Multi-wavelength study of X-ray reprocessing in Low Mass X-ray Binaries

Gayathri Raman

This thesis is submitted for the degree of

Doctor of Philosophy

Jawaharlal Nehru University, New Delhi

Department of Astronomy and Astrophysics
Raman Research Institute

September 2017

To my family and friends.
And to my kitten Fluffy, without whom this thesis would have probably been completed much sooner.

Certificate

This is to certify that the dissertation entitled 'Multi-wavelength study of X-ray reprocessing in Low Mass X-ray Binaries' submitted by Gayathri Raman for the award of the degree of Doctor of Philosophy to Jawaharlal Nehru University, is her original work. This has not been submitted or published for any other degree or qualification to any other university.

Prof. Ravi Subrahmanyan
Director

Prof. Biswajit Paul
Thesis Supervisor

Raman Research Institute,
Bangalore 560 080
INDIA.

Declaration

I, Gayathri Raman, declare that the work reported in this thesis titled 'Multi-wavelength study of X-ray reprocessing in Low Mass X-ray Binaries', is entirely original. This thesis is composed independently by me at the Raman Research Institute under the supervision of Prof. Biswajit Paul. I further declare that the subject matter presented in this thesis has not previously formed the basis for the award of any degree, diploma, membership, associateship, fellowship or any other similar title of any university or institution. I also declare that I have run it through TURNITIN plagiarism software.

Prof. Biswajt Paul

Gayathri Raman

Astronomy and Astrophysics Group
Raman Research Institute,
Bangalore 560 080
INDIA.

Acknowledgements

I wish to take this opportunity to extend my gratitude to all those who have made my PhD journey memorable.

I thank my supervisor Prof. Biswajit Paul for introducing me to the exciting field of X-ray astronomy. His unique mode of coaching has been very helpful in moulding me into an independent thinker. He has been extremely patient with me and my work. He has tolerated my short-comings while allowing me to make my own mistakes and learn from them. Since the days of my Masters program in Pune, I have been a fortunate recipient of Prof. Dipankar Bhattacharya's warm mentorship, something I will continue to cherish for a long time. I thank Desh for many insightful discussions on Astronomy and academia. I thank Prof. Andal and Desh for providing valuable inputs as members of my thesis advisory committee.

I thank my parents who have been extremely supportive and tolerant of my resolute stubbornness to pursue Science. I thank my brother Sai for morphing into my best friend, during these years. I am deeply indebted to all my friends and colleagues at RRI- Mayuri, Raju, Nomaan, Nazma, Lijo, Varun, Deepak, Priyanka, Aditi and the others for creating such an enjoyable atmosphere at RRI and the hostel so much so that I have eagerly looked forward to going to RRI, every single day, for the last six years. Their affection has always made me feel extremely special. I will cherish all the wonderful memories that I share with them. I thank Nomaan and Varun for getting me into swimming, which has become sort of an addiction ever since. My fellow X-ray group members Aru, Nazma, Varun, Chandreyee, Nafisa and Nirmal have been more than kind in assisting me with my work at various stages. I thank my batch-mates Rahul, Madhuri, Surya, Amu and Mriganko, whose wonderful company kept me going during my formative years as a graduate student. It means a lot to me that I have friends outside the academic circle who cared for me and encouraged me a whole lot more. Thank you all - Praharsha, Susmitha, Raman, Pavithra, Vaidya, Saranya, Shailesh,

Manasi and Venu. RRI has been home to some of the most wonderful feline fluff-balls I have ever known: Ludo, Kandappi, Bhageera, Puss-in-Boots, Mojo-Jojo and our astro-floor's very own personal kitten, Fluffy. I have had the pleasure of knowing them since they were kittens and caring for them, while they were being raised within the RRI campus.

I thank Vidya for being a mother figure to all of us on the Astro floor. I thank Radha and Marisa for making the academic paperwork smooth and hassle-free. I sincerely thank the RRI canteen staff for providing us with nutritious and extremely homely food that I am sure to keep coming back for. I thank the computer staff for catering to my ever-so-frequent technical mishaps.

Last but not the least, I am ever grateful to RRI for being my Home for all these years. These will probably be the most memorable 6 years of my life.

Synopsis

Neutron Star Low Mass X-ray Binary systems (NS - LMXBs) consist of a NS accreting matter from a low mass companion star. Primary X-ray photons which are emitted from the NS surface or the inner accretion disk, irradiate various components of the binary, get absorbed and are eventually re-emitted at UV/optical wavelengths. Since these point source systems are not resolvable even using telescopes with the highest angular resolution, X-ray to UV/optical reprocessing becomes a useful tool that can be used to explore such systems. These systems also exhibit a number of X-ray variability signatures like Quasi Periodic Oscillations, thermonuclear bursts, flares, etc. that often get reprocessed into the UV/optical band. Although optical studies have been carried out on LMXB sources before, due to lack of simultaneous X-ray and optical observations, the reprocessing phenomenon has remained largely unexplored. As part of this thesis, results of detailed studies of X-ray to optical reprocessing in several individual LMXBs using X-ray and optical data obtained from a number of space-based X-ray telescopes and ground-based optical telescopes are presented. We have detected a number of interesting reprocessing signatures that indicate the presence of evolving structures on the accretion disk. I further discuss disk wind emission scenarios, their possible correlation to the luminosity state in NS LMXBs and our study of the X-ray spectrum of an LMXB exhibiting disk winds. The thesis is structured in such a manner that the scientific context of the work is presented in the introductory chapters followed by chapters detailing timing and spectral analysis work on three individual LMXBs. In the concluding segment of the thesis, I discuss the possible extention of the results of this thesis work in the context of light curve modeling, inadequacies of the reprocessing phenomenon and binary parameter estimation for potential sources of Gravitational Waves.

List of Publications

- X-ray Pulse reprocessing in 4U 1626-67 using SALT
  Gayathri Raman, Biswajit Paul, Dipankar Bhattacharya, Vijay Mohan, 2016, MNRAS 458, 1302R

- X-ray and Optical orbital modulation of EXO 0748-676: A covariability study using XMM-Newton
  Gayathri Raman, Biswajit Paul, 2017, New Astronomy, 54, 122

- Observation of variable pre-eclipse dips and disk winds in the eclipsing LMXB XTE J1710-281
  Gayathri Raman, Chandreyee Maitra, Biswajit Paul, accepted for publication in MNRAS

- Re-visiting the ultra-compact LMXB pulsar 4U 1626-67 using SALT
  Gayathri Raman et al.. in preparation

Other publications:

- Multitude of of Fe lines in OAO 1657-415 detected with Chandra
  Pragati Pradhan, **Gayathri Raman**, Biswajit Paul, submitted to MNRAS

- Fermi-LAT observations of the brightest gamma ray flare in CTA 102
  Raj Prince, **Gayathri Raman**, Nayantara Gupta, submitted to ApJ

- Detection of type-1 bursts from the Galactic Center using Astrosat-LAXPC
  Gayathri Raman, Varun, Nirmal Iyer, Biswajit Paul, ... in preparation

"Why just look when you can observe?" - Sherlock Holmes

Table of contents

List of figures

List of tables

Prologue

Before the thesis banter begins, allow the author to guide you through a series of events that led to the birth of high energy X-ray astronomy as we know it today. Imagine being an Italian-born American scientist, say Mr. RG (not quite unlike the author's initials), in the early 1950s. War has just ended. Terrestrial X-rays were discovered by Wilhelm Röntgen not too long ago. Since the atmosphere absorbed most X-ray photons, you, or no one else knows if X-rays were being emitted from space. Using a number of captured german rockets, you send up X-ray and UV detectors above the earth's atmosphere and detect a low X-ray count rate from the sun. You then assume that other heavenly bodies also emitted faintly in the X-rays. After a couple of failed attempts, you and your team, while looking for X-rays from the moon, accidentally detect X-rays (from your 5 minute flight experiment!) peaking from different parts of the sky, particularly from a source in the direction of the constellation Scorpius. Little would you know, that the discovery of this first extra-solar X-ray source, Sco X-1 would end up opening an entire window of X-ray astronomy and also get you your Nobel Prize in 2002!

Coming back to the present and disengaging from the fantasy of identifying with Mr. Riccardo Giacconi, astronomy in X-rays is a very well established and ripe field, owing much of its credit to the early detectors and space-borne balloon experiments. The first orbiting X-ray satellite Uhuru was launched in 1970 by Giacconi and his team. Since then, there has been a surge in X-ray telescopes like Einstein, ROSAT, ASCA, RXTE, XMM-Newton, Chandra and several others (described in Chapter 2 of this thesis). These telescopes were aimed at probing a number of astrophysical sources, particularly compact remnants of massive star evolution, like neutron stars and black holes, that emitted significant amounts of X-rays. To account for the unusual X-ray energy spectrum of these sources, the physical process of "Accretion" had to be inevitably invoked. In an accreting binary system, the compact object is in orbit with another young and middle-aged, fuel-burning ordinary star, from which it tends to whisk away matter through a highly energetic and cannibalistic process called accretion.

Accretion ends up transforming an otherwise invisible compact star system into one of the brightest objects in the X-ray sky. This thesis focuses on X-rays from accreting neutron stars in a binary configuration with low mass stars.

Chapter 1

Introduction

1.1 Neutron stars

Back in 1934, two astronomers Bade and Zwicky, predicted that there must exist exotic compact objects called neutron stars. These objects are remnants of massive stars (>8$M_\odot$) that undergo a supernova explosion after a gravitational collapse. The realization that the X-ray sources detected by Giacconi and others contained such neutron stars proved to be invaluable to the understanding of stellar evolution and nuclear physics in extreme conditions. Neutron stars with masses of the order of 1.4 - 2.0 $M_\odot$, and extremely small radii (∼12 km, the size of a small city), are the densest objects in the universe (∼10^{14} g cm^{-3}). They are mainly composed of neutrons, but also contain protons, electrons and muons. A schematic of the different regions in a neutron star is shown in Figure 1.1. It comprises of the outer atmosphere, the envelope, the crust, outer and inner core. For extreme densities there have been predictions of the presence of exotic matter such as strange baryons, condensed mesons, de-confined quarks, along with fermions exhibiting superfluidity and super-conductivity (Lattimer and Prakash, 2001).

Obtaining the equation of state (EoS) for the dense matter present in neutron stars has been a long standing problem in nuclear physics. Depending on the exact composition of the star, a number EoS arise. These need to be numerically solved in order to obtain a unique mass versus radius (M-R) relation (Lattimer and Prakash, 2001; Steiner et al., 2013). There are many EoS models for a neutron star (For example, Friedman and Pandharipande 1981; Pandharipande and Smith 1975). Precise measurements of both the mass and the radius of neutron star sources using observations will help determine

the universal M-R relation and also place strong constraints on the EoS for dense matter.

Emission from Isolated Neutron Stars (INS) like rotation-powered pulsars (for eg. Crab), that emit periodic radio pulsations, is dominated by non-thermal processes like synchrotron radiation, where particles are relativistically accelerated in the pulsar's magnetosphere. Other INS candidates include radio-quiet neutron stars (for eg. The Magnificent Seven, Treves et al. 2001), magnetars, Central Compact Objects in Supernovae Remnants (Pavlov et al., 2004), etc. A number of middle to old aged ($\sim 10^5$-10^6 years) radio-quiet INS sources are also observed to have high thermal emissions along with a non-thermal component (whose origin remains uncertain, see Treves et al. 2000 for a review). The surface temperatures of neutron stars for these sources are in the range $\sim 10^5$ - 10^6 K, suggesting that the bulk of the emitted thermal radiation should lie in the far-UV and soft X-rays.

Neutron stars have also been identified in binary configurations called X-ray binaries, which are some of the brightest objects in the X-ray sky. These systems comprise a compact object (neutron star or a black hole) primary, and a main sequence, dwarf or giant companion secondary, gravitationally bound and co-rotating about their common center of mass. Depending on the nature and mass of the companion star, X-ray binaries are classified as High Mass X-ray Binaries (HMXBs) and Low Mass X-ray Binaries (LMXBs). The companion in HMXBs is typically a luminous early spectral type OB high mass star (typically > 10 $M_\odot$), while in LMXBs, the companion is a late spectral type low mass star (1 $M_\odot$ or less) (Chaty, 2011). The following section describes a particular class of LMXB systems that host a neutron star primary accreting matter from a low mass secondary.

1.2 Low Mass X-ray binaries

Since the early 1960s a number of bright X-ray sources were observed within 30° of the direction of the galactic center (Dolan, 1970). It was suspected that there existed a class of X-ray systems that comprised of a primary compact object, either a neutron star or a black hole, accreting matter from a low mass companion (M $\sim$1 $M_\odot$). Towards the end of the 1980s, LMXB sources were identified as a distinct class of objects with respect to their distributions, X-ray spectral characteristics, optical properties as well as variabilities (Lewin and Clark, 1980). Galactic LMXBs are distributed more towards

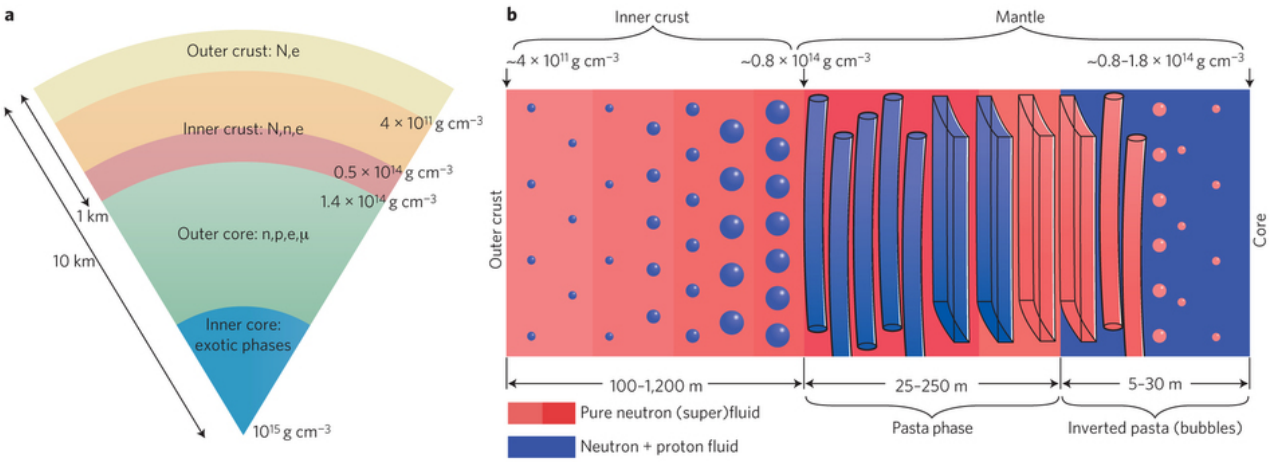

Fig. 1.1 Schematic of a neutron star adapted from Newton (2013). Letters N, n, p, e, μ represent nuclei, fluid neutrons and protons, electrons and muons, respectively. The inner core is suspected to be composed of various exotic particles like hyperons, etc.

the galactic bulge and in globular clusters (see Figure 1.2); the distance spread of these objects from the Galactic plane is nearly 1 kpc (van Paradijs and White, 1995). There are currently about 200 LMXBs observed in our galaxy and many hundreds in nearby galaxies (Liu et al., 2007; Fabbiano, 2006).

In LMXBs, matter from the low mass ($<1M_{\odot}$) companion falls into the gravitational influence of the compact object (Figure 1.3). In-falling matter, due to its pre-existing angular momentum, forms an accretion disc. Disc accretion, thus, forms the dominant mode of accretion in LMXB sources (see Lewin and Joss 1983 for a detailed review). There are multiple evolutionary scenarios that can give rise to an LMXB kind of a system with $M_{donor} < 1.5\ M_{\odot}$ and orbital periods less than ~ 10 days (Liu et al., 2007). The fact that these systems are bound and have such close orbital separations in-spite of the fact that the neutron star should have emerged from a massive progenitor, led to the development of the concept of the "Common envelope" scenario (Paczynski, 1976). In this model, the progenitor system is composed of a low mass star along with a sufficiently massive Helium star ($>2.3\ M_{\odot}$, Habets 1985). The massive star is captured by the companion's expansion and moves through the envelope, resulting in orbit shrinking due to frictional drag. This is the Common Envelope (CE) phase, after which the envelope is ejected and the resulting core undergoes a supernova explosion to form a neutron star (or a black hole). There are alternative models that propose other evolutionary pathways. In one case, a cataclysmic variable consisting of a white dwarf

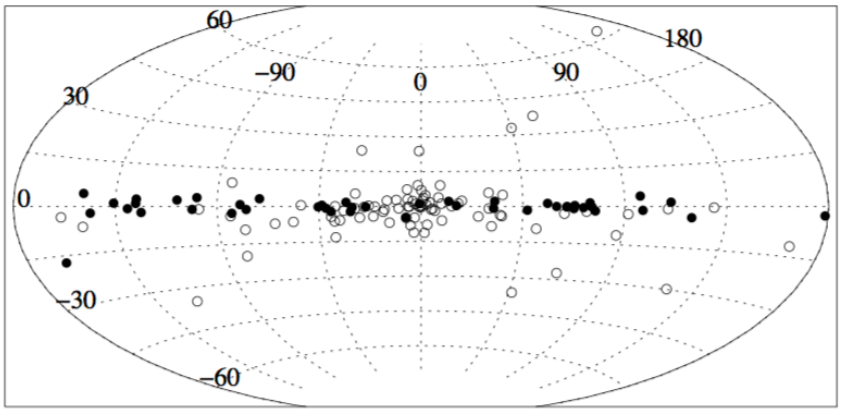

Fig. 1.2 Galactic distribution of X-ray binaries. The open circles represent LMXBs. Adapted from Grimm, Gilfanov et al. (2002).

accreting from a regular companion, evolves. The white dwarf undergoes accretion induced core-collapse and a neutron star LMXB results. In another proposed scenario, the evolution of a triple star system may result in the formation of an LMXB (Eggleton and Verbunt, 1986). A detailed review on the formation and evolution of LMXBs is given in Bhattacharya and van den Heuvel (1991) and Tauris and van den Heuvel (2006).

1.2.1 Classification

Based on a number of timing and spectral observational properties, LMXBs can be classified into various categories. Here we give a description of the LMXB class and its sub-categories.

- LMXBs hosting a neutron star primary, are further classified as Z and Atoll sources based on correlations observed between X-ray timing properties and the trajectory traced in a color-color or color-intensity digram (Hasinger and van der Klis, 1989). A color-color diagram represents a plot containing ratios of intensities in different wavebands. A hardness-intensity (or color-intensity) diagram is a similar representation of the color versus the intensity observed in a given band (see Figure 1.4). Any given LMXB source observed over a long span can be seen to trace a Z or Atoll shape in these color-color diagrams. The differences in the two are elaborated below:

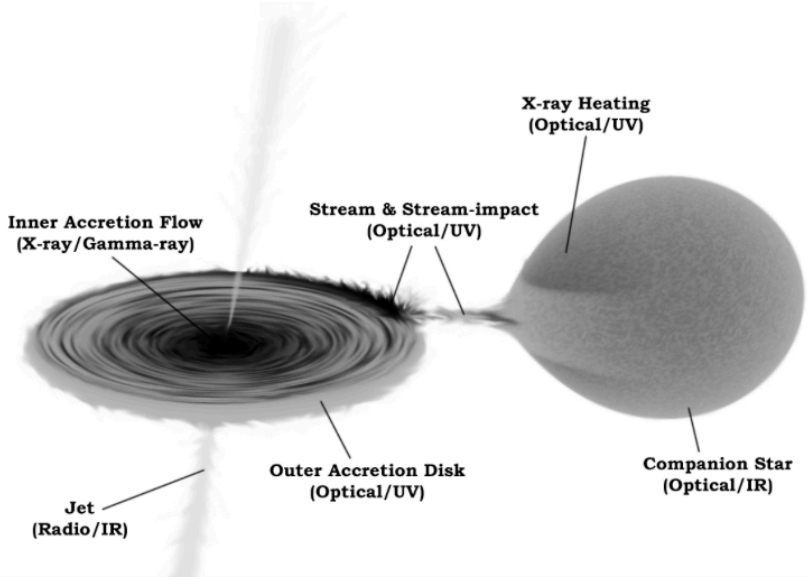

Fig. 1.3 LMXB schematic adapted from Hynes (2010). The compact object is shown to draw matter from the secondary star via an accretion disc.

- **Z source:** Hard color versus soft color plots of some LMXBs trace a Z shape within timescales of a few hours to days. Their timing properties include simple broad band noise components with strong (10%) Quasi Periodic Oscillations (QPOs) in the frequency range 1-60 Hz. Z sources are found to have extremely high accretion rates (0.5 - 1 L_{Edd}). The resulting spectral state is always soft, that can be described by the sum of a blackbody thermal component ($\sim$1 keV) and a Comptonized component from warm optically thick electrons (Di Salvo et al., 2000). Examples of Z sources include Cyg X-2, GX 17+2, etc.
- **Atoll source:** Atoll sources trace a band shape in the X-ray color-color diagram with islands of points appearing on timescales of weeks to months. These systems have lower accretion rates (0.01 $L_{Edd} < L_X <$ 0.5 L_{Edd}). Apart from broad band noise in the power density spectra, no QPOs are typically observed in these objects. Their energy spectral changes are extremely dramatic with sources spending time at the bottom of the color-color diagram in the soft state and then suddenly swinging to the top of the diagram (spectral index $\sim$1.8) during the faint hard state. Examples of Atoll sources include EXO 0748-676, 4U 1820-303, Aql X-1, GX 13+1, etc.

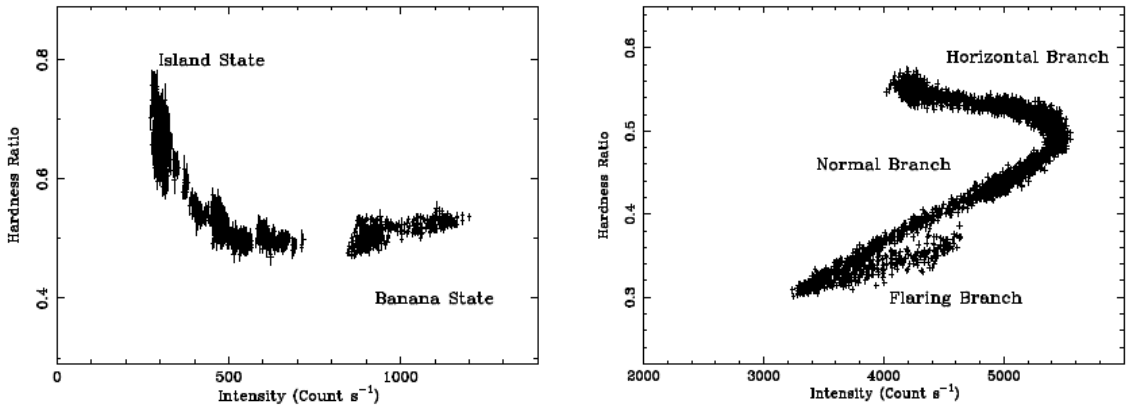

Fig. 1.4 Hardness intensity plots constructed from RXTE-PCA data for two sources. The left panel shows an atoll source 4U 0614+091 with its island and banana states and the right panel is a Z track source GX 340+0. Image adapted from Church et al. (2014).

- Based on the mass accretion activity, X-ray binaries are classified into persistent and transient sources.
  - **Persistent:** Persistent sources are those that accrete consistently all the time and remain active throughout. Their typical X-ray luminosities are above 10^{36} ergs s^{-1}. A large fraction of neutron star LMXBs tend to be persistent systems, for example Cyg X-2, Sco X-1, etc.
  - **Transient:** Transients however, remain dormant most of the time with low luminosities ($L_X \sim 10^{30} - 10^{34}$ ergs s^{-1}) in the quiescent state. They undergo outbursts where the luminosity increases by several orders of magnitude. Examples of transients include IGR J00291+5934, SAX J1808.4-3658, etc.
- Geometry: Depending on the angle of inclination of the binary system on the sky plane with respect to the line of sight of the observer (Figure 1.5), sources have face-on, edge-on or intermediate geometries. Intensity variations in light curves like ellipsoidal modulations, near-zero intensity drops at certain periodic orbital phases due to eclipses of the inner accretion disc region by the companion star[1], X-ray intensity dips that appear as additional structures in the light curves, etc. can be a result of the viewing geometry.

[1]The very idea that X-ray sources in the galaxy are mass exchanging binary stars, co-rotating with a compact accretor, was widely accepted, only after the first X-ray satellite Uhuru observed regular eclipses in Cen X-3 (Giacconi et al., 1971; Schreier et al., 1972).

- **0° < i < 60°**: No intensity dips or eclipses are seen. For example, 4U 1626-67 (Chapter 3).
- **60° < i < 75°**: This geometry allows for X-ray intensity dips to be observed. Dips are understood to be caused by the thick outer disc structures (White and Swank, 1982a) blocking the X-ray emission at specific orbital phases (Chapters 4 and 5).
- **75° < i < 80°**: Edge on geometry with this inclination range allows for dips as well as eclipses to be detected in the light curve (Chapters 4 and 5).
- **80° < i < 90°**: Extremely high inclination sources that also exhibit partial eclipses, are termed as Accretion Disc Corona (ADC) sources. In these objects, the observed emission is not from the inner disc region, but from an extended X-ray disc corona above the accretion disc (White and Holt, 1982). Depending on the geometry of this coronal structure, the companion star blocks a part of the ADC and gives rise to partial eclipses.

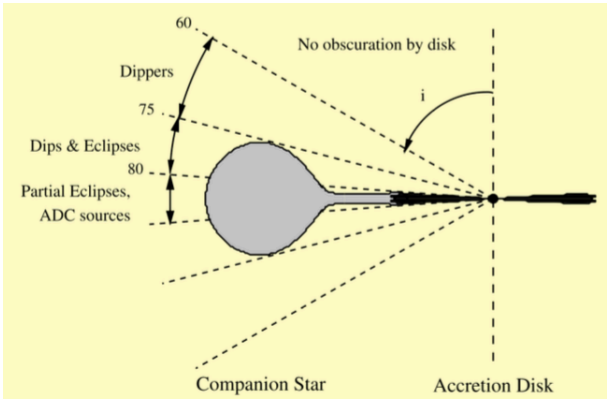

Fig. 1.5 Viewing geometry of an LMXB and the corresponding observational signatures in a typical light curve. Adapted from Seward and Charles (1995).

1.2.2 Theory of accretion

In binary systems, the two binary components, which are the primary star and the secondary star, orbit around their common center of mass. The physics of a test particle orbiting in the gravitational potential of two massive bodies under their mutual gravitational influence was first described by the French Mathematician Edouard Roche in the nineteenth century. The test particle is considered to be a point mass that does

not perturb the orbits of the massive objects. The orbits are assumed to be circular. The gas flow can be described by Euler's equation,

$$\frac{\delta v}{\delta t} + (v \cdot \nabla)v = -\nabla\phi_R - 2\omega \times v - \frac{1}{\rho}\nabla P \tag{1.1}$$

where ω is the angular velocity of the system and the $\omega \times v$ term is the coriolis force, observed in a rotating frame.

The gravitational potential or the Roche potential ϕ_R, which includes both the gravitational and centrifugal force effects of the binary in such a configuration, is given as follows (Frank et al., 1992):

$$\phi_R(r) = -\frac{GM_1}{|r - r_1|} - \frac{GM_2}{|r - r_2|} - \frac{1}{2}(\omega \times r)^2 \tag{1.2}$$

The equipotential surfaces of the Roche potential ϕ_R are shown in Figure 1.6. The circular equipotentials of both stars represent the regions of gravitational influence of each of them. These surfaces are termed as the Roche lobes. The two Roche lobes are connected at a point called the inner Lagrangian point L1, where matter is capable of escaping the gravitational influence of one star and pass on to the next star. This kind of mass transfer between stars is expected observationally, mainly because stellar objects evolve with time and in the course of their evolution, one star may swell up, or the binary separation may shrink. This process of mass transfer via the L1 point, from the secondary star to the primary star, is termed as "accretion via Roche lobe overflow".

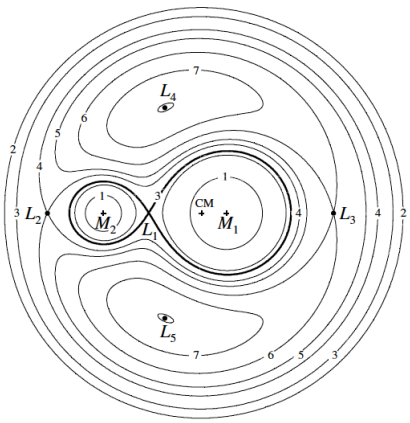

Fig. 1.6 Figure showing the equipotential surfaces for a binary system. Image credits: Frank et al. (1992).

The Roche lobe radius is a function of the mass ratio q (M_2/M_1) and the binary separation a, where M_1 and M_2 are the masses of the primary star and the secondary star, respectively. The Roche lobe radius (Eggleton, 1983) for the secondary star is given by:

$$\frac{R_2}{a} = \frac{0.49q^{2/3}}{0.6q^{2/3} + ln(1 + q^{2/3})} \tag{1.3}$$

In close binary systems, when the matter around one star falls under the gravitational influence of the other, the process of accretion extracts the gravitational potential energy. This process is highly energetic and is considered as the primary energy source for a number of systems like X-ray binaries, Active Galactic Nuclei (AGNs) and even Cataclysmic variables (CVs) (Salpeter, 1964; Zel'dovich, 1964). The energy released when a gravitating body of Mass $M_\star$ and radius $R_\star$ accretes matter of mass m, is given by,

$$\Delta E_{accretion} = \frac{GM_\star m}{R_\star} \tag{1.4}$$

From equation 1.4, it can be concluded that the compactness of the star (the ratio $M_\star/R_\star$) dictates the strength of the energy released. Typically for neutron stars, with masses $\sim 1.4M_\odot$ and radii $\sim$ 10 km, the yield of ΔE_{acc} is of the order of 10^{20} cm^3 s^{-1} g^{-1}. The accretion luminosity is further given by,

$$L_{acc} = \frac{GM\dot{M}}{R_\star} \tag{1.5}$$

where $\dot{M}$ is the mass accretion rate and is limited by the accretion luminosity limit described below. The average inferred accretion rates in bright X-ray binaries are $\sim$ 10^{15} - 10^{18} g s^{-1} ($\sim$ 10^{-11} - 10^{-8} $M_\odot$ yr $^{-1}$). Transient systems, during quiescence, show typical accretion rates of $< 10^{-13}$ $M_\odot$ yr $^{-1}$.

Sir Arthur Eddington provided the condition for the limiting luminosity, by considering the balance between the outward radiation pressure and inward gravitational pressure,

$$L_{edd} = \frac{4\pi GMmc}{\sigma_T} = 1.3 \times 10^{38}(m/M_\odot) ergs^{-1} \tag{1.6}$$

The maximum luminosity of the system (L_{edd}) is reached when the radiation pressure due to the matter exceeds the inward gravitational pressure. The outward layers of the star get blown away and accretion gets halted.

Assuming all the power of the radiation being emitted is in the form of blackbody emission, the temperature T_b is given as,

$$T_b = \left(\frac{L_{acc}}{4\pi R_\star^2 \sigma} \right)^{1/4} \tag{1.7}$$

For an accreting neutron star, the Eddington limit is typically $\sim 10^{38}$ erg s^{-1} . The typical observed temperatures of the accreted material accreting below the limit, say 10^{36} erg s^{-1}, can be estimated to be $T_b \sim 10^7$ K, or a kT_b value of about 1 keV. These energies correspond to the X-ray band of the electromagnetic spectrum.

The process of accretion acts as an efficient means of extracting the gravitational potential energy from X-ray binary systems. In LMXBs hosting neutrons stars, the accretion mode varies depending upon the strength of the magnetic field of the neutron star.

- **Disc accretion: Low magnetic field neutron star primary**
  In a rotating binary system, since the in-falling material arrives through the inner Lagrangian point with enormous angular momentum, it does not directly fall onto the primary compact object. The material at L1 follows an elliptical orbit along the binary plane and around the primary compact object. A continuous stream of incoming matter at L1 leads to matter, which is already present, being pushed into each subsequent inner ring (of smaller radius) while losing angular momentum and dissipating energy. Such a process of in-spiraling of matter leads to the formation of an accretion disc. The source of the loss of angular momentum is considered to be disc viscosity, although the exact functional form of this viscosity is not understood.

  The total disc luminosity is given by the binding energy of matter which accretes onto the surface of the primary.

$$L_{disc} = \left(\frac{G M_1 \dot{M}}{2 R_\star} \right)^{1/2} = \frac{1}{2} L_{acc} \tag{1.8}$$

  The disc luminosity L_{disc} is thus one half of the total accretion luminosity that is radiated.

Since the magnetic field of the neutron star is low (10^6 - 10^7 G), the inner accretion disc extends to almost the surface of the neutron star, with inner disc radii $\sim$ 10 - 12 km.

Shakura Sunyaev disc:
The Shakura Sunyaev disc prescription of an accretion disc assumes a geometrically thin and optically thick disc (Shakura and Sunyaev, 1976). The matter is assumed to lie very close to the disc plane, efficiently cooled and in a Keplerian orbit around the compact object. The Keplerian angular velocity of the matter orbiting in circles around the primary star is given by,

$$\Omega = \Omega_k(R) = \left(\frac{GM}{R^3}\right)^{1/2} \tag{1.9}$$

The effective temperature profile for a steady thin disc is T(R) $\propto$ $R^{-3/4}$. The mechanism responsible for angular momentum loss and inward spiral is specified by the viscosity parameter, ν which is parametrized as

$$\nu = \alpha c_s H \tag{1.10}$$

where c_s is the local sound speed, H is the disc thickness and α is a free parameter, typically of the order unity.

- **Accretion powered X-ray pulsars: High magnetic field neutron star primary**
  In LMXBs that host a highly magnetic neutron star ($\sim 10^{12}$ G), effects of the strong magnetosphere come into play and accretion proceeds differently (Pringle and Rees, 1972). Such strong fields disrupt the accretion flow at a radius where the magnetosphere and the disc flow interact (Figure 1.7).

  Assuming a dipolar magnetic field B, the field strength is given by,

$$B \sim \frac{\mu}{r^3} \tag{1.11}$$

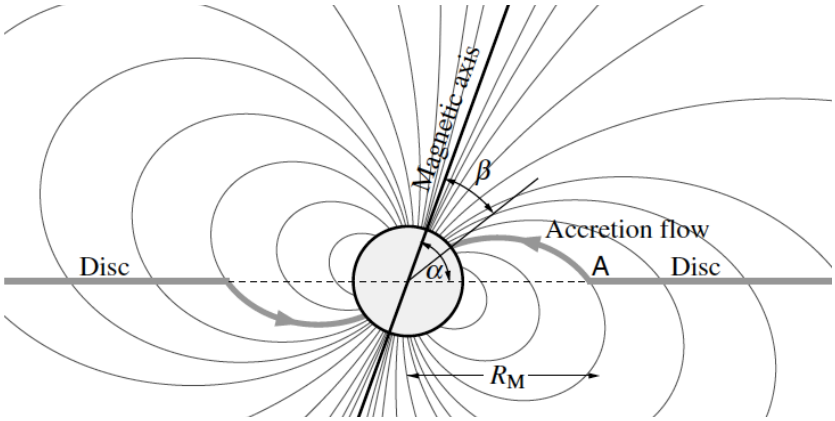

Fig. 1.7 Accretion onto a magnetized neutron star (Frank et al., 1992).

where r is the radial distance from the star with radius $R_\star$ and magnetic moment $\mu = B_\star R_\star^3$. This field generates a magnetic pressure given by,

$$P_{mag} = \left(\frac{4\pi}{\mu_0}\right)\frac{B^2}{8\pi} = \left(\frac{4\pi}{\mu_0}\right)\frac{\mu^2}{8\pi r^6} \tag{1.12}$$

The above equation suggests that during accretion, as the matter approaches the stellar surface, with decreasing r, the P_{mag} increases steeply. The magnetic pressure is strong enough to control the accretion flow by disrupting the accretion disc. In-falling matter is spherically symmetric and the flow is highly supersonic. The matter comes in with a ram pressure ρv^2, where the velocity v is the free-fall velocity, $v_{ff} = (2GM/r^{1/2})$. The ram pressure is given by,

$$\rho v = \frac{\dot{M}}{4\pi r^2} \tag{1.13}$$

At the magnetospheric boundary, the two pressures match, giving

$$\left(\frac{4\pi}{\mu_0}\right)\frac{\mu^2}{8\pi r^6} = \frac{(2GM)^{1/2}\dot{M}}{4\pi r_M^{5/2}} \tag{1.14}$$

This gives the radius of the magnetosphere, or the Alfvén radius below which the magnetospheric influence on the accretion flow starts dominating.

$$r_M = 5.1 \times 10^8 \dot{M}_{16}^{-2/7} m_1^{-1/7} \mu_{30}^{4/7} \tag{1.15}$$

where μ_{30} is the magnetic moment in units of 10^{30} G cm^3.

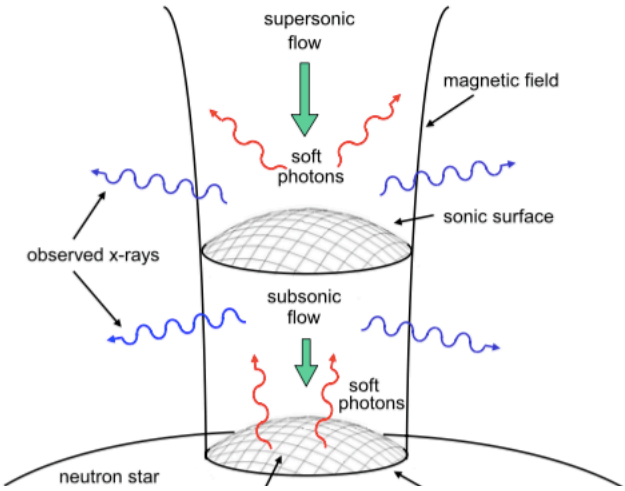

Fig. 1.8 The accretion column on the magnetic poles of an accreting neutron star is shown, where X-rays are generated in a high magnetic field environment (Becker and Wolff, 2007).

Inside the Alfvén radius, matter flows along the field lines and is channeled to the magnetic poles of the neutron star. Assuming that the neutron star and the corresponding magnetic field lines rotate with an angular velocity $\Omega_\star$ in the same direction as the disc angular velocity and the in-falling matter rotates with a Keplerian velocity (Ω_K), it can be shown that at the magnetospheric boundary, the following condition must be satisfied in order for accretion to take place:

$$\Omega_\star < \Omega_K(R_M) \tag{1.16}$$

If this is not satisfied, then matter would spiral outwards towards larger R, being repelled by a centrifugal barrier. For typical neutron star parameters and a luminosity of $\sim 10^{37}$ erg/s, the r_M of the star will be $\sim 10^8$ cm, far outside the stellar radius of a few 10^6 cm .

Accreted matter follows the magnetic field lines onto the magnetic poles of the neutron star via an accretion column (see Figure 1.8). In-falling matter is shocked and most of the kinetic energy is radiated out in the form of thermal Bremsstrahlung, blackbody emission and compton cooling. Thermal hotspots are created on the poles. Acceleration of relativistic charged particles in a high magnetic field also leads to the emission of Synchrotron emission, although this is not a significant component. X-ray pulsars, however do exhibit Cyclotron

Resonance Scattering Features (CRSF) in their energy spectra. The origin of these absorption features is understood to be due to the resonant scattering of X-rays by electrons in Landau orbits near the polar caps of the neutron star (Maitra and Paul, 2013).

If the magnetic axis and the neutron star spin axis are not co-aligned, the polar emission gets modulated at the spin frequency and appears as pulsed emission whenver it cuts the observer's line of sight (Lamb et al., 1973). The resultant object is an accretion powered pulsar. The pulsed emission is precisely clocked and typical pulsation periods lie in the range of 1 s to about 1000 seconds. From observational studies of pulse profiles, it has been inferred that the orientation of the resultant pulsed emission from accretion column provides two main beam patterns, the pencil beam and the fan beam or a combination of both (Kraus et al., 1996). Pulse profile analysis is crucial in determining the emission geometry, the accretion-disc-magnetospheric connection and accretion modes in accretion powered X-ray pulsars (Beri et al., 2014) .

The motion of this pulsating neutron star around the center of mass, adds a periodic modulation to the spin period due to the doppler motion. By conducting a pulse-arrival time analysis and modeling the modulation, the orbital period and the mass function of the system can be inferred. However, in a face-on system, which is geometrically inclined at a low angle on the sky plane, it becomes difficult to detect pulse arrival delays or doppler shifts in spectral lines. Such a system offers enormous challenges in orbital parameter determination.

Continuous monitoring of the spin evolution in several accretion powered X-ray pulsars (Bildsten et al., 1997) has shown a number of interesting patterns. Pulsars like 4U 1626-67 and GX 1+4 exhibited a steady spin up until a sudden torque reversal led to a spin-down rate similar to the spin-up rate, except with the opposite sign. On the other hand, sources like Cen X-3, OAO 1657-415 and Her X-1 exhibit spin up with small spin variations (Klochkov et al., 2009). Torque reversals occurring as a result of sudden changes in mass accretion rate have been insufficient to explain the spin changes in many sources. Currently, several other models that explain the observed torque reversal behavior in X-ray pulsars, include the magnetically threading disc model (Ghosh and Lamb, 1979; Bozzo et al., 2009), a disc in the propeller phase model (Illarionov and Sunyaev, 1975),

a disc bi-state model (Yi et al., 1997), and the retrograde or warping disc model (Nelson et al., 1997; van Kerkwijk et al., 1998). Some of these models have been invoked to explain the observed spin changes, flux changes as well as the measured QPO frequencies before and after torque reversal epochs and are found to be not wholly satisfactory. A recent model by Zhang and Li (2010) suggests that outflows or winds from the disc-magnetospheric boundary could play an important role to particularly explain spin-down in disc-accreting X-ray pulsars. Details of the spin changes, pulse profiles during different torque reversal epochs etc. have been considered in Chapter 3 of this thesis.

Timescales: Over the course of this thesis, while a number of accretion disc processes are probed, there is mention of several timescales as well as how the disc emission is modulated over those timescales. The following text is a small introduction to the different relevant timescales in an accreting binary system:

- **Dynamic timescales:** This is the time it takes for the accreting matter to complete an orbital cycle and is therefore related to the Keplerian angular velocity ω_K.

$$t_{dyn} = \frac{r}{v_K} = \frac{1}{\omega_K} \tag{1.17}$$

  This timescale also represents the characteristic timescale required to re-establish hydrostatic equilibrium. The dynamical timescales in an LMXB for outer accretion disc radii of about $\sim 10^{10}$ cm are of the order of a few minutes.

- **Thermal timescales:** This is the time required for the disc to attain thermal equilibrium and is a function of the heat content and the dissipation rate.

$$t_{th} = \frac{\text{thermal content}}{\text{dissipation rate}} \tag{1.18}$$

  Also,

$$t_{th} = \frac{1}{\alpha} t_{dyn} \tag{1.19}$$

  Assuming $\alpha \sim 0.02$ at an accretion disc radius of 10^{10} cm, gives a typical t_{th} of about a few hours. Thermal timescales are thus longer than dynamical timescales.

- **Viscous timescales:** This is the time required by the accretion fluid to drift in the radial direction. During the process of disc formation, matter forms a circular

ring around the compact object (at the circularization radius r_{circ}). Once more matter starts flowing in, a radial drift of matter ensues, while the material collides with previously existing material. The timescale for the matter to radially drift inwards is the viscous timescale specified by,

$$t_{vis} = \frac{r}{|v_r|} = \frac{r_{circ}^2}{\nu_{viscous}} = \left(\frac{h}{r}\right)^{-2} \frac{1}{\alpha\Omega} \tag{1.20}$$

where ν is the viscosity, v_r is the radial velocity, h/r is the scale height of the accretion disc. Assuming a scale height of h/r<<1 for thin accretion discs and an alpha value of 0.02, typical viscous timescales are of the order of a few 1000 years.

In effect the dynamical timescale is the shortest, while the thermal timescales are slightly longer. Both are much shorter than the viscous timescales in an accreting system.

1.2.3 Spectral properties of LMXBs

Emission processes

Continuum X-ray emission from LMXBs is governed by a number of processes, as detailed below:

- **Blackbody emission:** Matter close to the neutron star is in thermal equilibrium and is optically thick. The plasma temperatures here are typically of the order of 10^6 - 10^7 K. Emission from such a material is blackbody emission and follows the Planckian distribution given by,

$$B_\nu(\nu, T) = \frac{2h\nu^3}{c^2} \frac{1}{e^{\frac{h\nu}{k_B T}} - 1} \tag{1.21}$$

  The emission at a given frequency is solely dependent on the temperature T of the material, which is represented by the peak in the spectral shape. Processes like the thermonuclear X-ray bursts and soft excess due to hard-soft X-ray reprocessing are also modelled using the Blackbody function. In LMXBs, different radii of the accretion disc are at equilibrium at different temperatures, giving rise to a resultant multi-temperature disc blackbody spectrum (Mitsuda et al., 1984) .

- **Thermal Bremsstrahlung emission:** In extremely hot plasmas (T>10^6 K), the acceleration of charged particles like electrons in an electric field of a nearby

proton or ion results in the emission of breaking-radiation or bremsstrahlung. This is the main cooling process in extremely hot plasmas. The flux density S_ν is specified in terms of the temperature, T, frequency, ν and optical depth τ,

$$S_\nu \propto \frac{2kT\nu^2}{c^2}\tau_\nu \propto \nu^{-0.1} \tag{1.22}$$

- **Inverse Compton:** In a number of cases, high energy electrons ($\sim$ a few keV) present in the coronal structures, up-scatter low energy photons and in the process generate a stream of high energy photons in the energy range $\sim$ 10 - 60 keV for accretion powered pulsars (West et al., 2017). The average frequency of an up-scattered photon $< \nu >$ as a function of the initial frequency ν_0 and the Lorentz boost factor γ is given by,

$$\frac{< \nu >}{\nu_0} = \frac{4}{3}\gamma^2 \tag{1.23}$$

Spectral states in NS LMXBs: Accretion disc, corona and jets

Accreting neutron star LMXBs are found in several spectral states like the high/soft state and the low/hard state (Mitsuda et al., 1984, 1989; White and Mason, 1985). In the low/hard spectral state, the object exhibits a hard spectrum extending to about 100 keV, which is understood to be an outcome of thermal Comptonization of soft photons by hot electrons (Sunyaev and Titarchuk, 1980). The hot electron cloud is referred to as the Comptonizing corona (Zhang et al., 2016). During the low/hard state, when the mass accretion rate is relatively low (Luminosity $\sim 10^{36}$ ergs s^{-1}, 0.01 L_{edd}), the accretion disc is truncated at a large distance from the compact object and a Comptonizing corona, which is identified as a geometrically thick and optically thin accretion flow, is formed around the neutron star (Lightman and Eardley, 1974; D'Aì et al., 2010). The geometry and shape of the corona is still debated. In the high/soft state, the accretion disc moves close to the neutron star. This causes increased mass accretion rates (upto $\sim$0.5 L_{edd}), aiding efficient Compton cooling of hot electrons (D'Aì et al., 2010). The continuum spectrum is usually described by a thermal blackbody component from the neutron star surface, and disc blackbody emission (Zhang et al., 2014). The disc in the soft state is assumed to be a typical Shakura Sunyaev disc, optically thick and geometrically thin. The largely accepted picture of bimodal X-ray spectral state transition in these systems involves the accretion disc morphing from an optically thick, geometrically thin disc in the soft state, into an optically thin,

geometrically thick disc in the hard state (Zhang et al., 2014).

Several classes of LMXBs hosting neutron stars also exhibit transient outburst phases, where radio emission from highly collimated relativistic jets have been speculated. For example, take the Z and Atoll class of sources or the accreting milli-second X-ray pulsars (AMXP) and transitional millisecond pulsars (t-MSPs) type sources. During their outburst phases, their X-ray and radio emission are monitored in order to probe the inflow and outflow of material with respect to radio brightness and X-ray spectral state. Such radio/X-ray correlation studies allow for investigation of the effect of mass accretion, magnetic field strength etc. on jet launching phenomenon (Gusinskaia et al., 2017). However, BH-LMXBs are better characterized in the radio as compared to NS sources for a given X-ray luminosity (Fender and Kuulkers, 2001), since NS sources show weaker radio jets (Migliari and Fender, 2006; Gusinskaia et al., 2017), from about hundred of μJy down to a few tens of μJy. Spectral state dependent jet launching and quenching phenomenon in NS-LMXBs is still poorly sampled and is a topic of current and future research and hence is not discussed further in this thesis.

1.2.4 Reprocessing in LMXBs

According to the standard model of reprocessing, X-rays emitted by material near the compact object, photo-ionize and heat the surrounding regions of gas. This photo-ionized gas subsequently recombines and cools, producing lower energy photons (van Paradijs and McClintock, 1995; O'Brien et al., 2002; Hynes, 2005). This process of continuous irradiation of the different portions in the accretion disc and subsequent photon reprocessing, adds additional modulation to the overall form of the orbital light curve.

In LMXBs, the atmospheres of the accretion disc as well as the secondary star respond to incoming X-rays in mainly three regimes. The energy of the incident X-ray photon dictates the absorption/scattering phenomenon and thereby the emitted spectrum. The primary mechanism of reprocessing is photo-absorption/photo-ionization. The cross sections of the photo-absorption process is a steep function of energy ($\sigma_{ph} \propto \nu^{-3}$). At very low energies, the low energy photons get photo-absorbed at small optical depths and do not thermalize. The spectrum then produces significant line emissions. At intermediate photon energies (between 1 - 10 keV), X-rays penetrate deeper into the atmosphere before getting absorbed. This happens at moderate optical depths. This process leads to multiple scatterings of the emitted UV/optical photons,

leading to a thermalized spectrum. The energy distribution would be characteristic of the temperature of the photosphere. Beyond 10 keV, Compton scattering becomes the dominant process, while the photo-absorption cross-sections drop. Only a few high energy photons penetrate deep into the atmosphere, the remaining photons undergo scattering and get reflected back, while only depositing a fraction of their energy.

In LMXBs, a large fraction of the optical emission from the accretion disc is due to reprocessed X-rays which illuminates the disc surface (van Paradijs and McClintock, 1995). A linear relationship between the visual Luminosity L_V and the X-ray Luminosity L_X was proposed by van Paradijs and McClintock (1994), which is given by,

$$L_V \propto L_X^{1/2} P^{2/3} \tag{1.24}$$

where, P is the binary orbital period.

The reprocessed UV/optical emission is expected to posses a delay with respect to the primary irradiating X-ray emission due to light travel times within the binary. Delays are expected because, one fraction of primary X-ray photons are directly observed and the remaining fraction travels to different parts of the binary, gets reprocessed and re-emitted at lower wavelengths before reaching the observer. These delays can be up to twice the binary separation (O'Brien et al., 2002). The time delay τ for a particular reprocessing site in a binary with inclination i is specified in cylindrical co-ordinates (O'Brien et al., 2002) by,

$$\tau(x,\phi) = \frac{\sqrt{R^2+Z^2}}{c}[1+\sin i\mathrm{c}\cos(\phi-\theta)] - \frac{\mathrm{Z}}{\mathrm{c}}\cos\mathrm{i} \tag{1.25}$$

However, there is an additional time lag which is the diffusing delay. This takes into account motion of incident continuum X-ray photons, as it diffuses through the atmosphere and the emitted UV/optical photon, as it performs a random walk before escaping the atmosphere. There can also be delays corresponding to the photon-atom interaction timescales. The average reprocessing time (or re-combination time) for line photons as specified by Hummer (1963) is given by,

$$\frac{\tau_{rec}}{s} \sim \left(\frac{n_e}{10^{13}\ \mathrm{cm}^{-3}}\right)^{-1} \tag{1.26}$$

where, n_e is the electron density in the accretion disc, which is typically $\sim 10^{15}$ cm^{-3}. For continuum photons, these diffusion timescales have been shown to be less than 0.6 s, which is very small compared to binary light travel times (Pedersen et al., 1982). Thus for probing processes like burst reprocessing and orbital modulation reprocessing (see Chapter 4), diffusion timescales can be safely ignored and the reprocessing phenomenon can be treated as instantaneous. The optical photons are emitted from a region which has a finite spatial extent, which leads to a smear in the X-ray-optical lags. In effect, the optical response to an incident flash of X-ray light can be completely described by a function parametrized by just two parameters: delay and smear in delay.

Such time delay techniques are utilized in indirect imaging methods like Echo Tomography to understand the accretion disc, structures and their evolution. Typical procedures adopted to characterize delays and smear include i) X-ray/optical cross-correlation techniques and ii) constructing Gaussian Optical Transfer Functions. These methods have been used to study the reprocessing of Type-1 thermonuclear X-ray bursts in the eclipsing system EXO 0748-676 in detail and are elaborated in Chapter 4. Delay transfer functions may or may not also posses a binary phase dependence, depending upon the reprocessing site (O'Brien et al., 2002). For example, if the delay is a sinusoidal function of the binary phase, the secondary star surface is the dominant reprocessing site; and if no such phase dependence is observed, the delays observed are due to reprocessing from the circular accretion disc.

The effective temperature of a particular region at a distance R from the X-ray source of mass M_x, Radius R_{NS} is given by,

$$T_x^4 = \frac{Lx(1-A)}{4\pi\sigma R^2} \tag{1.27}$$

where the accretion luminosity L_x is

$$L_x = \eta \frac{GM_x\dot{M}}{R_{NS}} \tag{1.28}$$

A is the albedo, η is the efficiency and $\dot{M}$ is the accretion rate.
The temperature T, of an irradiated element which is at a distance R from the X-ray source, post-irradiation is

$$T^4 = T_x^4 \cos\theta \left(\frac{a}{R}\right)^2 + T_{eff}^4 \tag{1.29}$$

where θ is the angle between the line of sight and the element, T_{eff} is the unirradiated effective temperature of the element and a is the binary separation.

The irradiation temperature in terms of the accretion disc scale height (Shakura and Sunyaev, 1976) is specified by,

$$T_{irr}^4 = \frac{\eta \dot{M} c^2 (1 - A)}{4\pi\sigma R^2} \frac{H_{irr}}{R} \left(\frac{dlnH_{irr}}{dlnR} - 1 \right) \tag{1.30}$$

where, η is the efficiency of accretion, A is the X-ray albedo, H_{irr} is the local height at which the in-falling X-rays deposit energy.

The reprocessing process also manifests in the form of atomic spectral lines when continuum X-ray photons get intercepted by intervening disc material at energies corresponding to specific atomic transitions. Absorption and re-emission at these energies give rise to emission lines at these frequencies. For example, the fluorescent 6.4 keV neutral Fe K emission line is a result of such reprocessing near the compact object. The detection of emission lines can be used to probe the disc material composition and their strengths and velocities can give insights about disc winds.

Another dynamic effect of irradiation is disc warping. Warping can be expected if the irradiating photons scatter off the optically thick disc surface inducing radiation pressure (Pringle, 1996). Incident photons get absorbed as well as Thomson scattered. On an average they get re-radiated back in their original direction. The photon momentum gets absorbed by the disc due to which a single element of surface area dA experiences a force given by,

$$dF = \frac{2}{3} \frac{L}{4\pi R^2 c} dA \tag{1.31}$$

where L is the luminosity of the central irradiating source (Frank et al., 1992). If the disc is symmetric along the disc mid-plane, no net torque results. However, even a small perturbation on any one side of the disc can result in unequal radiation being incident on either side of the disc. If there are deviations from symmetry about the orbital plane, torques acting on the local disc material will make the disc ring rise out of the disc plane and precess. The radiation torque dG_{rad} drives the warp while the viscous torque $dG_{viscous}$ acts to restore the flat disc shape. Warping would then be observed when $dG_{rad} > dG_{viscous}$. Detailed perturbation analysis (Pringle, 1996) show that luminous discs around a compact object of radius $R_\star$, with a steady accretion rate

$\dot{M}$, are unstable to warping under the following condition:

$$\frac{R}{R_\star} > 8\pi^2\psi^2\frac{R_\star}{R_{Schw}} \tag{1.32}$$

where $R_{Schw} = 2GM/c^2$ is the Schwarzchild radius of the central compact star and ψ is the ratio of the vertical to the radial viscosity coefficients. The above equation shows that disc warping effects get significant after a radius of 10^8 - 10^9 cm for most disc-accreting LMXB systems hosting a neutron star primary of $M = 1M_\odot$ and radius $R_\star = 10^6$cm (Frank et al., 1992). Examples of disc warping effects are addressed in Chapter 3 and Chapter 4.

X-ray and optical timing variabilities

Steadily accreting systems exhibit a persistent level of emission in the light curves. On many occasions, particularly in NS LMXBs, a number of timing variabilities are observed in the light curves and in the power density spectra. The variabilities, specifically explored as part of this thesis, are addressed below:

- **Thermonuclear X-ray bursts**
  Observational studies of neutron stars in the early 1970s revealed sudden intensity peaks in their light curves (Grindlay, 1976). The origin of these eruptions or bursts, was soon understood to be thermonuclear in nature (Joss, 1977; Strohmayer and Bildsten, 2006), particularly since the ratio of the burst flux to the persistent emission flux exactly matched the ratio of the nuclear burning energy to the gravitational energy release (Bhattacharyya, 2010). However, nuclear energy released per nucleon during stable fusion is of the order of a few MeV, while the gravitational energy released by an in-falling nucleon onto the surface of the neutron star is $GM_{NS}m_{nucleon}/R$, which is $\sim$ 200 MeV. Stable nuclear burning, would thus be dominated by the over-luminous gravitational energy release and no thermonuclear burst would be observable. To explain the bursts, unstable nuclear burning was invoked, which successfully went on to explain burst energetics. Accretion onto the surface of a neutron star leads to accumulation of fuel, which undergoes hydrostatic compression as more matter keeps piling up. When temperature and density conditions reach ignition levels (typically within timescales of a few hours to days, Schatz and Rehm 2006), the entire fuel layer on the neutron star surface burns rapidly, leading to the thermonuclear burst profile

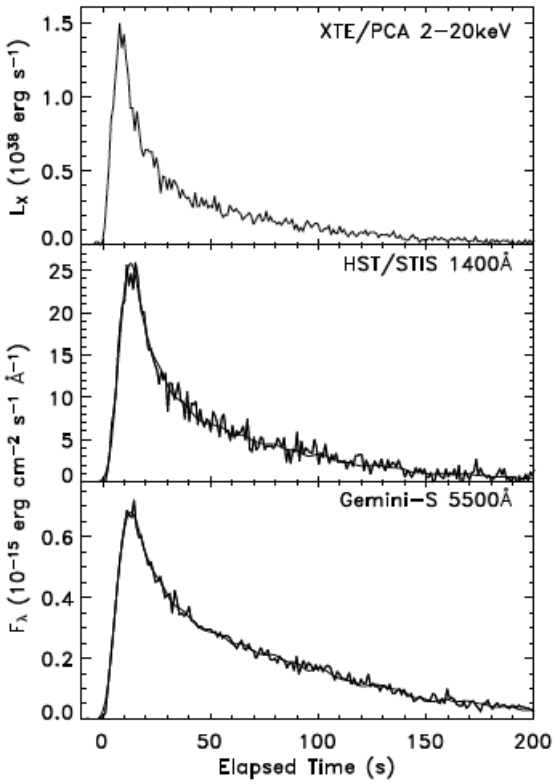

Fig. 1.9 Primary X-ray burst reprocessed into UV/optical in the source EXO 0748-676 (Hynes et al., 2006).

observed in the light curves. Since the burst emission area matched the emission area of the neutron star surface, the origin of these bursts was confirmed to be the neutron star surface (Bhattacharyya, 2010). During these burst episodes, the X-ray intensity rises by a factor of nearly 10 within a few seconds and then exponentially decays at a slower rate (10s - 100s of seconds, Galloway et al. 2008). Typically energy released during a single burst is of the order of 10^{39} ergs/s. Burning happens at a depth of 10 meters below the neutron star surface (corresponding to a column density of 10^8 g cm^{-2}). The ignition and compression rate depend on the accretion rate (Bildsten, 2000). In the regime of $\dot{M} < 900$ g cm^{-2} s^{-1}, the accumulated fuel exceeds a temperature of 10^7 K, resulting in burning of hydrogen via the CNO cycle. Mixed hydrogen and helium bursts are then triggered by unstable hydrogen ignition. Many NS LMXBs have shown evidence of thermonuclear X-ray bursts. In total, 6988 thermonuclear type-1 X-ray bursts from 84 burst sources observed by RXTE, Beppo-SAX and Integral have been

assembled in a database called the MUlti-INstrument Burst Archive (MINBAR)[2] .

Study of thermonuclear bursts is extremely interesting since these events light up the entire X-ray binary system like a flashlight. Since they occur right on top of the neutron star surface, many important neutron star parameters like the mass, radius and spin can be constrained from these bursts. This further allows for putting tighter constraints on the EoS of the neutron star.

Type-1 thermonuclear bursts exhibit a clear thermalized X-ray spectrum with blackbody temperatures between 1-3 keV. These photons being incident on the disc/companion surface, leads to an effective thermalized UV/optical response. (See Figure 1.9).

Thermonuclear bursts have been observed to be reprocessed instantly into UV/optical with a delay corresponding to the light travel time within the binary system and a smear in the delay owing to the finite extent of the reprocessing region in comparison to the X-ray emitting point-like source. Such reprocessed bursts were first discovered in 4U 1735-444 and Ser X-1 (Grindlay et al., 1978; McClintock et al., 1979; Hackwell et al., 1979). Subsequently such reprocessed bursts were observed in 4U 1636-536 (Pedersen et al., 1982), EXO 0748-676 (Paul et al. 2012; Hynes et al. 2006, this thesis). Burst spectral studies have shown that the temperature of the reprocessor rose by a factor of two (Lawrence et al., 1983) during bursts.

- **Quasi Periodic Oscillations**
  QPOs are features that appear in the power density spectra having a profile shape which can be described using a Lorenztian function.

$$P_\nu \propto \frac{A_0 w}{(\nu - \nu_0)^2 + (\frac{w}{2})^2} \tag{1.33}$$

where, ν_0 is the central frequency of the peak, w is the Full Width at Half Maximum (FWHM) and A_0 is the amplitude of the signal. The strength of the observed QPO is further characterized by its Quality factor (Q), which is

[2]https://burst.sci.monash.edu/wiki/index.php?n=MINBAR.Home

specified by

$$Q = \frac{\nu_0}{FWHM} \tag{1.34}$$

The width of the signal w and in turn Q, is a measure of the coherence time ($\tau = 1/\ [\pi w]$). Only signals with Q > 2 are considered QPOs, wider features are treated as noise. The fractional root-mean-squared (RMS) amplitude, being a function of source flux is proportional to the root of the integrated power,

$$r \propto P^{\frac{1}{2}} = \sqrt{\int P_\nu d\nu} \tag{1.35}$$

These features allow for detailed probing of a number of phenomena, like the disc-magnetospheric connections in accretion powered X-ray Pulsars, orbits of clumped matter near the inner accretion disc and even geometric modulations like disc warps. The most frequently invoked models that explain these QPOs fall into two main categories. i) The Beat frequency model (Alpar and Shaham, 1985) suggests that the QPO central frequency is at the beat frequency between the Keplerian frequency at the Alfvën radius of the disc-magnetosphere and the neutron star spin frequency. This would predict the Keplerian frequency to be, $\nu_k = \nu_{spin} + \nu_{QPO}$. ii) The Keplerian frequency model (van der Klis, 1987) suggests that the QPO frequency corresponds to the Keplerian frequency at the Alfven radius of the magnetosphere and that the QPO frequency is larger than spin frequency of the neutron star.

Optical studies of the power density spectra in several LMXB sources have reported optical QPOs at the same frequency of the X-ray QPO due to reprocessing in the accretion disc. For example, in 4U 1626-67, a 48 mHz QPO is simultaneously observed in the optical band as well (see chapter 3).

- **Flickering and flares**
  Many LMXBs do not exhibit thermonuclear X-ray bursts. But the source light curve is observed to flicker at short timescales. The response of such flickering has also been identified, where reprocessing leads to correlated optical flickering at identical timescales, albeit with a delay (see Figure 1.10). Such studies have been carried out for XTE J1118+480 and Sco X-1 (Ilovaisky et al., 1980). Correlated optical flickering behavior is also observed during the low accretion rate (quiescent)

state (Hynes et al., 2003; Zurita et al., 2003). Flares with timescales of a few hundred seconds are also reprocessed, for eg. in 4U 1626-67 (see Chapter 3).

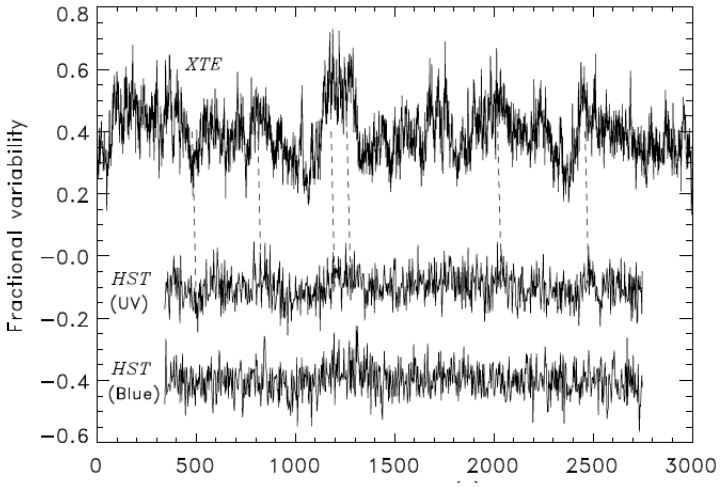

Fig. 1.10 Correlated flickering in GRO 1655-40 (Hynes et al., 2006)

- **Pulsations**
  Accretion powered X-ray pulsars emit pulsed X-rays at the rotation frequency of the neutron star. The X-ray emission is pulsed because of the mis-aligned rotation and magnetic axes. In some cases, the system geometry is such, that some fraction of the pulsed emission is also capable of irradiating nearby regions of the accretion disc and even the companion star. These X-ray pulsars exhibit optical pulsations at precisely the same frequency as the X-ray pulsation. This phenomenon is understood to be due to reprocessing at the accretion disc/companion star surface. Examples of X-ray pulsars that exhibit such optical pulsations are GX 1+4 (Jablonski et al., 1997a), 4U 1626-67 (Chakrabarty, 1998) and Her X-1 (Chester, 1979).

1.3 Challenges and Motivation

Although LMXBs prove to be excellent cosmic laboratories to probe compact object surroundings, an observational astronomer ends up facing several challenges.

- X-ray binaries are point sources and even with the best imaging telescope technologies, they cannot be resolved. Assuming that these sources are located at typical distances of the order of a few kilo-parsecs, and have an extent of a few light seconds across, gives an angular size of a few micro-arc seconds. Current

X-ray imaging telescopes like Chandra provide ∼0.5 arc second imaging resolution, at best. Individual binary components like the presence of an accretion disc, disc structures, disc wind outflows or even the companion star, cannot be directly imaged. This prompts looking at alternative methods of indirect imaging like echo mapping, X-ray-optical correlations, for these point source systems.

- To carry out X-ray-optical reprocessing studies, simultaneous X-ray and optical observational data is necessary. Since co-ordinated space-based X-ray as well as ground-based optical telescope observing time is often difficult to obtain, carrying out multi-wavelength timing studies becomes quite a challenge.
- Ground based optical observations often suffer from interrupted observing runs due to bad weather.
- There arise several statistical issues relating to data gaps, low count rate time bins in time series analysis, issues in spectral fitting due to extremely low source count rates in certain energy channels, etc. all of which need to be dealt with extreme care in order to make meaningful interpretations.

Given these challenges, a number of options *do* exist for pursuing reprocessing studies. The scope and motivation for this thesis is listed below:

- X-ray observatories like Swift, XMM-Newton and now Astrosat, offer simultaneous multi-wavelength X-ray (soft and hard) and optical (and UV) coverage during their observing runs. These missions become extremely crucial in pursuing correlation studies that form the crux of reprocessing.
- In LMXBs, the X-ray luminosity dominates over the optical luminosity by a large factor, as much as 1000. So even if a small fraction of the X-ray emission is reprocessed into the optical, it can be a significant part of the total optical emission. This makes LMXBs ideal candidates for the study of X-ray reprocessing because they offer the perfect setting to probe accretion discs, reprocessing, coronal structures, vertical disc structures and their evolution, all of which are not possible using conventional imaging methods.
- Persistent LMXBs have stable X-ray properties over long periods of time, allowing one to carry out near or non-simultaneous ground based optical observations to further probe reprocessing.

- Compact objects are exotic laboratories to test the current theories of relativity and space-time under extreme gravity. These systems present all possible extremes in terms of temperatures, gravity, matter density, magnetic fields, pressure. By carrying out more and more observational studies in these systems, accurate measurements of binary orbital parameters can be obtained. Such measurements will help understand evolutionary scenarios in a certain population of sources like ultra-compact binaries, LMXBs and milli-second X-ray pulsars.

1.4 Outline of thesis

The work presented in this thesis mainly focuses on Reprocessing, accretion disc structures and evolution in a few individual X-ray binary systems. The rest of the thesis chapters are organized as follows:

- In **Chapter 2**, various kinds of space-based X-ray, space and ground-based optical telescopes and detectors used for this thesis, are discussed. Further, astronomical observation and data analysis strategies are presented.
- In **Chapter 3**, optical studies of the unique LMXB pulsar 4U 1626-67, using the Southern African Large Telescope (SALT), is presented.
- **Chapter 4** discusses detailed studies carried out on the eclipsing LMXB EXO 0748-676 using XMM-Newton. It also covers simulations and modeling of thermonuclear bursts and orbital modulations.
- **Chapter 5** discusses timing and spectral studies of the LMXB eclipsing dipper, XTE J1710-281, particularly considering accretion disc wind emission scenarios.
- In **Chapter 6**, a summary of Chapters 3, 4 and 5 is presented along with discussion on future prospects.
- In **Chapter 6**, a summary of Chapters 3, 4 and 5 is presented along with discussion on future prospects.

Chapter 2

Telescopic systems and analysis methodologies

2.1 Ground based optical astronomy

Optical astronomy is the oldest form of astronomy that developed centuries ago, when all you needed was to look up at the night sky with your naked eyes. The human eye, with its limited sensitivity in the narrow optical regime of 400-700 nm, was in those days, sufficient to discern patterns of planetary motions, particularly eclipses and conjunctions, constellation patterns, star positions and sometimes, their intensity fluctuations. Years and years of naked eye observations necessitated the development of the first set of lenses and telescopes that could magnify images and increase sensitivity. Most ground-based research-oriented optical telescopes are large reflectors that adopt an alt-azimuth mount, which allows for separate altitude (up-down) and azimuth (side-to-side) motions. Incoming photons are reflected off the primary mirror, through a series of secondary mirror segments and further optics, into detectors located at their focal planes. Photon-detectors have also evolved from the good old retina in the human eye to the photo-electric single channel devices like the Photo-Multiplier Tubes (PMTs), and more recently, to semi-conductor based Charged Coupled Devices (CCDs). Observatories are typically located at high altitudes to minimize atmospheric turbulence effects, and sparsely populated places that ensure dark skies devoid of light pollution. Figure 2.1 shows a world map of all the currently operating large ground-based optical telescopes in the world[1]. Optical photometric observations from the 10 meter-class Southern African Large Telescope (SALT) has been used to study the LMXB pulsar 4U 1626-67, as elaborated in Chapter 3 of this thesis.

[1] http://www.atnf.csiro.au/outreach//education/senior/astrophysics/images/resolution/telescopelocations.jpg

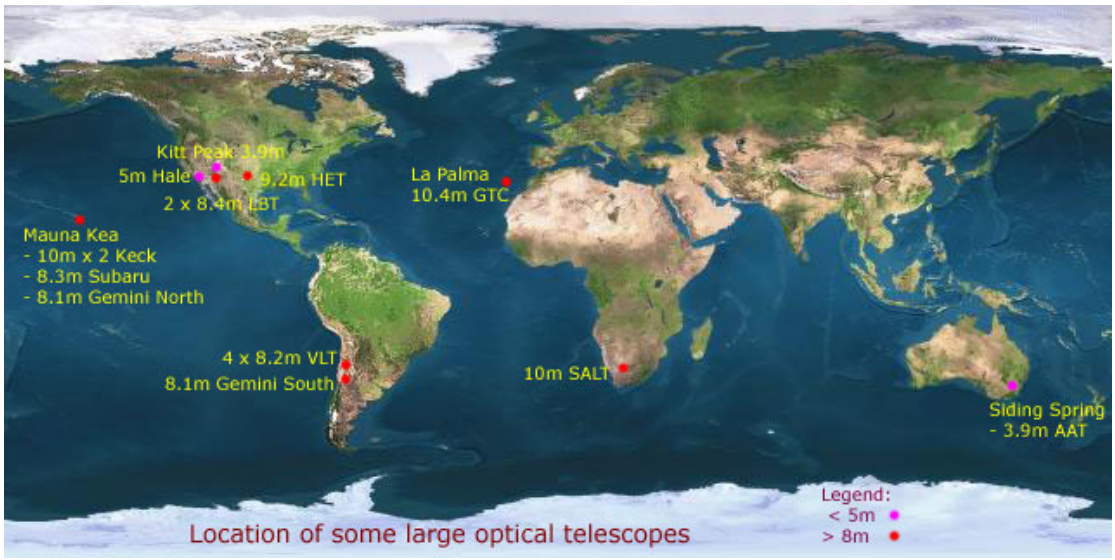

Fig. 2.1 Image shows locations of the world's largest ground-based optical telescopes.

2.1.1 Photometry

Optical photometry involves collecting photons using various wavelength filters into a detector at specified time intervals. A time-series is then generated by observing intensity variations as a function of time. The quality of observing conditions in a given place is dictated by a number of factors which are described below:

- **Air mass:** The thickness of air layer through which incoming photons have to pass through or the air mass (X), which is a function of the zenith angle Z, is specified by X=sec(Z). Observations are typically not carried out below an altitude of 30 degrees.

$$X = sec(Z)sec(Z) = sin(\phi)sin(\delta) + cos(\phi)cos(\delta)cosH \tag{2.1}$$

  where, ϕ and δ are the latitude of the location, and declination of the object, respectively and H is the hour angle (Local Sidereal Time LST - RA).

- **Extinction:** When photons pass through the earth's atmosphere, there is dimming of star-light due to absorption and scattering by the intervening medium. This is termed as Extinction and is expressed in units of magnitude/air mass.

- **Seeing and Scintillation:** Seeing and scintillation effects are both a measure of atmospheric turbulence. Variations in temperature and refractive indices across various layers of the atmosphere can result in the path of light getting distorted due to which the image of a star on the detector spreads over many pixels. Seeing is the effect where the fluctuations due to atmospheric turbulence result in random motion of the image and is measured in arc-seconds. Scintillation, more commonly known as twinkling is a change in brightness due to passage of stellar light through the turbulent atmosphere. By taking large exposures, the fluctuations causing scintillation can be averaged out.

The use of imaging CCD detectors in modern day telescopes is invaluable. A CCD camera is made of silicon wafer segmented into an array of individual light sensitive cells or pixels. Pixels act like light buckets, where incoming photons create electrons via the photoelectric effect. The number of electrons generated by each photon is expressed as Analog-to-Digital units (ADU) and is specified as the gain of the CCD. Over time, exposure to photons produces an image that is read-out by shifting the information out of the pixels to a read-out register. The photons are converted to charges and finally to a voltage for measurement. The voltage is converted to a digital unit to produce a two-dimensional image.

The most important parameter that decides the quality of the observation is the Signal-to-Noise ratio, which is dictated by the integration time as well as various sources of noise.

$$\frac{S}{N} = \frac{signal}{\sqrt{noise_1^2 + noise_2^2 + ... + noise_n^2}} \tag{2.2}$$

By putting in all the sources of noise, the exact CCD equation reads as

$$\frac{S}{N} = \frac{N_s}{\sqrt{N_s + n_{pix}(N_{bkg} + N_{dark} + N_{read-out}^2)}} \tag{2.3}$$

where,
N_s = total number of source photons collected (the product of the gain and ADU) on n_{pix} number of pixels,
N_{bkg} = number of photons/pixel from sky background,
N_{dark} = number of dark current electrons/pixel,

$N_{read-out}$ = read noise electrons/pixel

For modern day CCDs, dark current is negligible. For bright objects, N_s dominates, making the S/N $\sim\sqrt{N_s}$. For high time resolution observations with short exposures, read-out noise becomes more important.

The plate scale for a telescope is defined as the number of arc-seconds corresponding to the pixel size at the detector in the focal plane. It is a function of the focal length (f) of the primary mirror and the CCD pixel size (μ in microns). It is usually calculated using

$$P = \frac{206265 \ \ \mu}{1000 \ \ \mathrm{f}} \ \ \text{arcsec/pixel} \tag{2.4}$$

The plate scale is usually optimized considering seeing conditions. For a typical seeing of an arc second, having a plate scale of 0.5 arc-seconds/pixel is ideal. This would ensure that the entire image of the star falls in two pixels at the most.

The Point Spread Function (PSF) is the response of any given imaging system to a point source. To obtain a sharp image, the 2-dimensional intensity distribution of a point source on a CCD must be spread over a fewer number of pixels. Mainly, the telescopic system's aperture and the atmospheric seeing contribute to the functional form of the PSF.

2.1.2 Image processing using IRAF & SExtractor

Image Reduction and Analysis Facility (IRAF) is a software used for reduction of astronomical images developed at the National Optical Astronomy Observatory (NOAO) [2]. It has a set of tools and packages that are used for processing raw CCD images.

The basic steps for reduction of optical CCD images are as follows:

- **Bias subtraction:** A bias frame is obtained by giving a zero second exposure to the CCD to obtain the offset value. A number of bias frames are taken and averaged to obtain a master bias which is subtracted from all the data images. Sometimes, in order to avoid negative values, a high positive bias value is added to the offset.

[2]Image Reduction and Analysis Facility, http://iraf.noao.edu

- **Trimming:** The overscan region in a CCD image is trimmed for further processing.
- **Cosmic ray correction:** High energy particles, mostly protons, from space generate a shower of secondary particles which are also stopped by the Silicon layer in a CCD. This generates a few thousand electrons that are usually distributed over a few pixels on a CCD. Such events are cleaned and corrected for.
- **Flat fielding**: In order to account for non-uniform sensitivities of each pixel (in terms of the number of ADUs generated per photon), the CCD is exposed to uniform illumination like the twilight sky or the telescope dome. A number of such flat frames are averaged and the raw CCD images are normalized using the Master flat.

SExtractor is another software tool that uses a number of algorithms to extract a catalogue of objects from moderately crowded fields in any astronomical image. It can be used to carry out aperture photometry on processed images. The magnitude and fluxes of the stars in a field can be extracted, by specifying the aperture and PSF details. A time-series can then be generated for further analysis.

Differential Photometry: In order to calibrate the intensity measurements and fluctuations, particularly in time-series analysis, photometry of the target star, as well as a few comparison stars in the field of view, is carried out. Since all the stars in the field, including the target star, are observed at the same time, with the same filters, through the same optical instruments, they are all viewed through the exact same optical path length. This allows for a differential analysis by which all the common variables drop out. It ensures that the differential light curve is solely the intensity variations of the target star, unaffected by intervening atmospheric effects.

2.1.3 Southern African Large Telescope (SALT)

SALT is the largest operating optical telescope in the Southern Hemisphere. It is a 10 meter-class telescope located in the Sutherland outstation of the South African Astronomical Observatory (Buckley, 2001). Situated far from city-lights, and at an altitude of 1.8 meters above sea-level, the SALT site offers excellent seeing conditions of about 0.9 arc-seconds (FWHM), 50% photometric conditions and 75% spectroscopic conditions, on an average. The primary mirror array on SALT is a segmented dish of

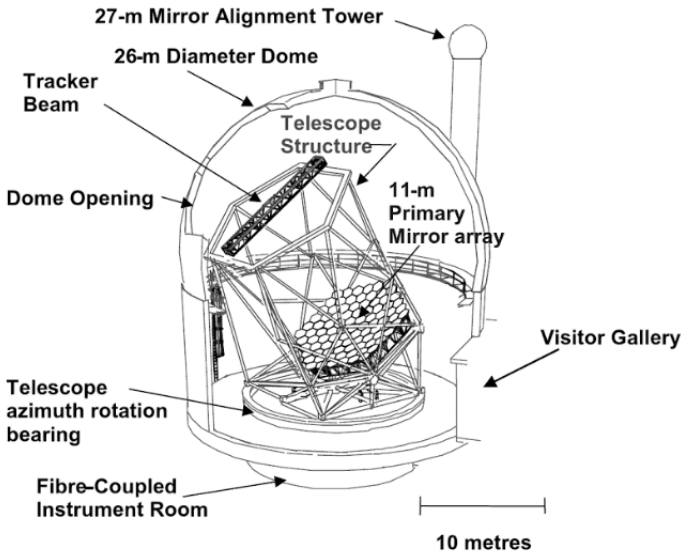

Fig. 2.2 Schematic of SALT adapted from Buckley (2001).

diameter 11 meters, with 91 identical hexagonal mirror segments and a focal ratio of f/4.2. The maximum effective collecting area is ∼60 m^2. The light from the primary is directed towards a Spherical Aberration Corrector (that provides a 8 arc minute field of view), which is mounted on a tracker at the prime focus (O'Donoghue, 2000). The instrument design is based on the Hobby-Eberly Telescope (HET) at McDonald Observatory, Texas and is an optical analogue of the Arecibo Radio telescope. It is fixed at a constant elevation of 37° from the vertical (Buckley et al., 2006; O'Donoghue et al., 2006) and thus allows for an accessible declination range between +10.5° to -75.3°. It has a full 360° azimuth rotation. During a given observation, the telescope super-structure is stationary and the tracker beam allows for targets to be followed for 12° across the sky. This gives an observing time of nearly 2 hours twice as the target drifts through the annulus.

Figure 2.2 shows the schematic of the SALT telescope and its components. SALT comprises of three science instruments, the SALTICAM, the RSS (Robert Stobie Spectrograph) and the HRS (High Resolution echelle spectrograph). All three instruments operate over the UV-visible band of 320-800 nm. The SALTICAM detector (Buckley et al. 2003) on the SALT telescope is dual-purpose optical imager that serves as an acquisition camera as well as a scientific imaging photometer with high time resolution capabilities. It consists of two E2V CCD 44-82 chips, separated by 1.5 mm, and a filter wheel. The filter set available is the Jounson-Cousins U, B, V, R and I. The incoming

photons are collected by the two CCDs, each having two read-out amplifiers. The read-out noise is usually less than 3 electrons per pixel. It employs frame-transfer CCDs operating between 10-20 Hz with minimal dead-time (a few ms). The SALTICAM can be operated in various modes. For hight speed differential photometry, slot-mode provides a fast read-out; a sampling time of 0.2 seconds can be achieved, if pixels are binned 3×3. Pixel binning allows spilling of light into fewer bins, thus increasing the SNR. Photometric data from SALTICAM has been used to study the ultra-compact X-ray binary pulsar 4U 1626-67 and the results of the study are detailed in Chapter 3 of this thesis.

2.2 Space based X-ray Astronomy

2.2.1 X-ray telescopes

Introduction

X-ray photons are way more energetic ($E_\nu \sim$ keV) compared to optical photons ($E_\nu \sim$ eV). They, however, end up getting absorbed in the upper atmosphere, which makes ground-based detection of X-ray photons impossible, unlike the more transparent optical window of the electromagnetic spectrum. All X-ray telescopes are therefore launched into orbit way above the atmosphere ($\sim$ hundreds of km altitude). Since X-ray observatories are space-based, building enormous telescopes and launching them becomes a technological challenge. Also, conventional optical instruments like lenses and mirrors are incapable of reflecting X-rays and focussing them into a detector.

Focussing X-rays

With the advent of new technologies in the last 40 years or so, focussing X-rays has become possible. X-ray telescopes comprise of mirror surfaces that specularly reflect X-rays under two conditions. First, when the incoming X-ray photons strike at grazing incidence and secondly, when constructive interference takes place between X-rays reflected from many layers of a material with high electron densities. These mirrors are coated alternately with high atomic number (Z) high reflectance metals (like Iridium, Gold and Tungsten) and low Z materials. X-rays are reflected at each layer and the optical thickness of each layer is chosen so as to produce a constructive interference between the layers. A simple parabolic mirror design was proposed and used by the founders of X-ray astronomy, Ricardo Giacconi and Bruno Rossi. Hans Wolter, in 1952,

showed that a paraboloid primary mirror followed by a hyperboloid secondary, served as a better focussing system for X-rays. Such mirror combinations are often nested within one another to increase the effective collecting area, as shown in Figure 2.3. Each mirror pair is co-aligned and also confocal. The inner shells have graze angles shallower and hence reflect higher energy X-rays than the outer shells. Such focussing mirrors have been used in Chandra and XMM-Newton telescopes.

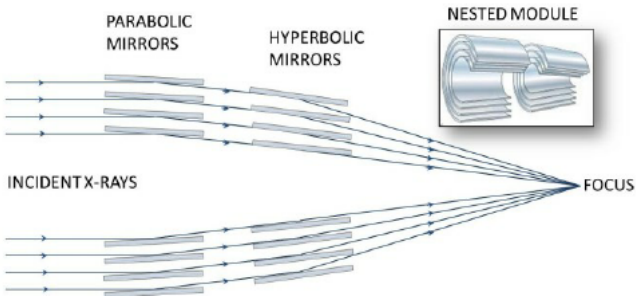

Fig. 2.3 Schematic of the Wolter design for focussing X-rays (Gaskin et al., 2015).

X-ray detectors

Each X-ray mission has been specifically designed to excel in one or more of the following capabilities: imaging, measuring the X-ray photon energy with high sensitivity, precise tagging of the arrival-time of each photon, etc. The main goal of all these missions is to offer maximum collecting area and collect minimum background. X-ray optics and detector designs vary significantly between telescopes that address different science goals pertaining to timing, spectroscopy, imaging or polarization. The different detector types used in various missions, as used for this thesis work, are discussed below:

1. Proportional counters

Proportional counters were one of the early detectors after the Geiger counter, designed for X-ray and cosmic ray measurements and are still widely used by many missions. The main proportional counter volume is filled with a noble gas mixture (Argon, Methane, Xenon or Neon) and is maintained at a pressure value of a few atmospheres. In order to reduce background, a collimator is used to restrict the field of view. A thin window (mica, plastic or Beryllium) is placed over the main volume, optimized such that it allows X-rays to pass through, but at the same time, withstands the internal gas pressure and prevents any gas leak. Each incoming X-ray photon passes through the window and is absorbed by the gas atoms, creating photoelectrons and

positive ions. The photoelectron, with a kinetic energy E_e (X-ray photon energy - electron binding energy) goes on to ionize more atoms and creates N=E/W number of further photoelectrons, where W is the ionization potential of the gas, typically W$\sim$30 eV. A central wire or anode, maintained at about +2000 Volts, attracts the electrons towards it. As the electrons drift towards the anode, they further photo-ionize other gas atoms and leave a trail of electrons and ions.The charge measured at the anode is then proportional to the number of electrons generated. The amplified signal is measured at the detector output as a *pulse-height spectrum*, which is proportional to the energy of the incoming X-ray photon. The gain obtained in such a system is about 10^4-10^5. Resistive anode wires are used in some position sensitive proportional counters in order to trace back the exact location of the incident X-ray photon.

A large flux of cosmic rays usually bombard the telescope-carrying satellite as well as the proportional counter volume, leaving trails similar to X-ray photons. This is why sometimes, guard counters or veto layers are used alongside the main proportional counter in order to reject cosmic ray events. Simultaneous detection of an event by both the counters (or several anode layers), identifies a charged particle event and can be rejected by anti-coincidence electronic logic. A few space X-ray observatories with proportional counter detectors include the *Röntgen Satellite (ROSAT)*, the *Rossi X-ray Timing Explorer (RXTE)* and the recently launched *Large Area Proportional counter (LAXPC)* on board ASTROSAT.

2. Charged Couple Devices (CCDs)

X-ray CCD detectors are most sought after for imaging purposes. They are largely similar to the optical CCDs. These devices have pixel arrays, each pixel operating as a potential well for incoming X-ray photons. They work on the principle of the photo-electric effect. Unlike in the optical scenario, where each photon generates one electron-hole pair, in X-ray CCDs, each X-ray photon produces multiple electron-hole pairs. Thus CCDs are operated in a photon counting mode where the resulting pulses measured are proportional to the original photon's energy. Data is recorded at fixed time intervals. The charge deposited on each row of the pixel array is transferred to the subsequent row and is read-out row-by-row. By choosing fewer pixel array rows, faster readout times can be achieved. Within the time window of a single event being sampled, a number of times, multiple photons impinge on the same pixel. Such an event produces a larger photon energy and is read-out as a single event. This kind of an issue is termed as photon *pile-up* that occurs for unusually bright sources. This effect

distorts the spectral information and renders spectroscopic measurements unreliable. *Pile-up* correction involves discarding the central few pixels or sometimes, modeling the pile-up effects. A few X-ray missions that utilize CCD detectors are *XMM-Newton, Chandra, Swift*, etc.

Comparison of mission capabilities:

A number of X-ray missions have been used for the study of the different X-ray sources in this thesis. A brief description of each mission is provided in the text below and a summary of their specifications is given in Table 2.1.

1. XMM-Newton

The X-ray Multi-Mirror Mission, named in honor of Sir Isaac Newton, was launched in 1999 by the European Space Agency (ESA) and is still operational as of today (mid-2017). The satellite is placed in a highly elliptical orbit with a 47.8 hour period (7000 km perigee and 114000 km apogee) and at an orbital inclination of 47.8°. This is so, for a number of scientific and operational reasons, one of which is to avoid the Earth's radiation belt that could lead to degradation of the CCD cameras on-board. The telescope payload consists of three co-aligned 7.5 meter focal length X-ray telescopes. The European Photon Imaging Camera (EPIC) comprises of the PN (Strüder et al., 2001) and Metal Oxide Semi-conductor (MOS, Turner et al. 2001) CCD arrays, that provide moderate spectral resolution in the energy range 0.1-15 keV. With multiple data collection modes, the telescope allows optimization of required imaging performance and timing resolution, while maximizing count rate. This observatory also comes with a co-aligned 30 cm Ritchen-Chretien optical/UV telescope called the Optical Monitor (OM). This provides simultaneous UV/optical information along with X-ray and assists in determining the optical state of the X-ray source and also its variability. A number of broad and narrow band filters including the Johnson-Cousins UBVRI bands are provided. The limiting sensitivity of the OM in the B band is 24. XMM-Newton, with its enormous X-ray photon collecting area and its ability to conduct uninterrupted long simultaneous X-ray and optical observations, proved invaluable for reprocessing studies, as elaborated in Chapter 4 of this thesis.

2. RXTE-PCA

The Rossi X-ray Timing Explorer was launched in 1995 by NASA and was decommissioned in 2012 after 16 long years of providing spectacular scientific results in X-ray

Timing. The satellite was launched into a low earth circular orbit at an altitude of 580 km and an inclination of 23°, corresponding to an orbital period of 90 minutes. The telescope was aimed at studying variability in X-ray sources and was built using large area proportional counters that provided unprecedented timing resolution of micro-seconds and a moderate spectral resolution in a wide energy band of 2 - 250 keV. The three instruments aboard the satellite were the Proportional Counter Array (PCA), co-pointed with the High Energy X-ray Timing Experiment (HEXTE) and the All-Sky Monitor (ASM). The PCA consisted of an array of 5 large area proportional counters with a total collecting area of 6500 cm^2. The proportional counters were filled with Xenon gas. The sensitivity of the PCA proved to be 0.1 milli-crab. To restrict the large background, a 1 degree FWHM collimator was used. The three wide-angled shadow cameras on the ASM, with a collecting area of 90 cm^2, were equipped with position sensitive proportional counters also filled with Xenon gas. The ASM independently scanned 70% of the entire sky, during each satellite orbit, with a wide field of view, every 100 seconds. Such scans proved to be extremely useful to detect X-ray transient phenomena and also to collect a long term history of all the different X-ray sources. Data from RXTE-PCA and ASM has been utilized to explore transient phenomena called Quasi Periodic Oscillations (QPOs) and flares in the X-ray pulsar 4U 1626-67 as is elaborated in Chapter 3 of this thesis.

3. Chandra

NASA's Chandra X-ray Observatory, one of the most sophisticated astronomy missions ever, was launched in 1999. The spacecraft has a high Earth elliptical orbit with a 16000 km perihelion distance and a 64 hour orbital period, ensuring long uninterrupted observing time and more duty cycle (∼85%). The X-ray telescope consists of four pairs (parabolic and hyperbolic) of nested mirrors, that focuses X-rays into the detector at the focal plane, located about 9.2 meters away. The focal plane instruments are the Advanced CCD Imaging Spectrometer (ACIS) and the High Resolution Camera (HRC). The ACIS-I is a 2x2 and the ACIS-S is a 6x1 array of large format (2.5 sq. cm) CCDs that provide high resolution spectrometric imaging. The telescope also has high resolution dispersive spectroscopic capabilities in the form of the High, Medium and Low Energy Transmission Gratings (HETG , METG and LETG) operating at the energy ranges 0.8 - 10.0 keV, 0.4 - 5.0 keV and 0.2 - 8.8 keV respectively. The ACIS-S serves as the primary readout detector for the Transmission Gratings (Weisskopf et al., 2000). Data from the Chandra ACIS-S and the HETG has been used to explore the

spectral properties of the eclipsing binary XTE J1710-281, as is further discussed in Chapter 5.

4. Suzaku

The Suzaku mission was Japan's fifth Astronomy mission developed by the Japan Space Exploration Agency (JAXA) in collaboration with NASA. The spacecraft was launched in 2005 into a circular orbit at an altitude of about 550 km with a 31° inclination and successfully operated till 2015 when it was de-commissioned. It covered a broad-band energy range between 0.2-600 keV with its two co-aligned instruments, the imaging X-ray Telescope (XRT) and the non-imaging collimated Hard X-ray Detector (HXD). The non-dispersive X-ray Imaging Spectrometer (XIS), comprising of four imaging CCDs (three of them front illuminated and one back illuminated), was located at the focal plane of the XRT. The high spectral resolution of the XIS CCDs has been used to identify crucial high ionization Fe lines in the high inclination dipper XTE J1710-281, as is further elaborated in Chapter 5.

5. Swift

The Swift mission, part of NASA's medium explorer program (MIDEX), was launched in 2004 into a 600 km low-earth circular orbit with an inclination of 20.6°. The telescope payload comprises of three instruments, the Burst Alert Telescope (BAT), the X-ray Telescope (XRT) and the UV/Optical Telescope (UVOT) which simultaneously provide rapid identification and multi wave band follow-up of transient events (Burrows et al., 2005). The BAT, with a large field of view between 15 - 150 keV and a high sensitivity between 15 - 150 keV, specifies the position of an event within 20 seconds of it occurring and relays it to the ground. Soon after, the spacecraft, in less than 90 seconds, maneuvers and re-orients to the source position. The XRT detector element comprises of an EPIC-PN CCD (similar to the one used for XMM-Newton) and has multiple modes of operation like the Photon Counting mode, Integrated Imaging mode and Rapid Timing mode in order to optimize imaging and read-out time. The UVOT, similar to the OM aboard the XMM-Newton mission, is a 30 cm Modified Ritchey-Chretien telescope which operates with a CCD detector in the Photon counting mode up to a limiting magnitude of B$\sim$24. A near-simultaneous Swift-XRT observation was carried out along with an optical SALT observation and has been used to study the X-ray state of the LMXB pulsar 4U 1626-67, as is subsequently discussed in Chapter 3.

Table 2.1 Comparison of capabilities of the different X-ray instruments used for data analysis in this thesis, from various past and currently operating X-ray missions.

Mission	Instrument	Effective area (cm^2)	Energy range (keV)	Angular Resolution	Field of view	Spectral Resolution (eV)	Timing Resolution	Capability
XMM-Newton	EPIC-PN	1300 at 1.5 keV	0.2-12	6"	30'	130 at 6 keV	73 ms	Broadband Spectro-Photometry
	OM		180-600 nm		17'		0.5 s	Simultaneous optical
RXTE	PCA	5000 at 5 keV	2-60	1 deg	1 deg	1300 at 6 keV	1 μs	Fast Timing
Chandra	ACIS	525 at 1.5 keV	0.1-10	1"	17'x17'	130 at 6 keV		Imaging and Spectroscopy
	ACIS/HETG	45 at 1.5 keV	0.6-10			29 at 6 keV		Grating spectroscopy
Suzaku	XIS	1600 at 1.0 eV	0.2-12	<1.5'	19'x19'	120 at 6 keV		Spectroscopy
Swift	XRT	110 at 1.5 keV	0.2-10	5'	23.6'×23.6'			Timing and spectroscopy
Astrosat	LAXPC	6000	3-80		1 deg × 1 deg		10 μs	Fast Timing

2.2.2 X-ray data analysis methods

X-ray data in its rawest form is photon information with respect to their arrival time, energy, position and spatial distribution on a CCD and their polarization. It is essential to extract this information accurately for a telescope, given the specifics about the telescope's optics, energy response characteristics and satellite orbital parameters. Also, since counting X-ray photons is a Poisson process, each recorded photon comes with an associated Poisson noise of the order of $\sqrt{N}$, where N is the count rate recorded in each time bin. The High Energetic Astrophysics Science Archive Research Center (HEASARC) is the primary archive for obtaining astronomical data from almost all current and past, space and ground based observatories operating in a wide range of the electromagnetic spectrum, particularly the high energy end. Data is obtained from the HEASARC and is further processed and analyzed using the HEASOFT software. All X-ray data analysis procedures require the input file format to be in a Flexible Image Transport System (FITS) format. FITS is a digital file format that is used for easy storing and processing of scientific images. All image metadata is stored in the header in human readable ASCII format. FITS is also used to store non-image data like spectra, photon counts, structured data with several extensions. FTOOLS is a general package comprising of software that can be used to manipulate (create, examine or modify) FITS format data files and is supported by many different operating system environments. The various timing and spectral software packages and their respective tasks, elaborated below, produce simple and user-friendly output scientific graphs using the default graphics plotting subroutine library, *PGPLOT* [3].

[3]https://www.scribd.com/document/39702200/Pgplot-Manual

Timing analysis

XRONOS: The '*XRONOS*' is a sub-package of the FTOOLS. It is a timing analysis package that includes various tasks required for time-series analysis. The different processes involved in a timing study of X-ray data and their specific analysis tools are discussed below:

1. Time-series: Time-series analysis is extremely crucial in X-ray timing studies. It involves recording information of photon count rate as a function time. Such a plot of count rate versus time is termed as a light curve. A number of periodic, non-periodic, bursting and flaring phenomena can be visualized in a light curve. The accretion state of the source, as to when it is quiescence or when it is highly accreting can also be determined by looking at the count rate level in the light curve. This kind of study is identical to optical photometry and can also be carried out in multiple X-ray energy bands. Intensity variations as a function of energy allows for determining the source of the underlying physical phenomenon. Hardness ratio, calculated as the ratio of the count rate in the hard X-ray band with respect to the soft band determines whether the dominant photon flux is hard or soft and gives the corresponding fraction. Such a ratio is also termed as 'color' and can be used to plot a color-color diagram between photon count rate ratios in multiple energy bands. X-ray sources tend to follow a certain path in the color-color diagram during different luminosity states and are duly classified as Z or Atoll sources. The following task are used for studying time-series, hardness ratios as well as color-color diagrams of a given source.

- lcurve: The *lcurve* task produces a light curve plot given an input event file or binned data file in a FITS extension. Time, exposure as well as phase windows can be applied to filter the time-series. Data can be re-binned and divided into multiple intervals and plotted in multiple frames. The task also allows for plotting multiple time-series, hardness and color-color diagrams together, when required.

2. Period search: To carry out any general period search, a number of techniques like Fourier methods, phase folding methods, etc. are adopted. The most commonly adopted Lomb Scargle periodogram adopts the Least Squares method. This involves fitting the data to a model at each frequency and selecting the frequency that maximizes the likelihood (Lomb, 1976; VanderPlas, 2017).

- efsearch: This task is employed to look for periodicities in a time-series. It folds the data over a specified period range and determines the variations of the folded data with respect to a model function. The task determines the chi-square for all the periods and identifies the best period and plots the same.

For evenly binned time-series data, a Fast Fourier Transform algorithm can be used to convert the signal from the time domain to the frequency domain and look for periodicities. A Power Density Spectrum (PDS) constitutes the Fourier Transform of the auto-correlation function of the time-series. The PDS gives the amplitudes of the different frequency components present in the time-series data. The light curve is usually segmented and the power spectra is computed for each of these segments, and later averaged. Narrow frequency components can be explored with sufficiently long datasets.

A light curve of length T, with N_{ph} photons, has a time resolution of T/N, where N is the number of time bins. Assuming x_k represents the number of photons detected in bin k (k=0,N-1), this gives the total number of photons as the sum of all the photons from all bins, $N_{ph} = \Sigma_{k=0}^{N-1} x_k$. The Fourier transform of this time series, with a Fourier amplitude a_j is given by,

$$a_j = \Sigma_{k=0}^{N-1} x_k \; e^{2\pi ijk/N} (j = 0, N/2) \tag{2.5}$$

Parseval's theorem states that the sum of the square of a function is equal to the sum of the square of its Fourier transform.

$$\Sigma_{k=0}^{N-1} |x_k|^2 = \frac{1}{N} \Sigma_{j=-N/2}^{N/2-1} |a_j|^2 \tag{2.6}$$

The variance in the light curve data can then be expressed in terms of the Fourier amplitudes a_j as,

$$Var(x_k) = \frac{1}{N} \Sigma_{j=-N/2}^{N/2-1} |a_j|^2 \tag{2.7}$$

By incorporating the Leahy normalization (Leahy et al., 1983), the power in each frequency bin j is,

$$P_j = \frac{2}{N_{ph}} |a_j|^2, j = 0, ..., N/2 \tag{2.8}$$

Giving the total variance as,

$$Var(x_k) = \frac{N_{ph}}{N} (\Sigma_{j=1}^{N/2-1} P_j + \frac{1}{2} P_{N/2}) \tag{2.9}$$

The fractional root mean square (rms) variation is then expressed as

$$r = \frac{\sqrt{\frac{1}{N} Var(x_k)}}{\bar{x}} = \sqrt{\frac{\Sigma_{j=1}^{N/2-1} P_j + \frac{1}{2} P_{N/2}}{N_{ph}}} \tag{2.10}$$

The fractional rms $(\text{rms/mean})^2$ Hz^{-1} is then plotted as a function of frequency in logarithmic scale.

- powspec: This task computes the power spectral density of an input time-series by an FFT algorithm or a direct slow Fourier algorithm. The power spectra can then be normalized such that the integral gives the squared rms fractional variability. The expected white noise level can also be subtracted from the time-series data. The output can also be binned logarithmically.

3. Folding: The time-series can be stacked at regular intervals and count rates can be averaged at each bin. This generates what is known as a folded profile. The folded profile describes the average count rate at different phases. For example, in pulsars, a time-series folded at their pulse period results in a pulse profile which represents the emission geometry of the region emitting the pulsed component as a function of pulse phase. Their time-series can also be folded by the orbital period, to obtain an orbital average profile, that describes their average orbital intensity modulation as a function of orbital phase.

- efold: This task folds the input time-series with a specified period, by averaging the count rates in corresponding bins and produces a folded profile. A number of time, exposure and phase windows can be used to filter data.

4. Cross correlation: Cross correlation measures how closely any two given different time-series resemble one another at a certain delay. The cross correlation between two time series f(t) and g(t) is given by,

$$(f \times g)(\tau) = \int f(t) g(t + \tau) dt \tag{2.11}$$

where τ is the delay.

It provides details on delays, advances between the two time-series observations. X-ray and optical correlation studies have been dealt with in detail in Chapter 4.

- crosscor: This task computes the CCF between any two given time-series data.

Spectroscopy

Spectroscopy involves studying the X-ray photon flux as a function of energy and is carried out by spectrometers that operate at different energy bands. The X-ray spectral information as measured by a spectrometer, is photon counts as a function of channel, I. This measured spectrum C(I) can be described as follows:

$$C(I) = \int f(E)R(I,E)dE \tag{2.12}$$

where, the measured spectrum C(I) is the result of the convolution of the actual source spectrum f(E) with the instrumental response R(I,E). The instrument response is proportional to the probability that a measured photon of energy E is detected in a channel I. Since this equation is not invertible, obtaining f(E) directly, is not possible. An alternative method is to chose a model spectrum f$^{'}$(E) that can be described by several parameters p1, p2, ..etc. This is convolved with the instrument response to obtain a predicted spectrum C_p(I). The predicted spectrum and the measured spectrum are then compared using a fit statistic to judge whether the model spectrum fits the observed data.

There are two fit statistics (both derived from the more general Maximum Likelihood Analysis) that are typically employed to assert the goodness of fit, the χ^2 and the C-statistic. When the count rate in each bin is high enough to be considered gaussian distributed, the χ^2 statistic is employed. If the count rates are lower than say, 20, the spectra are re-binned to obtain at least 20-30 counts per bin using the FTOOL task *grppha*, after which a valid χ^2 statistic can be applied. The χ^2 statistic is defined as:

$$\chi^2 = \Sigma \frac{(C(I) - C_p(I))^2}{(\sigma(I))^2} \tag{2.13}$$

where, $\sigma(I)$ is the error on the measured count rates, typically expressed as $\sqrt{C(I)}$, assuming the photon counting is a Poissonian process. In certain cases, the count rate in each bin is small enough and re-binning is not an option. In such cases, assuming a gaussian distribution becomes no longer valid and a maximum likelihood analysis (Cash 1968), results in the C-statistic which is given by:

$$C = -2 \log L \tag{2.14}$$

where L, the Likelihood, is given as Π_i p(d_i | m_i) .
Such a statistic cannot be however applied to background subtracted data, since the difference between two Poisson distributed variables is not Poisson distributed.

The goodness of fit, for a given number of degrees of freedom (d.o.f = number of channels - number of model parameters) and a given confidence interval for a χ^2 statistic, is typically assessed by the reduced χ^2 or the $\frac{\chi^2}{d.o.f}$. If the reduced χ^2 is nearly 1, the model describes the data well, if it much less than one, the errors are over estimated and if it is more than 1, the model parameters of the current model or the model itself needs to be modified. Spectral fitting is iteratively carried out before arriving at the lowest reduced χ^2. The model parameters so obtained become the best fit model parameters.

The basic forward fitting algorithm used for analyzing X-ray spectra involves the following steps:
Step 1: Chose a model spectrum M(E) that is best thought to represent the observed spectrum and provide reasonable estimates of the model parameters.
Step 2: Multiply this spectrum by the telescope effective area.
Step 3: Further convolve it with the telescope's instrument response, to obtain the predicted count spectrum that a spectrometer would detect in a given channel for such a model.
Step 4: Compare the obtained result (predicted spectrum) with the data measured by the spectral device using an appropriate fit statistic.
Step 5: Repeat all the above steps each time by modifying the model spectra and their parameters until a desired value of the fit-statistic is obtained.
Step 6: Obtain the confidence intervals for the best fit model parameters.

X-ray spectral data is fitted using a number of packages like XSPEC, ISIS, Sherpa, etc. The XSPEC package and its models that have been used in this thesis for analyzing spectra from Chandra and Suzaku observations, are discussed below:

XSPEC: XSPEC is a command-driven, interactive X-ray spectral fitting package developed jointly by ESA's EXOSAT project and NASA/GSFC's HEASARC (Arnaud, 1996). It is completely independent of the detector and hence is used for data obtained from any kind of spectrometer. XSPEC uses the PGPLOT as its default plotting device. XSPEC comes with a number of in-built spectral models and also allows for

developing one's own models. Any given spectral data is built as a combination of multiple individual model components that can be multiplicative and/or additive. The following are some of the individual XSPEC models used for the thesis:

Power law:
This is a phenomenological model used to describe the continuum emission (like Compton, synchrotron) from many different types of X-ray sources. It is a multiplicative model.

$$A(E) = KE^{-\alpha} \tag{2.15}$$

where, α is the photon index of the power law (dimensionless) and K is the normalization parameter (in units of photons/keV/cm^2) at 1 keV.

Blackbody:
This is a physical model used to describe the blackbody emission from the neutron star surface and/or the inner accretion disc. The model is additive and uses the Plank function to describe the blackbody emission.

$$A(E) = \frac{K\ 8.0525\ E^2\ dE}{(kT)^4[exp(\frac{E}{kT}) - 1]} \tag{2.16}$$

where, kT is the temperature in keV and K is the normalization factor given by L_{39}/D_{10}^2.

Photo-electric absorption:
This is a multiplicative model that modifies the underlying continuum model and is used to describe the absorption of X-ray photons by the neutral hydrogen column, along the line of sight.

$$M(E) = exp[-n_H\sigma(E)] \tag{2.17}$$

where, σ(E) is the photo-electric cross-section and n_H is the equivalent hydrogen column density (in units of 10^{22} atoms cm^{-2}).

Partial covering fraction absorption:
This is a multiplicative model that modifies the underlying continuum emission by introducing partial absorption by neutral medium.

$$M(E) = fexp[-n_H\sigma(E)] + (1 - f) \tag{2.18}$$

where, n_H is the equivalent hydrogen column density (in units of 10^{22} atoms cm^{-2}) and f is a dimensionless covering fraction ($0 < f < 1$).

Partial covering absorption by partially ionized material:
This model assumes that a fraction of the source is covered by photo-ionized material (Reeves et al., 2008), while the remaining (1-f) of the spectrum is directly observed. The parameters involved are the column density (in units of 10^{22} atoms cm^{-2}), $\log(\xi)$ where the ionization parameter $\xi = \frac{L}{nr^2}$, f is the covering fraction and z is the redshift.

Gaussian line:
This is an additive model used to describe emission lines with a simple gaussian profile.

$$A(E) = K\frac{1}{\sigma\sqrt{2\pi}}exp\left(\frac{-(E - E_{line})^2}{2\sigma^2}\right) \tag{2.19}$$

where, E_{line} is the line energy in keV, σ is the line width in keV and K is the normalization factor which represents the total number of photons/cm^2/s in the line.

Absorption Edge:
This is a multiplicative model that modifies the continuum by introducing an absorption edge corresponding to certain edge energies of elements.

$$M(E) = \begin{cases} 1 & E < E_c \\ exp[-D(E/E_c)^{-3}] & E > E_c \end{cases} \tag{2.20}$$

where, E_c is the threshold energy in keV and D is the absorption depth at the threshold.

Gaussian absorption:
This is a multiplicative model used to describe absorption lines with a simple gaussian profile.

$$M(E) = exp\left(-\frac{par3}{\sqrt{2\pi}par2}\right)exp\left(-0.5 \times (E - par1/par2)^2\right) \tag{2.21}$$

where par1 is the line energy in keV, par2 is the line width (σ) in keV and par3 is the line depth.

Chapter 3

Pulse reprocessing in 4U 1626-67 using SALT

One part of this chapter is adapted from the paper 'Pulse reprocessing in 4U 1626-67 using SALT' by Raman et al. (2016) published in MNRAS, 458, 1302R and the remaining is based on further study of the system with newer observation with SALT.

3.1 Introduction

A small fraction of the entire LMXB population is observed to exhibit X-ray pulsations. Most of the pulsating LMXBs are Accreting Millisecond Pulsars (AMXP) with a relatively weak magnetic field strength of 10^8-10^9 G. In the recycling scenario of neutron stars, these LMXBs accrete matter and angular momentum from the donor star over extended periods, causing the magnetic field to decay (Bhattacharya and Srinivasan, 1995). If the accretion disc extends down to the stellar surface, the neutron star could get spun-up into milli-second pulsars (Alpar et al., 1982; Bhattacharya and van den Heuvel, 1991). These AMXPs eventually "switch on" as a radio millisecond pulsar (for eg. IGR J18245-2453, Papitto et al. 2013). 4U 1626-67 is one of the very few persistent LMXB pulsars that has high magnetic field strength ($\sim 10^{12}$G) and is not yet an AMXP. Thus, from an evolutionary point of view, this pulsar is an important link between the AMXPs and high magnetic field LMXB pulsars.

4U 1626-67 is an ultra-compact LMXB pulsar, with a magnetic field strength of about 3×10^{12} G, measured using the cyclotron resonance scattering feature detected in the X-ray spectrum (Orlandini et al., 1998; Camero-Arranz et al., 2010). The pulsar has a spin period of about 7.7 s with no evidence of pulse arrival time delay due to orbital motion.The 42 min orbital period was measured from an optical sideband by Middleditch et al. (1981) and the upper limit of the projected semi-major axis was

derived as 10 lt-ms (Rappaport et al., 1977; Levine et al., 1988; Jain et al., 2008). The short orbital period and the faintness of the optical counterpart, indicate an extremely low mass and degenerate secondary star (Levine et al., 1988; Chakrabarty, 1998). It has one of the lowest mass functions ($<1.3 \times 10^{-6}$ $M_{\odot}$, Levine et al. 1988) measured for any X-ray binary. A very low inclination or a nearly face on geometry ($i<10^{\circ}$) does allow for a moderate mass companion. However, the *a priori* probability of finding such a system, is only 0.015. The maximum possible torque that can act on a neutron star during spin-up is when the magnetospheric radius comes very close to the co-rotation radius. Using this, Chakrabarty (1998) calculated the lower limit for the mass transfer rate as 2×10^{-10} $M_{\odot}$ per year and showed that a 0.08 $M_{\odot}$ hydrogen-depleted companion, with an $i<8^{\circ}$ (*a priori* probability of $\sim 1\%$) would satisfy the minimum mass transfer rate criterion and would also put the binary at a distance of 3 kpc. The system shows no type 1 X-ray thermonuclear bursts, but does show frequent X-ray flares.

Accretion torques acting on the neutron star leads to spin up or spin down of the neutron star. These torques are crucial in understanding the interaction between the accretion disc and the magnetosphere. Most accretion powered X-ray pulsars show torque reversals in timescales of weeks to months and years that is often related to the X-ray luminosity (Bildsten et al., 1997). Not only does 4U 1626-67 not show the standard X-ray luminosity-accretion torque relation (Beri et al., 2014), but it has undergone only two such torque reversals in the last 40 years (Chakrabarty et al., 1997; Jain et al., 2010; Camero-Arranz et al., 2010). From the time of its discovery in 1977 till 1990, the source was steadily spinning-up. This era was the first spin-up era (Joss et al., 1978a). In 1990, the first torque reversal was observed and for 18 years the source was steadily spinning down at the rate similar to the spin up rate observed in the first spin-up era (Chakrabarty et al., 1997). In 2008, the source underwent a second torque reversal (Camero-Arranz et al., 2010) after which it is currently steadily spinning up. This is the second spin-up era. The source shows different X-ray features during the spin-up and spin-down eras. For example, the X-ray pulse profiles show a double horned shape during the two spin-up eras, which gets turned into a dip during the spin-down era (Beri et al., 2014). A strong 48 mHz QPO found consistently during the spin-down phase (Kaur et al., 2008), is absent in the power spectrum of the current spin-up phase (Jain et al., 2010), although a weak X-ray QPO was reported by Shinoda et al. (1990) during the first spin-up epoch. The X-ray spectra are similar during the spin-up eras as against the spin-down era (Camero-Arranz et al., 2010). All of these indicate that there are changes in the accretion mode from the inner disc to the

neutron star that are associated with the torque reversals (Beri et al., 2014).

The very faint blue optical counterpart KZ Ter, discovered by McClintock et al. (1977), was found to have a UV excess in its spectrum. The magnitudes obtained with the identified source were not consistent with a main sequence or supergiant companion, but were more likely supportive of a system containing a late type dwarf or a degenerate dwarf where most of the optical light came from reprocessed X-ray flux by an accretion disc and/or the inner face of the companion star (Joss et al., 1978b). Optical pulsations were then detected at the same X-ray pulse period of 7.67 s with a pulsed amplitude of 4% and pulsed energy fraction of 2% (Ilovaisky et al., 1978). It was then established that if the system was an ultra compact binary, then the X-ray heating of the companion must be negligible and that the UV excess seen in the source must be associated with an accretion disc (Crampton and McClure, 1979; Chester, 1979). McClintock et al. (1980) discovered intense correlated X-ray and optical flares and suggested that a large fraction (>8%) of the pulsed emission must be produced within 0.5 light seconds from the neutron star. This established the fact that the pulsed X-rays impinging on the accretion disc gave rise to the observed reprocessed optical pulsations. They found a pulsed amplitude of 6.2%, and showed that the optical pulsations were mainly driven by the 1-3 keV soft X-ray pulsed photons.

In the first spin-up era, along with the main pulsation, a sideband of a slightly lower frequency was observed and explained as reprocessed pulsation from the donor's surface (Middleditch et al., 1981) that was beating with the main pulsation at the orbital period. An orbital period of 42 min and a pulsed fraction of 2.4% was obtained. The sideband and orbital period was confirmed by Chakrabarty (1998). The fact that the side band occurred at a lower frequency indicated that the pulsar spin was in the same direction as the orbital motion. After the first torque reversal, in the spin-down era, Chakrabarty (1998) reported a 48 mHz optical QPO with a fractional rms amplitude of 6-8% in the power density spectrum and a pulsed fraction of 6%. Another 1 mHz QPO was detected by Chakrabarty et al. (2001) without a simultaneous X-ray QPO at that frequency. This was associated with a possible warp in the accretion disc.

Detailed observations in the last four decades have indicated change in accretion mode associated with change in accretion torque (Jain et al., 2010; Beri et al., 2014). In this work the optical temporal characteristics of 4U 1626-67 after the second torque reversal (during its spin-up phase) were investigated in order to re-examine various

Observation	Date	Exposure time (ks)	Observation length (ks)
SALT night 1	2014 March 5	4.8	4.8
SALT night 2	2014 March 6	6.6	6.6
Swift-XRT (00031156002)	2014 March 5	4.6	4.6
RXTE-PCA (95313-01-01-08)	2010 December 9	18.2	20.3
RXTE-PCA (95338-05-01-00)	2010 January 14	10.9	17.1
RXTE-PCA (95338-05-02-00)	2010 January 15	7.3	9.6

Table 3.1 Log of all optical and X-ray observations of 4U 1626-67 used for this work.

features like the relative pulse amplitudes in X-rays and optical, the strength of the previously reported orbital sidebands and the pulse profile evolution. New observations were carried out with the Southern African Large Telescope (SALT) and Swift-XRT. Analysis of archival RXTE data was also carried out in order to examine the pulse characteristics during X-ray flares.

3.2 SALT observation 2014

3.2.1 Observations and data reduction

4U 1626-67 was observed using the SALT for two consecutive nights on 2014 March 5 and 6. The observations were made using the SALTICAM instrument. Details of the observations are given in Table 3.1. The SALTICAM was operated using the V band filter (central wavelength 550 nm). The slot mode gives a fast readout time with practically no dead time. With a 3×3 pixel binning, a sampling time of nearly 0.2 s was achieved. The clocks used for time sampling produced a binning of 0.203 or 0.204 s. For a very small fraction of the observation, the binning is uneven, separated by 0.1 or 0.6 s. It is noted here that the instrument configuration was identical on the two nights and therefore the difference between the results obtained on the two nights of observation are not due to any instrumental artifact. The photons are collected by two CCDs separated by 1.5 mm, each with two readout amplifiers. The readout noise is less than 3 electrons pixel^{-1}. The gain specified was 2.6 electron per ADU.

The bias subtracted SALT data were first extracted using the package `IRAF`. The target star and two other comparison stars were chosen from a single amplifier (see Figure 3.1). The image frames that contained these stars were then further processed. The overscan regions in the raw images were trimmed. An aperture photometry was then carried out on these images using the `SEXTRACTOR` software. The magnitude

and fluxes of the target star and comparison stars were extracted using an aperture with inner and outer radii as 16 and 25 pixels. The point spread function had a full width at half-maximum of 3 arcsec. These images were then used to remove all the identified stars and create a flat image. Around 50 flat images were averaged to produce a master flat, which was then used for flat fielding the images. The flat fielded, bias subtracted images were then used for determining the magnitudes and the fluxes of the target and comparison stars. In some of the exposures, the algorithm could not identify the star and hence the light curve had certain individual bins that had very low counts. All such bins (<2% of the total bins) were manually removed.

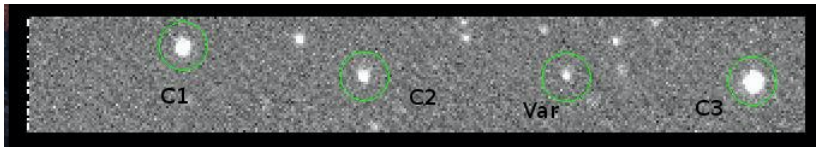

Fig. 3.1 SALT field of view

3.2.2 Timing analysis and results

Light curves

Figure 3.2 shows the light curves for both the nights with a bin size of 7 s. The March 5th light curve shows slow variations around an average rate. The optical intensity varies by about a factor of 2 on the first night and by a factor of 3 on the second night. The March 6th light curve shows many flares of duration between 3 to 15 minutes recurring at shorter timescales during some parts of the light curve. The flaring amplitude is about 1.5 to 2 times above the quiescent levels. These flares are of shorter duration with shorter recurrence timescales as compared to earlier reports (Joss et al., 1978a), which had ∼500 s co-incident X-ray and optical flares, recurring every ∼1000 s. In the spin-down phase of 4U 1626-67, it is known to show no X-ray flares (Chakrabarty et al., 2001; Beri et al., 2014).

Power Density Spectra

The Power Density Spectra (PDS) generated from the two nights are shown in Figure 3.3. The PDS was white noise subtracted and also normalized such that its integral

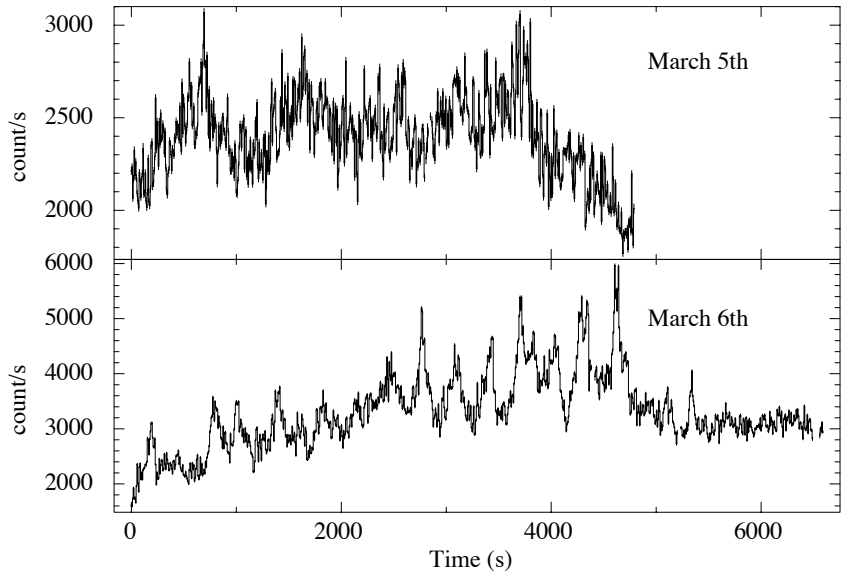

Fig. 3.2 V-band light curves of 4U 1626-67/KZ TrA with a bin size of 7 s shown for March 5th (top, T_{start} MJD 56721.06) and March 6th (bottom, T_{start} MJD 56722.06), 2014. March 6th light curve shows a number of flaring episodes.

gives the squared r.m.s fractional variability. The PDS has a power law shape and shows the pulse period peak and the higher harmonics. The March 5th night data, surprisingly, shows a weak broad QPO-like feature at nearly 48 mHz. This PDS was fit with a power law in the frequency range 2 mHz to 0.2 Hz, excluding the frequency bins near the pulse frequency and the harmonics. The excess in power around 0.048 Hz was fit with a Lorentzian centered at that frequency. The optical QPO has a fractional amplitude of 3.3% (Figure 3.3). Also, a broad feature centered at 3.2 mHz, is observed in the PDS of the March 6th night light curve, which appears to be a reflection of the periodic flares that are present in the light curve.

Period search and folded optical pulse profiles

The optical pulse period was searched for, using trial periods around the known X-ray pulse period of 7.6736 s obtained from the near simultaneous *Swift*-XRT observations (see next section). The FTOOL '*efsearch*' is a time domain epoch folding procedure that is used to determine periodicity accurately in a time-series once an approximate

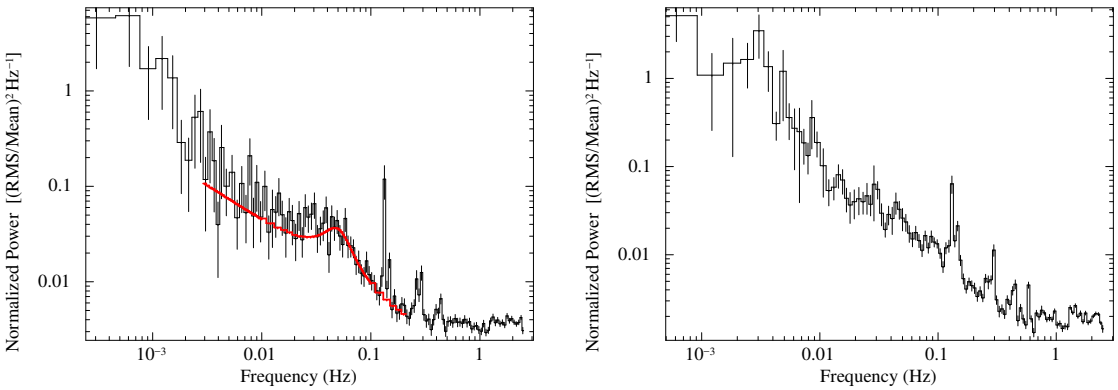

Fig. 3.3 White noise subtracted Fourier power density spectrum of March 5th (left) and 6th (right) night data normalized relative to the mean source power. The broad 48 mHz optical QPO detected in the March 5th SALT PDS is fit with a power law and a Lorentzian and shows a fractional rms amplitude of 3.3%.

period value is known. Each folded time-series is fit with a constant function and the best period is obtained by chi-squared maximization. The SALT time-series were folded with 1000 different periods around a value of 7.67 s with a resolution of 0.1 ms and 32 phase-bins per period. A sharp peak at 7.677 s (130.259 mHz) and a sideband at 7.697 s was obtained on the March 5th. The left panel of Figure 3.4 shows the *efsearch* results for March 5th light curve. The sideband frequency, measured from the SALT light curve is 129.921 mHz giving a frequency down-shift of 0.338 mHz and the corresponding beat period of ∼49.3 minutes as compared to the earlier measured value of 42.2 minutes or a difference of 0.395 mHz (Chakrabarty, 1998). The amplitude of the side-band relative to the main pulsation is ∼30%, compared to 20% measured by Middleditch et al. (1981) and 25% measured by Chakrabarty (1998).

The average pulse profiles folded at the pulse period and sideband period are shown in Figure 3.5. The profile shows a single broad peaked feature. The pulse fraction obtained from the average pulse profile on March 5th night was 5%. An orbital phase resolved analysis was carried out using the March 5th light curve. The light curve was divided into 4 orbital phases corresponding to the beat period obtained on night 1 (0.338 mHz or 49.3 min), and separate pulse profiles were created from each segment by folding with the same pulse period. The four resultant profiles are shown in Figure 3.6. The pulse profile shape clearly varies as a function of orbital phase.

A period search, carried out on the light curve of the second night, produced several peaks, no single one stands out, like that obtained from the data of March

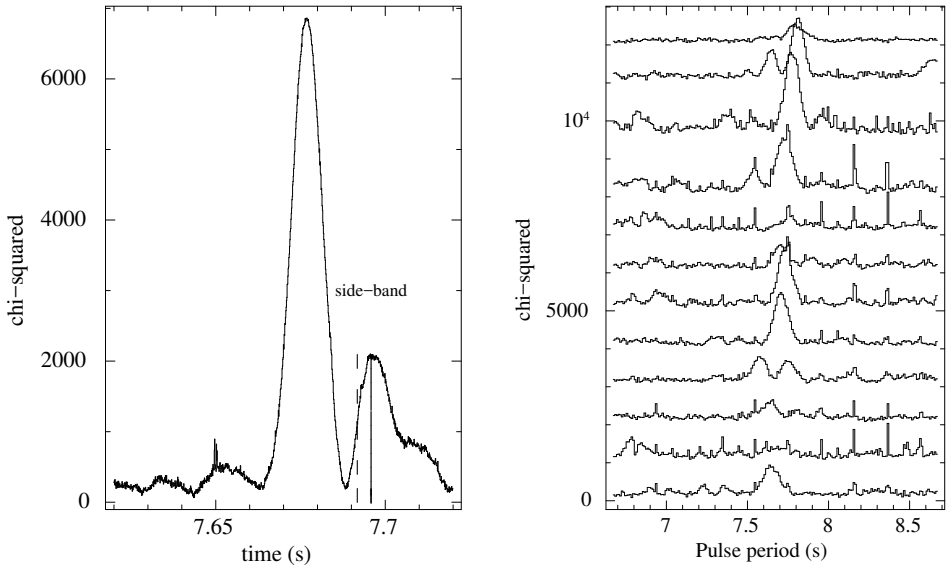

Fig. 3.4 Period search results for March 5th (left) and 6th (right) light curves. A clear side-band peak is seen on March 5th data at 7.697 s. The earlier reported side-band is shown by the dashed line. The March 6th light curve has been divided into smaller segments and epoch folding period searches yield variable pulse periods along the course of the observation.

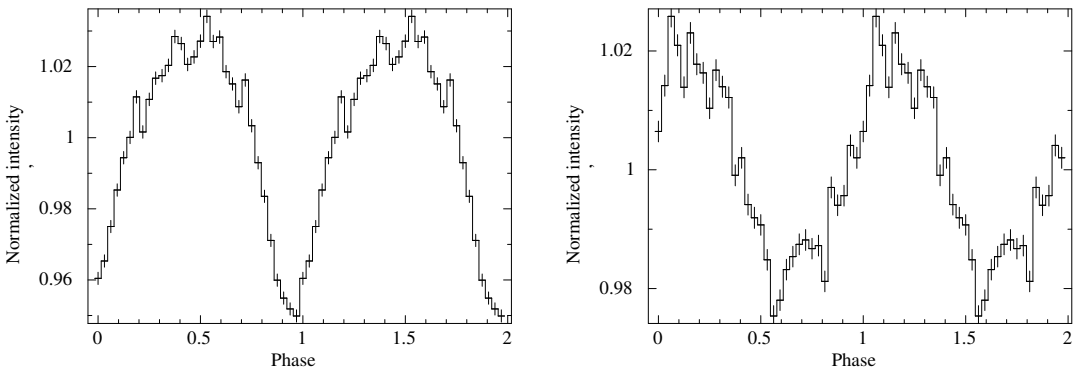

Fig. 3.5 Average pulse profiles for Night 1 folded on the main pulse period 7.677 s (left) and sideband period 7.697 s (right).

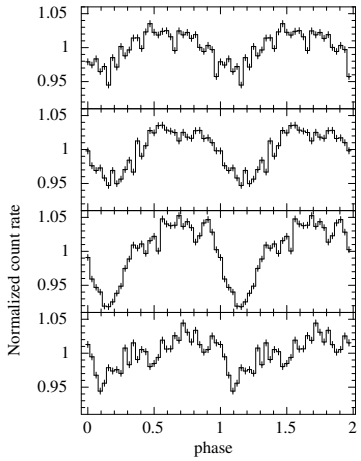

Fig. 3.6 Normalized pulse profiles of March 5th light curve folded at the pulse period shown at 4 different orbital phases considering an orbital period 2958 s.

5th. A search for coherent pulsations was then carried out in small segments of the light curve, in a wider trial period range. The result is shown in Figure 3.4 (right panel). Clear pulsations are detected in at least five segments, but with a pulse period which differ by as much as 0.1 s. The pulse period monitoring of 4U 1626-67 with the Fermi Gamma Ray Burst Monitor (GBM) shows a period change of the order of a few micro-seconds per day in the current spin-up phase, which is much smaller than the period measurement error from the first night's light curve. Assuming that the true spin period of the neutron star on the two nights must be quite similar, pulse profiles from the March 6th light curve were created with the same period.

To study the pulse shape variation as a function of time, the V-band light curves of March 5th and 6th each were folded on 7.677 s pulse period. A total of 20 and 27 pulse profiles were created for the two nights respectively which are shown in Figure 3.7. Each pulse profile, corresponding to a time segment of ∼244 s, was given count rate offset and plotted below the previous profile. The segment-wise pulse profiles of March 5th shows no significant drift. However, the March 6th data shows a phase shift in the pulse profile peak at the rate of 3 pulses per 0.02 days, corresponding to a pulse period difference of about 0.1 s, as one moves along the light curve segments. This is also seen in pulse period of the second night (Figure 3.4, right panel). To eliminate the possibility that the phase drift seen on March 6th night could be due to the overall intensity variation in this light curve, the analysis was repeated after de-trending the light curve with a 4th order polynomial. The pulse peak drifting effects were found to

be same in the de-trended light curve.

Dynamic power spectra

To further probe this drift in the pulse period, a dynamic power spectrum analysis was carried out. Light curve segments of duration 1000 s were created with a moving window of 20 s, for both the observations. The dynamic power spectra are shown in two frequency ranges: around the fundamental (Figure 3.8 and 3.9 top) and first harmonic of the pulse frequency (Figure 3.8 and 3.9, bottom). PDS of the 5th night shows persistent features at the fundamental and the harmonic with lower power at around $2/3^{rd}$ of the observation. This is consistent with a smaller pulse fraction in the pulse profiles at that time. The dynamic power spectrum of the 6th night shows many interesting patterns of decreasing pulse frequency with lower power in the last 20% of the observation and at around $1/5^{th}$ of the observation. It also shows an upward turn in the frequency near the discontinuity. Two frequencies are present simultaneously at about $1/4^{th}$ and $3/4^{th}$ of the observation.

3.2.3 Simulation of the side-band

The peak of the side-band feature seen from the observation on the night of March 5 has an offset of 0.338 mHz which is different from values of the same measured earlier (Middleditch et al., 1981; Chakrabarty, 1998). A simulation was carried out to find the significance of this difference. Gaussian randomized light curves were simulated at the same time bins as the observed data using the main band and side-band pulse profiles as shown in Figure 5.2 (left and right-hand panels) with random phase offset. Period searches were carried out on 10000 simulated light curves. However, the short duration of the observation, covering only about two orbital cycles, proved to be insufficient to constrain the separation between the two components with simulations.

3.2.4 X-ray data analysis and results

Swift-XRT analysis results

A Target of Opportunity X-ray near-simultaneous observation was carried out on 2014 March 5 (See Table 3.1) using Swift-XRT. The XRT aboard the Swift satellite was operated in the Window Timing mode and given an exposure of 4594 s with a time resolution of 0.1 s. The raw data were processed using xrtpipeline task and using

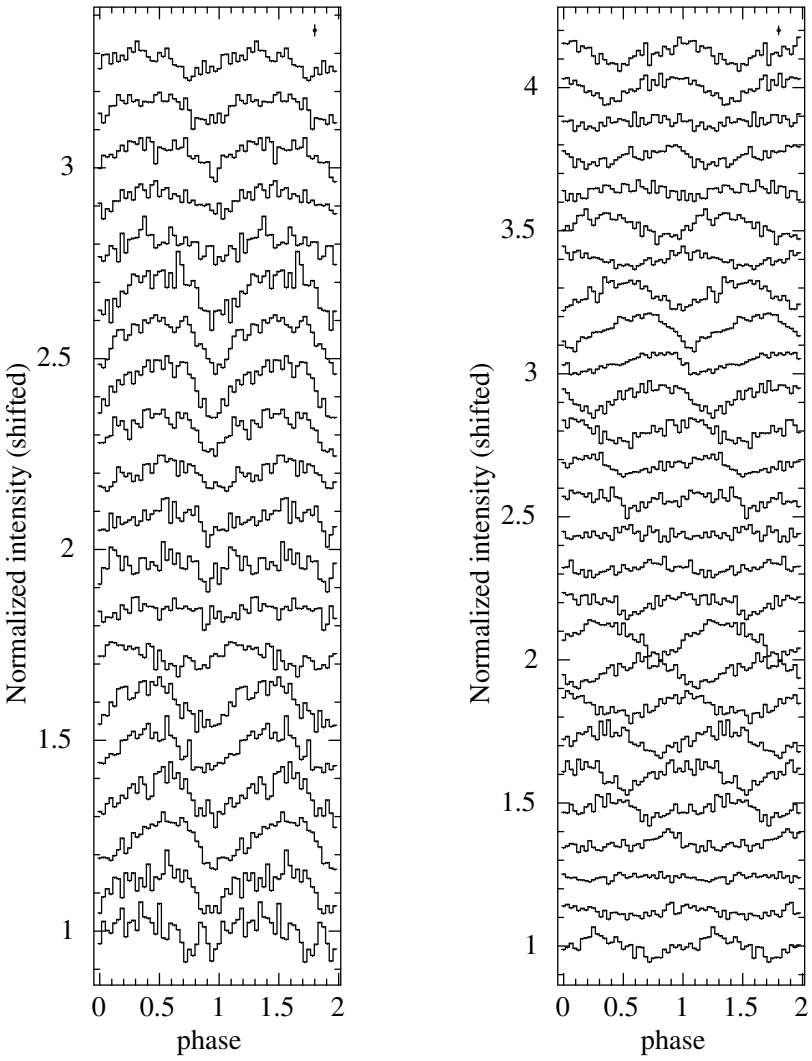

Fig. 3.7 Pulse profile evolution as a function of time for March 5th and 6th nights are shown in the left and right panel, respectively. Each pulse profile corresponds to a time segment of ∼244 s. To estimate the error, each light curve segment has been folded with a pulse period, away from the main pulsation, that showed a very low power in the period search routine. An average standard deviation was then computed for the folded profiles from all the segments and is shown in the top-right corner of the figures.

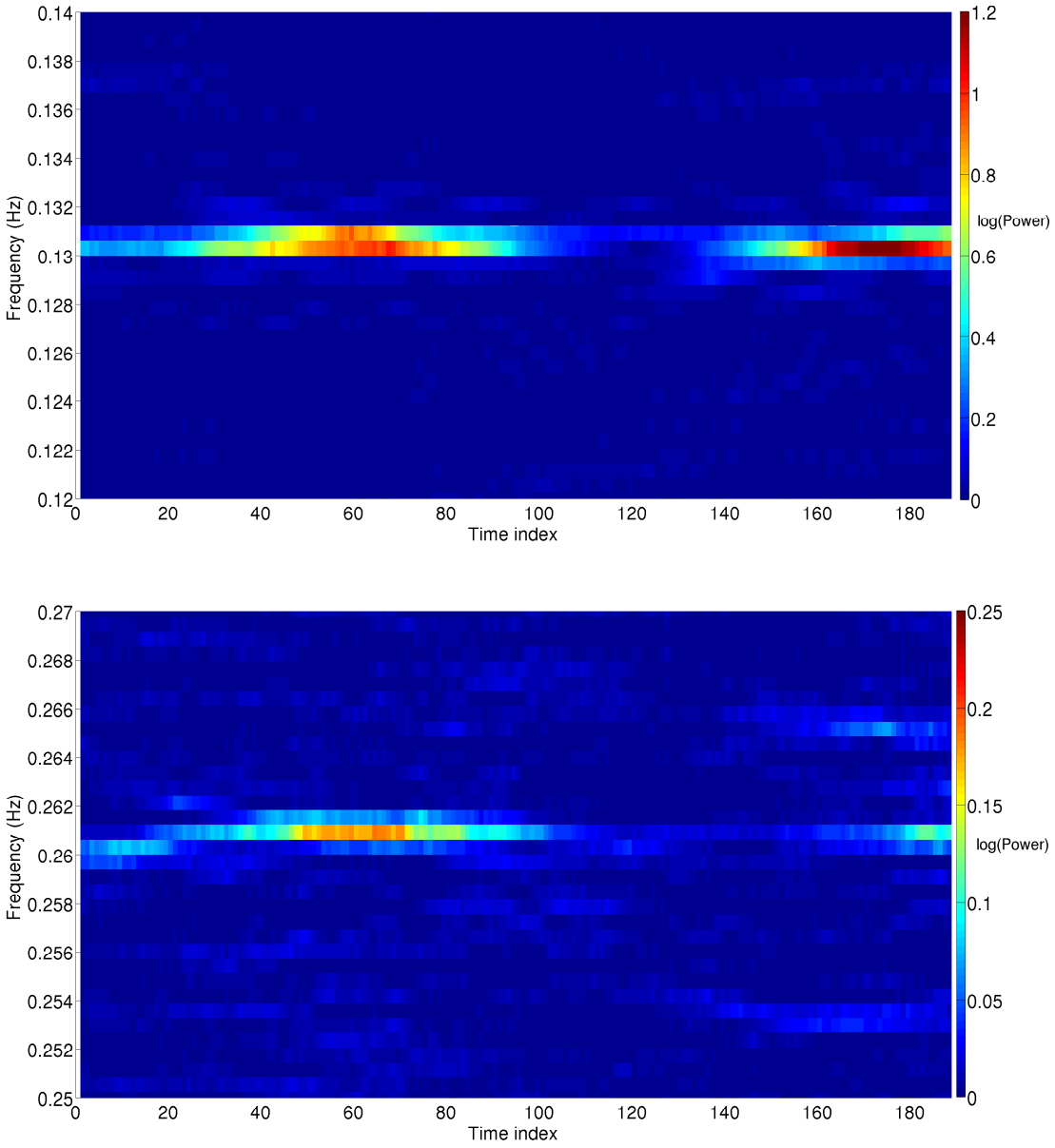

Fig. 3.8 Dynamic power spectra around the fundamental (top) and first harmonic (bottom) of the pulse frequency on March 5th. Each segment corresponds to 1000 s of data and a moving window of 20 s.

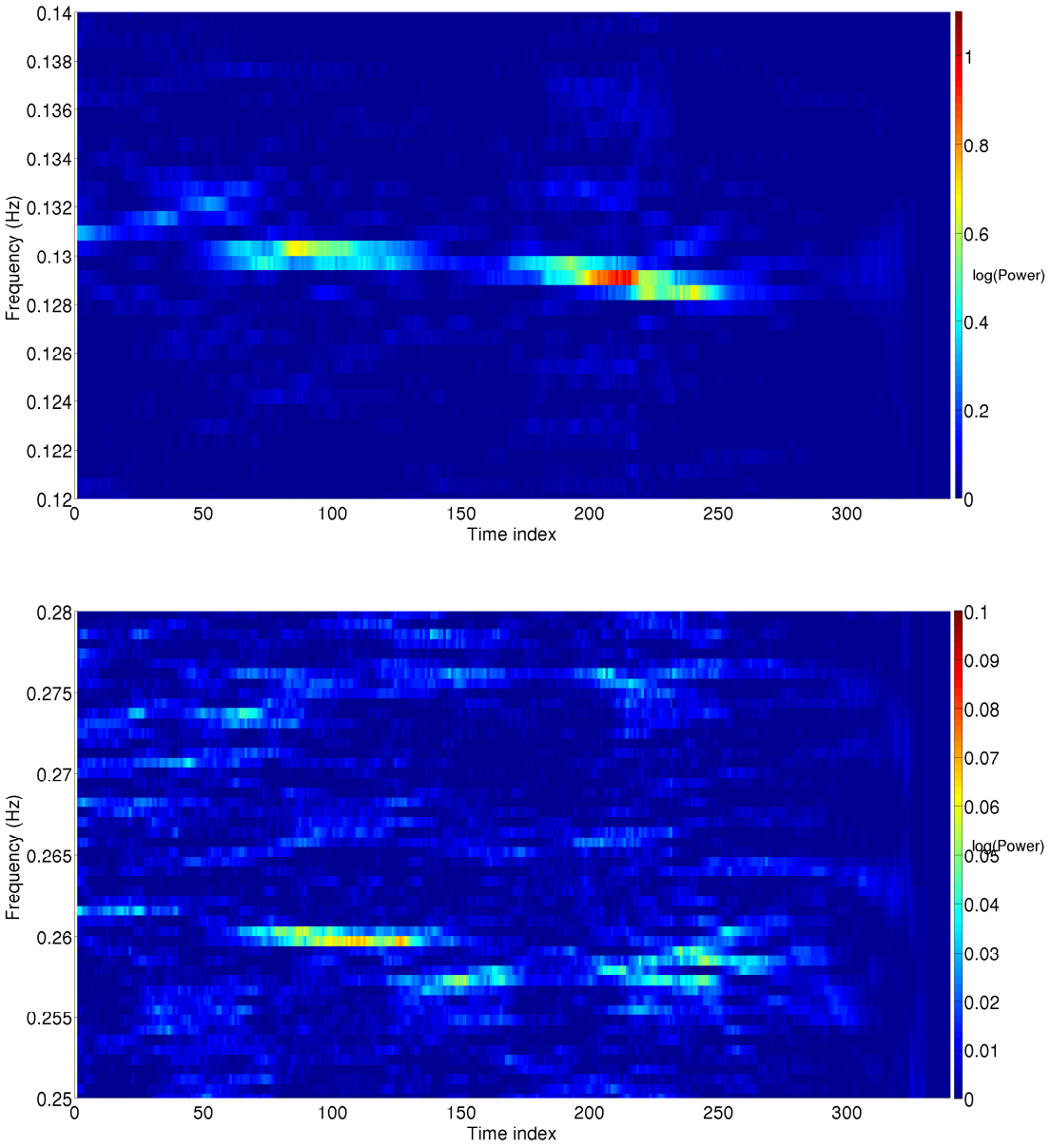

Fig. 3.9 Dynamic power spectra around the fundamental (top) and first harmonic (bottom) of the pulse frequency on March 6th. A clear evolution of the spin period strength and frequency is observed on March 6th.

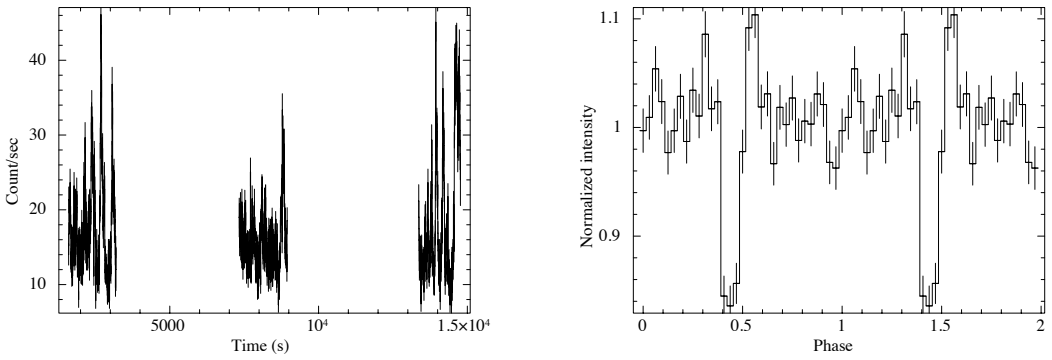

Fig. 3.10 Figure shows 7 s binned *Swift*-XRT light curve (Start time 56721.52 MJD, left) and the pulse profile folded at the best period 7.6736 s (right).

standard screening criteria. The source image and light curve were extracted using xselect in the energy band 0.3 to 10 keV from a circular region centered on the source co-ordinates. The background subtracted Swift light curve with a bin size of 10 s is shown in Figure 3.10 (top panel). The efsearch task was used to determine the pulse period and a sharp peak was obtained at 7.6736 s. The light curve was folded using this pulse period. The characteristic double-horned profile is discernible (Figure 3.10 bottom panel). The Swift observation was carried out to know if the properties of the X-ray source (pulse profile, power density spectrum) were the same as the other X-ray observations in the spin-up phase.

RXTE analysis of pulse profiles in flaring state

The near simultaneous Swift-XRT observation which was carried out on March 5 showed no flares and has limited statistics. So it was not possible to separately investigate intrinsic variations in the X-ray pulse profile using the Swift-XRT light curve. Archival data of the Proportional Counter Array (PCA) on board RXTE were analyzed for this purpose. The standard 1 light curve in the 2-60 keV band was extracted for all the observations after the second torque reversal in 2008. The PCA light curve with a bin size of 7 s for one such Obs-ID 95313-01-01-08 (see Table 3.1) is shown in Figure 3.11. The light curve shows intermittent flares. However, in contrast with the March 6 optical data, period search on the X-ray light curve gives a single sharp peak at the pulse period of 7.67 s. The light curve from small segments was folded at this pulse period and stacked over one another by giving them a finite offset (Figure 3.12). The X-ray profile is dominated by dips, which are locked in phase. They are probably produced by absorption in the accretion stream/column. Flaring portions of the X-ray light

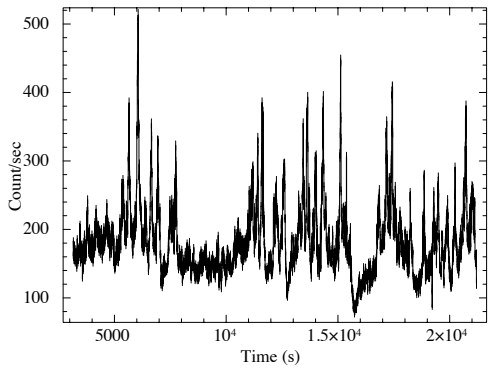

Fig. 3.11 *RXTE*/PCA light curve with a bin size of 7 s corresponding to Obs-ID 95313-01-01-08 showing many flares.

curve seem to change the amplitude of the peaks in the X-ray pulse profiles to some extent, but no phase shift is seen in the X-ray pulse profile. The PDS from two of the data sets from the post second torque-reversal era were analyzed. These observations had large exposure times and were devoid of any flares (Obs-ID 95338-05-01-00 and 95338-05-02-00). The power spectra were fit between the frequency range 2 to 200 mHz with a power law continuum and a Lorentzian at the same QPO frequency as obtained from the current SALT dataset. The upper limit of the rms power of the X-ray QPO was found to be 0.9%.

3.3 SALT observation 2016

3.3.1 Background

4U 1626-67 is a unique high magnetic field LMXB pulsar that shows torque reversals, flares, mHz QPOs etc. This object has also exhibited X-ray side-bands at the frequencies corresponding to n$\times\nu_s$ + ν_{QPO}, where n is an integer, ν_s is the spin frequency of the neutron star and ν_{QPO} is the QPO centroid frequency (Kommers et al., 1998). Some X-ray side-bands have been observed to be symmetric in both frequency and power amplitude. However, some other side-bands are asymmetric in power but not in frequencies; the lower frequency side-bands have enhanced amplitudes compared to their higher frequency counterparts. Side-bands can also occur at frequencies modulated at the orbital period of the binary. Since the different X-ray timing variabilities like the pulsation, flares and QPOs are being consistently observed in the optical due to reprocessing, it becomes intriguing when optical observations reveal side-bands, more

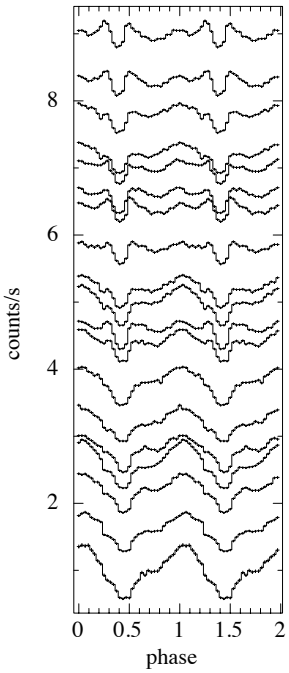

Fig. 3.12 Time evolution of RXTE pulse profiles folded at the 7.676 s pulse period along the flaring light curve. Changes in pulse profile shape is seen but not any phase shift.

so, because the origin of these modulations is still debated. Apart from the down-shifted orbital side-band, two additional side-bands have been reported for this object in the optical (Chakrabarty et al., 2001), whose origin was attributed to superhumps, warps etc. in the accretion disc.

The interesting location of the side-band as well as the presence of the drifting pulse periods detected in the SALT observations of 2014, prompted us to re-visit the source 4U 1626-67 again using SALT.

3.3.2 Observations and data analysis

4U 1626-67 was again observed with the SALT telescope using the SALTICAM instrument operated in the slot mode on 5th June, 2016. SALT, being a fixed elevation telescope, with a 11 meter primary, was operated in a unique configuration to observe the source continuously for ∼5.5 hours on 5th June, 2016. These observations were carried out in the V band. The raw images were extracted using `IRAF`. Along with the target source, three comparison stars were identified in the field of view. Standard

cleaning and image reduction procedures (explained in the previous section) were adopted to obtain the magnitudes and fluxes of the stars using the SEXTRACTOR package.

In order to subtract the effects of the intervening atmospheric variations, we carried out differential photometry between the target star and the three other comparison stars. Figure 3.13 shows the differential light curves as the ratio of the magnitudes of the target star along with each comparison star C1, C2 and C3. No flaring episodes are visible in the light curve. A period search was carried out on the light curve using the ftool '*efsearch*' and the result is shown in Figure 3.14. A strong pulse period signal is observed at 7.672 s along with the orbital side-band peak, which is located at 7.696 s. The frequency separation between the main pulse and this side-band results in the beat period of 42 minutes, confirming the earlier measured orbital period of 42 minutes. We also observe a second side-band at 7.65 s. This peak is at the $\omega_{spin} + \omega_{orbital}$ frequency. The presence of such a frequency could be indicative of a different kind of modulation discussed below. The white-noise subtracted rms normalized power density spectrum is shown in Figure 3.15. It shows the pulse peak and its harmonics, although no QPO at 48 mHz is observed during this SALT observation. In order to study the stability of the pulse period strength and frequency as a function of time, a dynamic power spectrum was constructed using 1000 second patches of the light curve and a 20 s moving window (Figure 3.16). The pulse period is seen to be fairly stable over the entire duration of the observation.

3.4 Discussions

4U 1626-67 is an X-ray pulsar that has been found to consistently display timing signatures in the optical that mirror the X-ray timing features due to reprocessing phenomenon. Results from this work indicate many reprocessing signatures like optical pulsations at the spin frequency of the neutron star, the orbital side band due to reprocessing of the X-ray pulse from the surface of the companion star, optical flares of a few hundred seconds timescales, an optical QPO at 48 mHz and drift in the phase of the reprocessed optical pulses in data from one night. The accretion disc contributes to most of the reprocessing that is observed, with the companion star surface also partly being responsible for reprocessing the main X-ray pulsation.

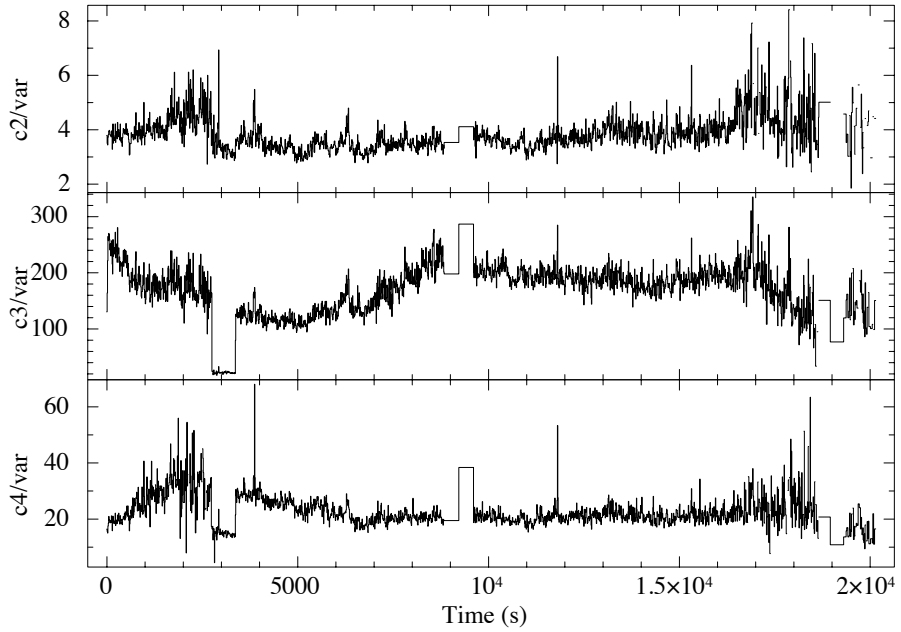

Fig. 3.13 Differential photometric light curves of 4U 1626-67 with three comparison stars C1, C2 and C3 are shown.

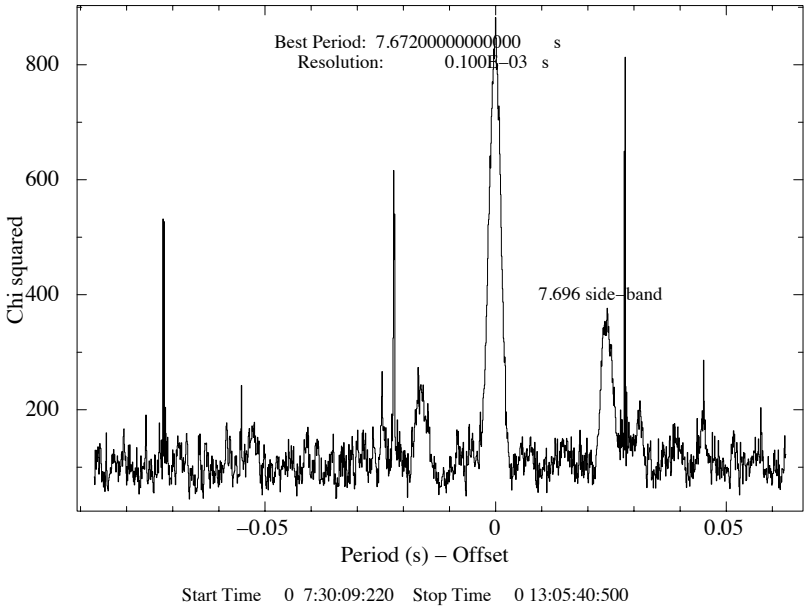

Fig. 3.14 The period search analysis shows a strong signal at the pulse frequency of 7.67 s and two side-bands.

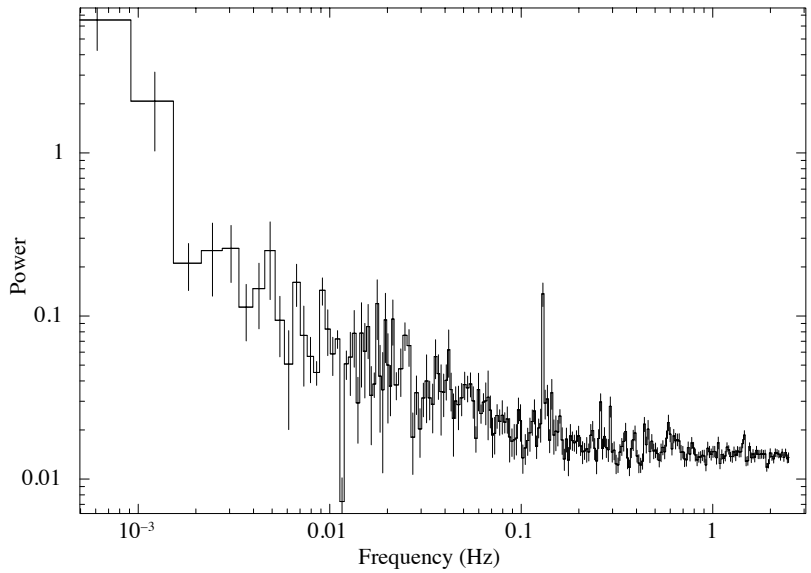

Fig. 3.15 The power spectral density showing the pulse period and its harmonics.

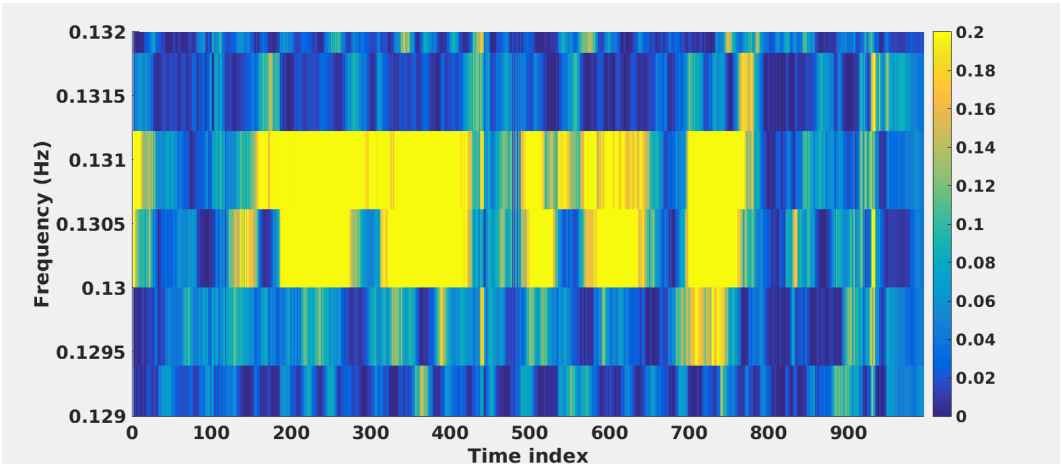

Fig. 3.16 A dynamic power spectrum showing the evolution of the strength of the pulse period as a function of time.

A 48 mHz QPO was detected simultaneously in the X-ray and optical bands in the spin-down phase right after the first torque reversal (Chakrabarty, 1998). Although the first spin-up phase showed a weak QPO at ∼40 mHz in X-rays (Shinoda et al., 1990), it is absent in the X-ray light curves of the current spin-up phase (Beri et al., 2014). Interestingly, current SALT results point towards the presence of the same 48 mHz QPO in the optical.

The presence of the optical 48 mHz QPO at the same X-ray QPO frequency indicates that the X-ray signal is being reprocessed. The 48 mHz QPO from the optical light curve is detected at an rms of 3%, while the non-simultaneous X-ray QPO (obtained from RCTE-PCA observations in the same spin-up era) is seen to have an upper limit of 1% rms at the same frequency. However, detection of the QPO feature in the optical light curve with strengths higher than the X-ray feature could indicate various possibilities. An underlying X-ray QPO that is anisotropic can generate the optical QPO in a reprocessing region which has different visibility of the X-ray QPOs than the observer. An alternative possibility is that there is an X-ray QPO at 48 mHz in the spin-up phase with a variable rms and during the observation on March 5th, the X-ray QPO rms was higher than usual. A third scenario could be that the QPO generation mechanism in the spin-down phase produces a larger rms in the optical band.

X-ray QPOs in high magnetic field pulsars are believed to be produced as a result of inhomogeneities, that arise due the turbulent accretion flow at the magnetosphere-inner disc connection. The quasi-periodic motion of the inhomogeneities at the different accretion disc radii can act as the source of reprocessed optical QPOs. There are several models that explain the X-ray QPOs observed in accretion powered X-ray pulsars. In the Keplerian frequency model (van der Klis et al., 1987), the QPO frequency corresponds to the Keplerian frequency at the Alfvén radius of the magnetosphere and QPO frequency is larger than spin frequency of the neutron star which is not the present case. The beat frequency model (Alpar and Shaham, 1985) suggests that QPO is observed at the beat frequency between the Keplerian frequency at the Alfvén radius of the disc-magnetosphere and the neutron star spin frequency. This would predict the Keplerian frequency to be, $\nu_k = \nu_{spin} + \nu_{QPO} \sim 0.17$ mHz. As shown in Shinoda et al. (1990), this leads to a consistent measure of the magnetic dipole moment. This model however, fails to explain the asymmetric side-band amplitudes. The inner disc hypothesis of QPOs (Keplerian Frequency Model or Beat Frequency Model) can be tested in pulsars that show both the cyclotron absorption line and QPO (James 2013).

However, in two of the persistent pulsars with known cyclotron line energy in which the QPOs have been detected over a range of X-ray luminosity, the QPO frequency is found to have little luminosity dependence contrary to what would be expected if they had an inner disc origin (4U 1626-67: Kaur et al. 2008; Cen X-3: Raichur and Paul 2008).

A number of other X-ray pulsars have shown flares at intervals comparable to those in the optical light curve of the second night which produce mHz QPO features in the PDS. For example, Her X-1 (Boroson et al., 2000), LMC X-4 (Moon and Eikenberry, 2001) and 4U 0115+63 (Soong and Swank, 1989). A magnetically driven warping/precessing model has been alternatively invoked to explain mHz variability in the X-rays and UV/optical for these sources (Shirakawa and Lai, 2002). A 1 mHz optical QPO, without a counterpart X-ray QPO at that frequency, was discovered in 2001 (Chakrabarty et al., 2001) for 4U 1626-67. Since during spin-down the source did not show 1000 s flares in X-rays, the optical features were attributed to a possible warp in the system. This current dataset in the spin-up phase, does show flares and with significant power at a 3.32 mHz in the PDS of the March 6th night data. Optical flares which are reprocessed X-ray flares might be responsible for such a feature. This cannot however, be confirmed, due to the lack of simultaneous X-ray data for the second night of SALT observation. But another possible scenario could be that the 3.32 mHz frequency, like an earlier reported 1 mHz signal (Chakrabarty et al., 2001), might be a geometric modulation effect.

A tantalizing suggestion in this data is of the difference, by about 0.06 mHz, in the sideband frequency from what was observed earlier (Middleditch et al., 1981; Chakrabarty, 1998). If interpreted as a beat between the spin and the orbital frequency, a change of this magnitude is not expected over such a short timescale. This result would need a longer stretch of timing data to confirm, but one can speculate on possible reasons that could contribute to such a change. Optical reprocessing by a structure in the outer accretion disc, e.g. a short-lived warp orbiting with a period of 2958 s, could give rise to the observed sideband, and small changes in the warped structure can then lead to frequency drift of this feature. Warps in the accretion discs of LMXBs may be driven by instabilities discussed by Pringle (1996). While the conditions for excitation are met in limited circumstances (Ogilvie and Dubus, 2001), strong irradiation (or X-ray heating) of the disc in the present system may help drive such behaviour.

The March 6th light curve showed a definite drift of the phase of the optical pulse with time. The reprocessed optical main pulsation could show such a pulse phase shift if the original X-ray pulse suffered a similar phase shift in the first place. From analysis of many *RXTE* observations in the current spin-up phase, there were significant changes observed in the X-ray pulse profile at short timescales in terms of changes in the relative intensities of the two peaks. However, the X-ray pulse profiles obtained with the *RXTE*-PCA light curves including flares do not show pulse phase drift as is seen in the optical light curve of the second night. The SALT observations therefore do not suggest changes in the rotation period of the neutron star or the pulse period of the X-ray emission. The light curve folded with the period of the neutron star pulse period shows the reprocessed optical emission to be shifting in phase, indicating a changing location of the reprocessing region in the accretion disc. However, the timescale for this change is smaller, about 600 seconds, compared to the sideband observed in the first night which is at a five times longer timescale. The SALT observations therefore probably show warps at different radii in the accretion disc for two consecutive nights.

Side-bands in the SALT 2016 observations

4U 1626-67 is one of the three LMXB pulsars that exhibits an optical pulsation at the same pulse period as the X-ray pulsation. The other two sources are GX 1+4 (Jablonski et al., 1997b) and Her X-1 (Middleditch and Nelson, 1976). The optical pulsed emission in these sources is understood to be primarily due to reprocessing of the pulsed X-ray emission. Reprocessed emission can arise from various regions for example, from different axisymmetric and/or non-axisymmetric parts of the accretion disc, from the surface of the companion star facing the neutron star, from the stream-impact point at the outer accretion disc, etc. This implies, that the light curve can be considered as a sum of these various reprocessed components along with a constant background. Assume that a simple optical modulation of the pulsation can be represented by an intensity variation of the form A sinωt, where ω is the angular frequency of rotation of the neutron star. This implies that reprocessing at the different binary locations, could then lead to a number of other periodicities due to the orbital motion of the binary, rotational motion of any of the reprocessing regions, etc. These components need not necessarily be in phase with respect to the primary modulation frequency ω. These periodic Fourier components have been observed in the PDS for a number of CVs as well (Warner, 1986). Fourier components that are close to the spin period of the neutron star can be interpreted as a beat period between the neutron star spin

frequency and some other characteristic frequency in the binary, for example, the orbital frequency at a given radius or a QPO frequency.

Detection of these optical side-bands is extremely intriguing. Not only do they act as tracers for orbital modulation signatures, but if their presence/absence is transitory, i.e they are observed only during certain observational epochs, they can be very useful in understanding the development and evolution of disc structures like warps or blobs that are located at different accretion disc radii. The orbital side-band in 4U 1626-67 at 7.696 s is understood to be a signature of periodic illumination of the secondary star by the X-ray pulsation as the entire binary rotates with frequency $\omega_{orbital}$. Such a modulation can result in an intensity variation with frequency of $\omega_{spin} - \omega_{orbital}$. The second peak in the period search has a frequency of $\omega_{spin} + \omega_{orbital}$. Such a modulation can arise due to several other reasons. It could represent precession of an accretion disc warp or reprocessing in a certain asymmetric feature in the disc. In CVs, pairs of asymmetric side-bands are observed that are modulated at the orbital frequency of the binary (Warner, 1986). Apart from the spin frequency and the orbital side-band frequency, intensity modulations at frequencies like $\omega_{spin} - 2\omega_{orbital}$, $\omega_{spin} + \omega_{orbital}$ can also be expected and have been observed. Obtaining the relative amplitudes and phases of these side-bands can shed light on the dominant reprocessing components which could be the source of this observed modulation frequency. This is particularly important in a system like 4U 1626-67, where the system orbital parameters like the binary inclination and the companion mass are not well constrained.

Longer, and simultaneous X-ray and UV/optical timing study would yield a more comprehensive understanding of the size, extent and location of the reprocessing sites within the binary and give more insight into the effects of torque reversal on the inner disc-magnetosphere geometry.

3.5 Summary and Conclusions

The ultracompact LMXB X-ray pulsar 4U 1626-67 has been studied in the optical during its spin up phase using SALT. A number of reprocessing timing signatures have been detected from the two SALT observations, like the 48 mHz optical QPO, an optical pulsation at the pulsar's spin period ∼7.67 s (as illustrated in Figure 3.18) as well as optical flares. Drifting optical pulses, slightly shifted optical side-band

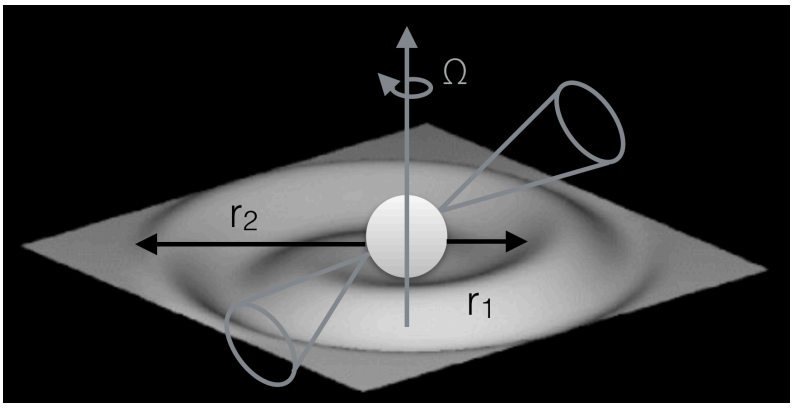

Fig. 3.17 A cartoon illustrating the warps at two different accretion disc radii r_1 and r_2. The NS spin frequency is indicated as Ω. Image adapted from Maloney and Begelman (1997) and modified for clarity.

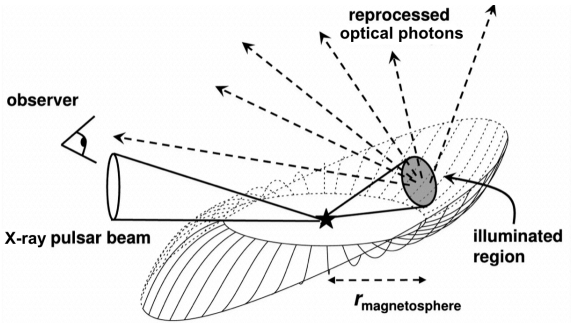

Fig. 3.18 Schematic of disc reprocessing in X-ray pulsars, adapted from Hickox and Vrtilek (2005) and modified for clarity. The X-ray beam sweeps around and illuminates the accretion disc, which re-radiates a soft X-ray and optical component.

frequency and the presence of mHz QPOs are indicative of inner disc-magnetospheric interactions leading to instabilities like accretion disc warps (as illustrated in Figure 3.17), etc. An second optical observation has revealed a side-band at 7.65 s in this system. For a system as unique as 4U 1626-67, such reprocessing studies can help serve as an additional diagnostic tool to understand accretion torque effects and also evolutionary scenarios of accretion powered LMXB pulsars.

Chapter 4

Reprocessing in EXO 0748-676

A part of this chapter is adapted from the paper 'X-ray and Optical orbital modulation in EXO 0748-676 using XMM-Newton' by Raman and Paul (2017) published in New Astronomy, 54, 122.

4.1 Source background

EXO 0748-676 is a prototypical eclipsing LMXB system. Soon after its discovery using EXOSAT in 1985 (Parmar et al., 1986), its optical counterpart UY Vol was identified (Wade et al., 1985; Pedersen et al., 1985). It was found to be a high inclination ($\sim$ 75 - 82°) system on account of its display of periodic eclipses every 3.82 hours (Parmar et al., 1985b; Crampton et al., 1986; Parmar et al., 1986). The primary star in the binary was identified as a neutron star because of the presence of thermonuclear X-ray bursts in the X-ray light curves (Gottwald et al., 1986; Parmar et al., 1986). Variabilities in the form of many high and low frequency signals have been detected in the power density spectra for this source, including a Quasi Periodic Oscillation (QPO) at 695 Hz (Homan and van der Klis, 2000). A 552 Hz Burst Oscillations feature, detected by Galloway et al. (2010), is likely to be the spin period of the neutron star in EXO 0748-676. Mass of the companion has been estimated to be in the range of 0.16 to 0.42 $M_\odot$ with the upper limit corresponding to an M2V spectral type star (Hynes and Jones, 2009). Using detailed studies of helium-dominated photospheric expansion bursts, Galloway et al. 2008 derived a source distance of 7.1 $\pm$ 1.2 kpc, which is higher than the distance indicated by X-ray burst studies by Wolff et al. 2005 ($\sim$ 5kpc), that assumed a hydrogen-dominated atmosphere.

In addition to eclipses and thermonuclear X-ray bursts, EXO 0748-676 is known to exhibit pre-eclipse intensity dips in almost all orbital cycles. These dips are commonly understood to be due to obscuration of the central X-ray source by structures in the outer disc, whose azimuthal distribution is variable (Parmar et al., 1986). The source also exhibits a lot of intensity modulation at different orbital phases in the X-rays. Soon after its discovery, it was noted that EXO 0748-676 displayed two different X-ray intensity states (Parmar et al., 1986; Gottwald et al., 1986). Recent studies by Ponti et al. (2014), showed that the X-ray bright 'high' state displayed less intense dipping phenomenon compared to the X-ray faint 'low' state.

The optical counterpart of EXO 0748-676, UY Vol, also exhibits significant orbital modulation in the UV/optical (Crampton et al., 1986; Parmar et al., 1986; van Paradijs et al., 1988). Since most of the optical emission from this system originates from the accretion disc (van Paradijs et al., 1988), it shows optical eclipses simultaneous with the X-ray eclipses; the former is broad and shallow as against the narrow and sharp X-ray eclipses (Crampton et al., 1986; van Paradijs et al., 1988). The optical light curves also exhibit intensity dips at various orbital phases.

A number of earlier studies were performed on simultaneous X-ray and optical data to study the co-variability in LMXBs. Some sources showed X-ray and optical correlation during quiescence (4U 1735-44: Corbet et al. 1989, V404 Cyg: Hynes et al. 2004); some showed no correlation during quiescence (Cen X-3: Cackett et al. 2013); some showed correlation during highest emission (4U 1556-605: Motch et al. 1989a); some showed anti-correlated emission (4U 0614+09: Machin et al. 1990); some sources even showed bimodal behavior i.e., correlation as well as anti-correlation (Sco X-1: Ilovaisky et al. 1980). The lack of a consistent relation between X-ray and optical variations in LMXBs has been associated with changes in the extent and visibility of the reprocessing structures that produce most of the optical variability.

The X-ray and optical emission for EXO 0748-676 was initially seen on an average to be correlated on short timescales (Motch et al., 1989b). Co-variability studies by Thomas et al. (1993) did not yield any X-ray to optical correlations, that were previously observed for this source. Southwell et al. (1996) also confirmed this change in the nature of co-variability. The lack of X-ray and optical co-variability was associated with the geometric masking of the reprocessed emission. Understanding how the system geometry alters the X-ray and reprocessed optical signal requires correlation

studies, which we have carried out using very long, simultaneous X-ray and optical data, obtained from XMM-Newton.

Since the time of its discovery in 1985, this quasi-persistent binary, EXO 0748-676, has been moderately bright and has displayed a lot of short term variability. For a span 24 years, its persistent X-ray luminosity remained at $\sim 10^{36-37}$ ergs/s (Degenaar et al., 2011), after which, it went into quiescence in 2008 (Hynes and Jones, 2009). In this section, the non-burst co-variability of the X-rays and optical emission is probed using XMM-Newton observations. The analysis has been particularly carried out using observations when the spectral state of the source was hard. The X-ray and optical light curves, orbit-to-orbit modulations and the intensity state dependent dipping behavior of EXO 0748-676 are explored as part of this work.

4.2 Orbital modulation in EXO 0748-676

4.2.1 Observations

EXO 0748-676 was observed for nearly 600 kilo-seconds using XMM-Newton, spanning 7 observations between September-November, 2003. Details regarding the 7 Obs-IDs are shown in Table 4.1. X-ray data, obtained from the European Photon Imaging Camera (EPIC), was collected using the PN CCD detector (0.1-10 keV) in the small window mode. Optical data was collected from the Optical Monitor (OM, Mason et al. 2001). The OM was operated in timing mode using the white band (170 - 650 nm). The EPIC-PN and OM are co-aligned and together offer a multi-wavelength coverage to the target in the X-ray and UV/optical bands, enabling detailed reprocessing studies.

The EPIC-PN data were reduced using the `SAS` version 12.0.1 software, using the latest calibration files. The X-ray light curves were extracted in the soft (0.3-5 keV) and hard (5-10 keV) bands from a 40" radius centered on the position of EXO 0748-676 with 1 s binning. The optical light curve was extracted from a region of 6" around the source using the *omichain* task which processes the data with the latest calibration files, and subsequently performs source detection and aperture photometry.

Table 4.1 EXO 0748-676 was observed using XMM-Newton in 2003. This table details the Obs-IDs, date of observation, number of thermonuclear X-ray bursts, number or reprocessed optical bursts, number of complete orbital segments and non-burst r.m.s variability for the soft X-rays, hard X-rays and optical.

Obs-ID	Date (dd/mm/yyyy)	Start Time UT (hh:mm)	t_{exp}	No. of X-ray bursts	No. of Optical bursts	No. of full orbits	Soft X-ray var(%)	Opt. var.(%) var.(%)	Hard X-ray var.(%)
0160760101	19/09/2003	13:37	24.6	10	8	6	52.19	13.93	22.68
0160760201	21/09/2003	13:38	25.1	14	13	6	65.25	16.78	25.19
0160760301	23/09/2003	10:42	30.0	14	11	7	50.20	15.38	22.55
0160760401	25/09/2003	17:29	20.4	9	8	5	65.79	17.17	23.16
0160760601	21/10/2003	10:02	15.2	8	6	3	55.82	17.07	22.87
0160760801	25/10/2003	19:19	17.3	9	6	3	73.30	16.11	23.32
01607601301	12/11/2003	08:24	25.2	12	10	6	65.27	19.54	24.97

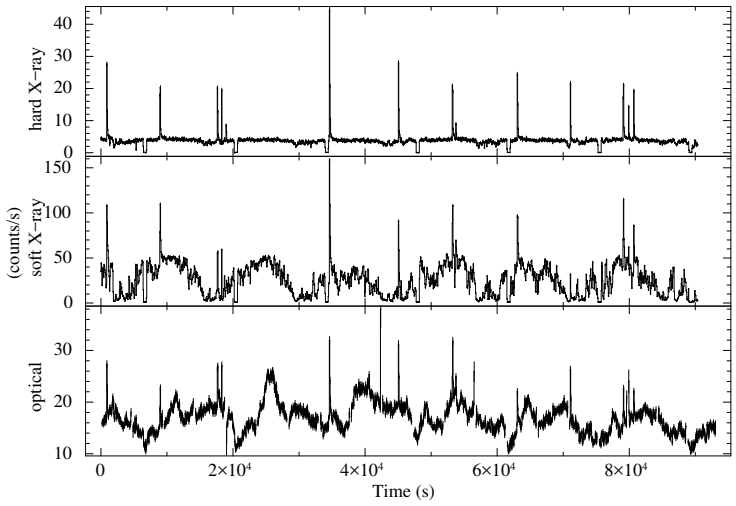

Fig. 4.1 Simultaneous hard X-ray (5-10 keV), soft X-ray (0.3-5.0 keV), and optical light curves with 60 s binning for the Obs-ID 0160760201. The light curves show simultaneous thermonuclear bursts in all the three bands as well as significant non-burst intensity modulation in the soft X-ray and optical bands.

4.2.2 Data analysis and results

X-ray and optical light curves

Figure 4.1 shows the simultaneous soft X-ray, hard X-ray and optical light curves from the Obs-ID 0160760201. All the light curves exhibit thermonuclear bursts, eclipses and intensity dips in the X-rays as well as optical. To study the non-burst orbital modulations in the X-ray as well as optical, thermonuclear burst time intervals were excluded from the X-ray and optical light curves by generating a time window file using the task *xronwin*. The optical burst time windows, in some cases, contained a little more than just the X-ray burst duration to account for the delayed optical response and also the slow, extended decay tails. Depending on the duration of each

burst, windows spanned a time range of approximately 40 to 100 s.

Simultaneous non-burst hard X-ray, soft X-ray and optical light curves are shown in Figure 4.2 for all the 7 observations with a bin size of 60 s. A significant amount of variability is seen in the soft X-ray band compared to the hard X-ray for all Obs-IDs. The most prominent variability observed all the 7 light curves is the orbital modulation. The pattern of orbital modulation appears to vary significantly during the observations, which is discussed below. The optical count rate varies between 10-25 counts/s and soft X-ray count rates are nearly 2-3 times the optical rates for almost all the Obs-IDs. The percentage r.m.s variability with respect to the average values of the 60 s binned light curves in these bands for all the 7 Obs-IDs are shown in Table 4.1. A number of differences in the intensity variation patterns like heavy to moderate dipping behavior, frequent short timescale fluctuations, smooth orbital variability etc. are seen in all the three bands on different observation epochs.

Orbit-to-orbit modulation

To further probe sub-orbital timescale modulation and its evolution in consecutive orbits, the light curves were sliced into several orbits using the X-ray orbital ephemeris provided in Wolff et al. (2009). Soft X-ray and optical light curves from different binary orbital cycles for all the seven Obs-IDs are overlaid in Figure 4.3 .

The Obs-ID 0160760101 displays an erratic X-ray behavior with many soft X-ray dips at different orbital phases. In four of the seven observations (Obs-IDs 0160760201, 0160760401, 0160760801 and 0160761301), pre-eclipse dips are seen in soft X-rays in the orbital phase range of 0.6-0.9. In some observations dips are observed near phase 0.2 (Obs-ID 0160760601), 0.15 (Obs-ID 0160760401) and 0.45 (Obs-ID 0160761301). Other than the dips, light curves exhibit large orbit-to-orbit intensity variations often by a factor of a few; for example at phase $\sim$ 0.2 in Obs-IDs 0160760201 and 0160760401 and at all phases in Obs-ID 0160760101. In Obs-ID 0160760601 dips are observed in phase range 0.6-0.9 but with a large difference in the dip phases from orbit to orbit. The dip duty cycle in some orbital cycles, or the fraction of the orbital phase during which the soft X-ray dips are observed, is found to be as high as 50%.

Optical light curves show dips and also peaking signatures at different orbital phases. Obs-IDs 0160760201, 0160760301, 0160760401 and 0160760601 show peaking behavior

at phases 0.1 and 0.4 with moderate dips around phase 0.2 in some of the orbital cycles. A single orbit each in Obs-IDs 0160760201 and 0160760601 peaks at phase 0.2 unlike the rest of the orbital cycles within these observations. Obs-IDs 0160760101 and 0160760301 exhibit a single peak around 0.25, whereas Obs-IDs 0160760801 and 0160761301 exhibit a peak near phase 0.3. According to the variable dipping seen in their orbital profiles, the soft X-ray and corresponding optical variations are broadly classified into five classes (see Figure 4.4). This classification is based on the observed soft X-ray light curves from all the 7 Obs-IDs.

Cross-correlation analysis

Three timescales of variability are defined to assess the correlation between soft, hard X-rays and optical emission. Since reprocessing takes place at extremely short timescales, contribution of this process is insignificant compared to the orbital timescales. Probing such short timescales is not considered in this work. In EXO 0748-676, the size of the accretion disc and the binary separation is $\sim$3 lt-sec (Hynes et al., 2006). Other than the thermonuclear bursts, there is not much short timescale (of the order of a few seconds) X-ray variability. However, the bursts have been removed from the current analysis and therefore, reprocessing at these timescales, is not investigated as part of this work.

To probe long term variability at timescales longer than the ones mentioned above, each orbital segment from the soft and hard X-ray light curve, measured from eclipse to eclipse, was cross-correlated mutually as well as with the simultaneous optical orbital light curve segment with a bin time of 60 s. Data gaps, thermonuclear X-ray bursts, reprocessed optical bursts and the eclipses were not included in the cross correlation analysis.

The XRONOS tool *'crosscor'* was used to obtain the time delay between the various light curve segments in the three bands. This tool adopts the FFT algorithm. The cross correlation profiles have been classified broadly into five classes on the basis of their delays and profile shapes. They do not correspond to the variable dipping classification of the soft X-ray light curves, discussed in the previous section. The CCF profiles (Figure 4.5, left) are computed for sample light curves, one, from each of the five classes, and are shown along with the corresponding orbital light curve segment for the hard X-ray, soft X-ray and optical (Figure 4.5, right). The soft X-ray to optical

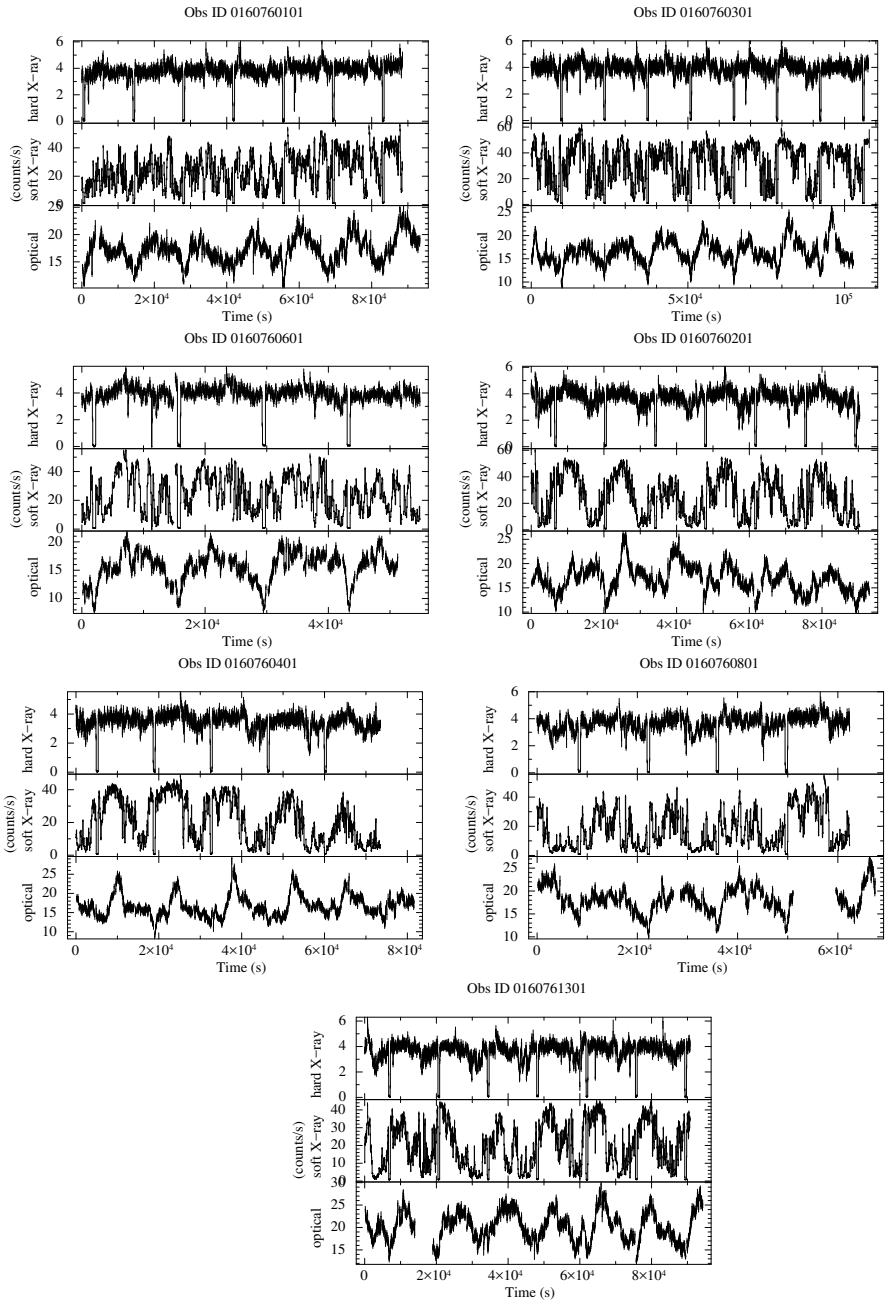

Fig. 4.2 Simultaneous hard X-ray (5-10 keV), soft X-ray (0.3-5.0 keV), and optical light curves for all the Obs-IDs are shown with a filter applied to remove the thermonuclear burst sections. The non-burst X-ray and optical light curves display significant intensity modulation during all the observations.

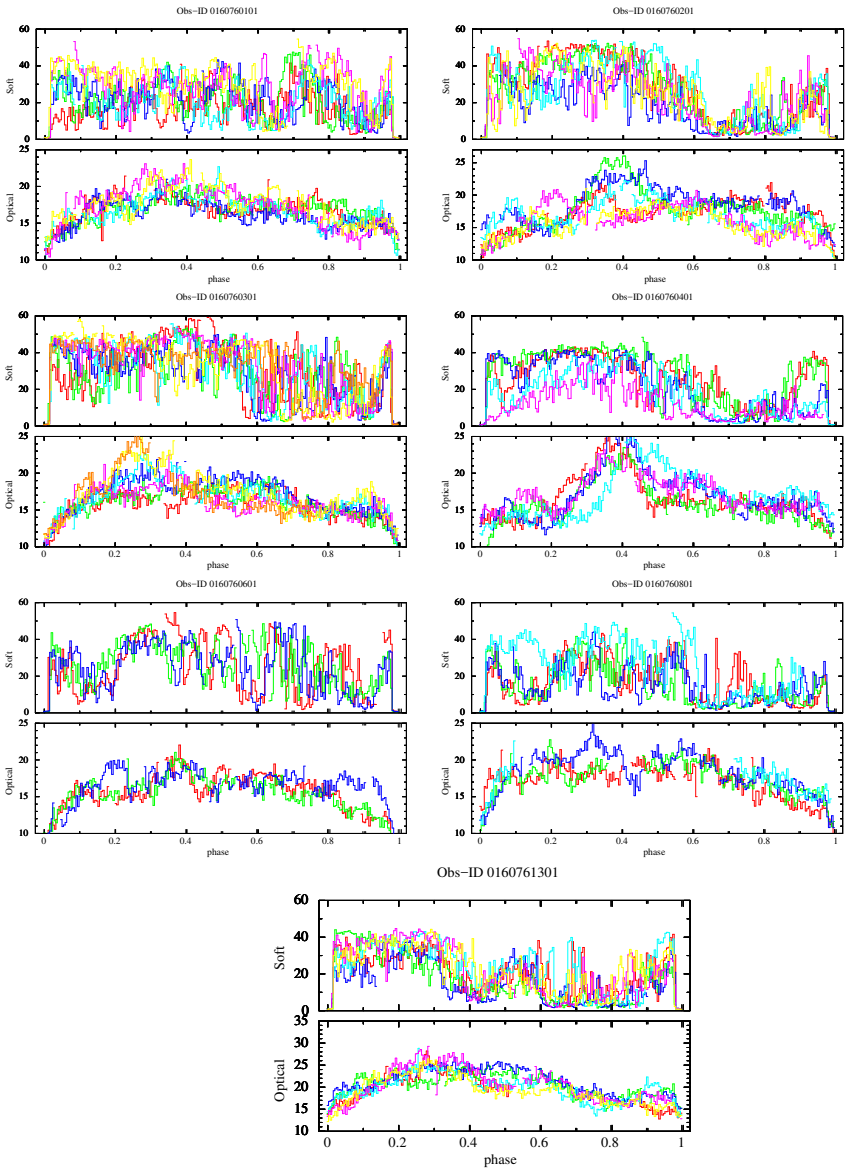

Fig. 4.3 Orbit to orbit modulations seen in soft X-rays simultaneously with the optical for all the Obs-IDs. Each binary orbit is represented by a different color. The orbital light curve intensity is seen to vary enormously between successive binary orbits both in the soft X-rays and optical.

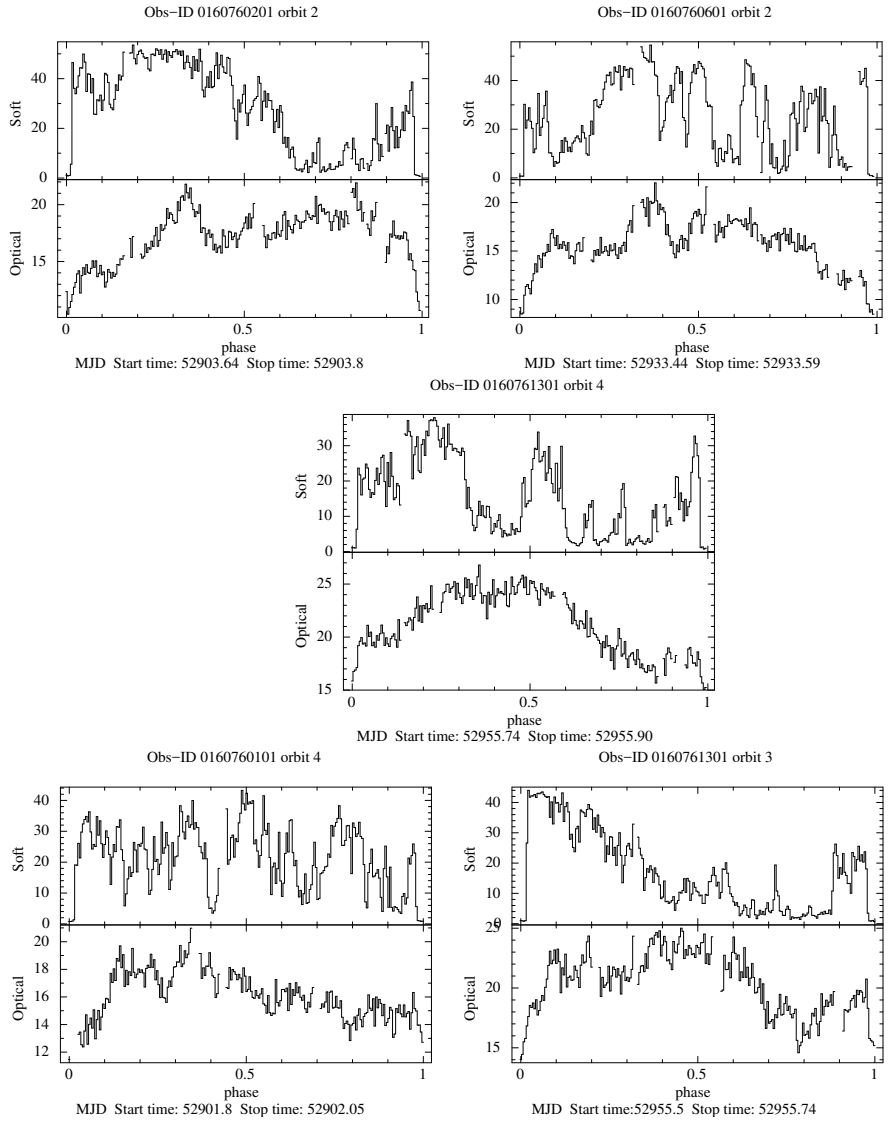

Fig. 4.4 Soft X-ray and corresponding optical variations seen in five broad classes of orbital profiles. 1) A broad pre-eclipse X-ray absorption between phases 0.6-0.9 (top-left panel). 2) A broad absorption feature around phase 0.2 (top-right panel). 3) A broad absorption feature around phase 0.4 (middle panel). 4) Multiple narrow less intense dips at different orbital phases (bottom-left panel). 5) Intense absorption during significant portion of the orbit (bottom-right panel).

Table 4.2 A summary of the cross-correlation analysis carried out between the soft, hard X-rays and the optical light curves from all the 7 Obs-IDs.

Class	Soft X-ray to Optical			Soft X-ray to Hard X-ray		
	delay (s)	FFT Coeff	Pearson's r coeff (p-val)	delay (s)	FFT Coeff	Pearson's r coeff (p-val)
I	660	0.65	0.57	0.0	0.75	0.75
II	1920	0.60	0.38	0.0	0.73	0.66
III	0	0.43	0.43	0.0	0.73	0.73
IV	1260	0.42	0.39	0.0	0.54	0.54
V	1380	0.17	0.07	0.0	0.67	0.66

CCFs resemble the hard X-ray to optical CCFs in almost all the cases. with a positive delay (600-1500 s) indicating that the optical emission lags behind the soft and hard X-ray emission. The soft to hard X-rays CCF shows a sharp peak at near zero delays with a cross-correlation coefficient of ∼0.7. To cross-check the correlation study, a Pearson's test was carried out, the results of which, are summarized in Table 4.2. The first four classes of CCF profiles show weak soft X-ray to optical correlation and strong soft X-ray to hard X-ray correlation with an average cross correlation coefficient of ∼0.5 and an average Pearson's test r value of ∼0.4 and ∼0.66, respectively. The fifth class of CCF profiles show no X-ray to optical correlation. Results indicate that here is little or no correlation between the optical and X-rays at short timescales, and the repeating patterns of the CCF are independently related to the orbital period (a few 1000s of seconds).

Spectral analysis

A representative spectral study was carried out to characterize the nature of the absorber responsible for producing X-ray dips. Intensity resolved spectra were extracted for the second orbital cycle from the Obs-ID 0160761301 (Figure 4.6). Díaz Trigo et al. (2006) reported a detailed intensity resolved spectral analysis for this observation. The EPIC-PN spectra were extracted from a region of 40" centered on the source, in the 0.5-10 keV energy band. Segments from the light curve with a count rate of less than 20 counts/s in the 0.5-10 keV band were identified as dipping. The remaining nearly-steady emission segment was considered as persistent emission. The responses were generated using the `SAS` task 'arfgen' and spectral fitting was performed using XSPEC (Arnaud, 1996) version 12.8.1.

The persistent and dip spectra were simultaneously fit with a power-law model along with neutral hydrogen absorber and a partial covering ionized absorber (*zxipcf* in XSPEC). As similarly considered by Díaz Trigo et al. (2006), the nH parameter was

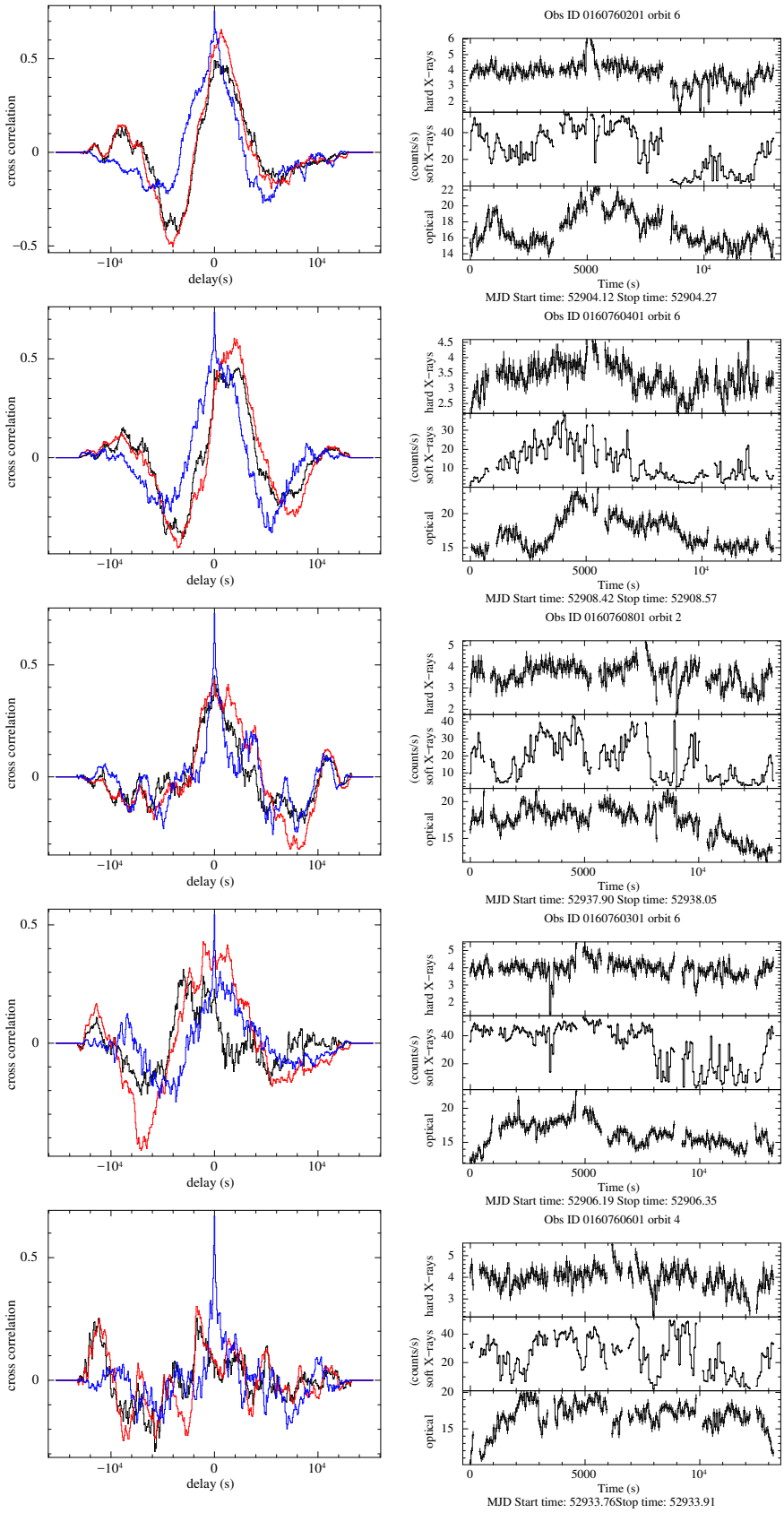

Fig. 4.5 Five different classes of cross correlation analysis patterns between the soft X-ray and optical (red), the hard X-ray and optical (black) and the soft and hard X-ray (blue) have been identified and are shown in the left segment along with the corresponding light curve segments on the right.

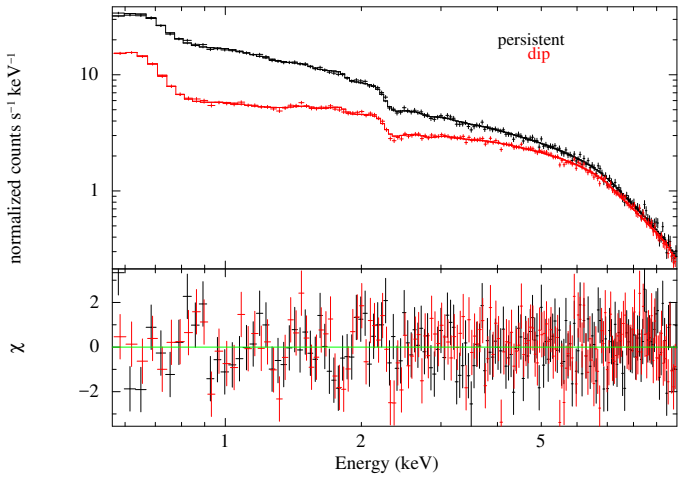

Fig. 4.6 Simultaneous 0.5 - 10 keV spectra for the second orbital cycle of Obs-ID 0160761301 are shown for the persistent and dipping epochs.

Parameter	model	Persistent		Dip
nH (x$10^{22} cm^{-2}$)	*phabs*		0.11 (frozen)	
nH	*zxipcf*	$4.33^{+0.43}_{-0.97}$		$4.53^{+0.45}_{-0.57}$
log(ξ)	*zxipcf*	1.39±0.2		$1.09^{+0.14}_{-0.29}$
cov. f	*zxipcf*	$0.55^{+0.03}_{-0.07}$		0.78±0.02
α	*power law*	$1.52^{+0.04}_{-0.09}$		1.38±0.05
E (keV)	*gaus*		0.569 (frozen)	
EW (eV)	*gaus*	437.2±0.001		666.9±0.0002
E (keV)	*gaus*		0.915 (frozen)	
EW (eV)	*gaus*	70.5±0.0005		49.6±0.0002
Reduced χ^2		1.22 for 319 d.o.f		

Table 4.3 Best fit spectral parameters for the second orbital cycle of the Obs-ID 0160761301.

fixed it to 0.11 × 10^{22} cm^{-2}, in order to prevent it from taking unreasonably low values. Residuals at 0.569 keV and 0.915 keV were observed, which were modelled using two gaussians. A spectral model consisting of *phabs*zxipcf*po+phabs*(gaus+gaus)* model in XSPEC, resulted in a reduced χ^2 of 1.22 with 319 dof. Table 4.3 details the best fit parameters for the intensity resolved spectra. Similar to what is observed in a few other high inclination dippers reported by Díaz Trigo et al. (2006), an increase in the covering fraction of the ionized absorber and a decrease in the ionization parameter is observed, while moving from persistent emission to dipping.

4.3 Simulations

4.3.1 Burst studies in EXO 0748-676

Background

Type 1 thermonuclear X-ray bursts are observed when the fuel accumulated on the neutron star surface burns due to unstable thermonuclear burning. The time interval between successive bursts is the time required to re-accumulate the fuel and attain the correct pressure and density conditions, which go on to trigger the next burst. Using long stretches of XMM-Newton observations (nearly 158 hours) of EXO 0748-676, Boirin et al. (2007) detected 76 type-1 X-ray bursts, some single, some as doublets and some even as triplets. In these very observations, the optical monitor (OM) aboard XMM-Newton recorded simultaneous optical data. This provided an excellent means to study X-ray and optical correlations. Detailed studies of the X-ray and optical bursts were carried out by Paul et al. (2012). They detected 63 simultaneous optical bursts and characterized the rise, decay time and also the reprocessing fraction for the optical bursts. The observed delays between the X-ray and optical bursts were found to be of the order of a few seconds. Paul et al. (2012) fit all the burst profiles with a model consisting of a constant component, a burst with a linear rise and an exponential decay. The X-ray and optical counts of the bursts were then calculated by subtracting the pre-burst component from the total photon counts during the bursts. The bursts show an average X-ray to optical conversion factor (ratio of the optical counts to the X-ray counts for each of the burst) of 0.15 (Paul et al., 2012).

As an extension to the work by Paul et al. (2012), the following exercise was carried out in order to characterize the optically reprocessed bursts further. The X-ray and optical light curves were extracted, after which a cross correlation analysis was performed. The resultant optical bursts were modelled using the Optical Transfer Function (OTF). A detailed description of the procedure is given in the following subsections.

Observation, data analysis and results

To conduct a burst reprocessing study, the 7 XMM-Newton observations, described in section 4.1.2., were used, details of which are specified in Table 4.1. The EPIC-PN CCD and the Optical Monitor provided simultaneous coverage during the entire duration

of observations. Details of data reduction are specified in section 4.1.2. From the light curves generated using the 7 long XMM-Newton observations, 76 thermonuclear X-ray bursts and 63 simultaneous optical bursts were identified. The X-ray and optical bursts exhibit the Fast Rise Exponential Decay (FRED) profile, characteristic of a thermonuclear burst. There were gaps in the optical data during 13 of the X-ray bursts, because of which they were not recorded in the optical observations.

1. Cross correlation analysis

In order to estimate the delays between the onset of each optical burst with respect to the primary X-ray burst, all the 63 X-ray burst profiles were cross-correlated with their respective optical bursts. The cross correlation analysis was carried out between the 1 s binned X-ray and optical burst segments. The CCD profiles for all the bursts showed a sharp correlation peak with positive delays of the order of a few seconds. The delays obtained in the cross correlation analysis are consistent with light travel times within the binary system. Table 4.4 and 4.5 shows the mean delays obtained for all the 63 bursts. To further model the optical burst profiles, an Optical Transfer Function was generated, details of which are specified below.

2. Optical Transfer Function (OTF)

X-ray reprocessing entails that the optical photons are emitted from the reprocessing region after a finite light travel time between the X-ray photon source and the reprocessing region. The resultant optical signal can then be expected to be delayed. Since the accretion disc, which acts as the dominant source of reprocessed optical emission, has a finite physical extent, the delay is also expected to be smeared. With these two input parameters, an OTF was constructed, using a simple gaussian profile as was indicated by Hynes et al. (2006).

$$OTF(\tau) = \left(\frac{\psi}{\sqrt{2\pi}\sigma}\right) exp\left[-\frac{1}{2}\left(\frac{\tau - \tau_0}{\sigma}\right)^2\right] \tag{4.1}$$

where τ_0 is the mean time delay, σ is the measure of the smear in the delay.

Each X-ray and optical burst was modelled using a constant and a burst profile, to obtain the the best fit burst model parameters like the burst rise time, decay time and the constant background count rate. These parameters were then used to obtain the the X-ray to optical conversion fraction and Optical_{bkg}, which are needed to compute the resultant optical burst profile. The optical persistent count rate is assumed to be a

sum of the optical background count rate and the fraction of persistent X-ray count rate; the total optical count rate is assumed to be a sum of the background optical count rate over the entire burst duration and the fraction of the total X-ray counts. These are expressed as the following two equations:

$$\text{Optical}_{per} = \text{Optical}_{bkg} + \text{X-ray}_{per} \times \text{frac}$$

$$\text{Optical}_{total} = \text{Optical}_{bkg} \text{ x } \text{T}_{burst} + \text{X-ray}_{total} \times \text{frac}$$

where, Optical_{total} is the total expected optical photon counts, Optical_{bkg} is the optical background counts, Optical_{per} and X-ray_{per} are the persistent optical and X-ray count rate and 'frac' is the optical to X-ray conversion fraction. The delays were varied from 0.1 - 10 s in steps of 0.1 s and smear in delays were varied from 0.05 - 5.0 s in steps of 0.05 s. Using the 100 delays and 100 smear values, 10^4 OTFs were generated. The resultant OTF was then convolved with the X-ray light curve to obtain the optical response. A χ^2 fit was performed to assess the best fit model. The delay and smear values corresponding to the minimum χ^2 is then used to plot the best fit optical burst model. The model optical light curves are superimposed on the optical burst data and are shown in Figure 4.8 - Figure 4.17. Details of the delays and smears are specified in Table 4.4 and 4.5. We also tried to assess if there were correlations between the delay and smear parameters as a function of orbital phase. Figure 4.7 shows that such a correlations is indeed absent, ruling out the possibility that the companion star could be responsible for reprocessing of the X-ray bursts.

A total of 76 X-ray bursts and 63 optical bursts observed in the XMM-Newton light curves. The bursts which do not appear in the optical are 6, 7, 15, 23, 32, 35, 38, 47, 55, 59, 63, 64, 74. Due to several unaccountable reasons 4 bursts (21, 22, 62, 71) show problems in the CCF analysis and/or the OTF modeling and four other bursts (51, 52, 69, 70) give unreasonable CCF/OTF delays/sigmas. What is presented here are the 55 best modelled bursts out of the total 63 bursts observed.

OBs-ID	Burst number	CCF value	Mean delay (s)	OTF delay (s)	OTF sigma (s)	OTF chi-square
0160760101	1	0.88	3	2.7	2.55	2.42
	2	0.56	1	4.4	1.75	2.63
	3	0.79	1	4.09	3.25	1.93
	4	0.72	4	2.2	1.05	1.68
	5	0.74	3	3.3	1.5	1.48
	8	0.51	4	2.8	1.3	1.88
	9	0.76	2	2.0	0.9	1.68
	10	0.79	4	3.7	1.85	1.33
0160760201	11	0.76	4	3.6	1.75	2.1
	12	0.69	3	3.6	1.85	1.95
	13	0.73	2	2.2	1.0	1.87
	14	0.83	5	4.8	2.0	1.48
	16	0.68	0	2.3	1.1	1.76
	17	0.79	4	4.2	1.95	1.41
	18	0.75	4	4.0	2.0	1.97
	19	0.44	3	1.9	0.9	1.63
	20	0.6	4	2.3	3.35	2.28
	24	0.76	4	3.2	1.6	1.45
0160760301	25	0.71	3	2.6	1.3	1.5
	27	0.62	2	2.5	1.25	1.55
	28	0.72	3	3.5	1.65	2.78
	29	0.71	7	5.5	2.75	1.78
	30	0.5	5	1.8	0.8	1.68
	31	0.72	2	3.7	1.85	1.67
	33	0.77	2	3.2	1.6	1.48
	34	0.74	3	2.9	1.45	1.37
	36	0.42	2	1.9	0.9	1.51
	37	2	3.3	1.6	1.93	1.9

Table 4.4 Table detailing the CCF and OTF results for Obs-IDs 0160760101, 0160760201 and 0160760301.

OBs-ID	Burst number	CCF value	Mean delay (s)	OTF delay (s)	OTF sigma (s)	OTF chi-square
0160760401	40	0.81	2	3.2	0.94	2.44
	41	0.7	3	3.3	1.65	1.34
	42	0.69	0	4.6	2.2	1.41
	43	0.58	6	2.9	1.3	1.64
	44	0.66	3	2.8	1.4	1.84
	45	0.62	4	4.8	2.0	1.91
	46	0.68	4	4.4	2.3	1.73
0160760601	48	0.68	3	2.3	1.15	
	49	0.62	0	0.5	0.2	2.17
	50	0.7	4	3.7	1.8	1.84
	53	0.74	2	2.6	1.3	2.3
	54	0.74	3	2.4	1.15	1.7
0160760801	56	0.72	3	3.3	1.4	1.61
	57	0.61	6	7.4	3.1	1.72
	58	0.68	8	6.8	2.8	1.76
	60	0.66	3	3.9	1.95	1.86
	61	0.71	6	6.0	2.5	1.43
0160761301	65	0.81	3	3.7	1.85	1.96
	67	0.76	3	3.9	1.95	1.88
	68	0.7	3	2.3	1.15	1.02
	72	0.7	0	2.2	1.0	1.72
	73	0.56	8	6.1	2.55	1.93
	75	0.76	1	1.1	0.55	1.76
	76	0.74	6	1.1	0.55	1.77

Table 4.5 Table detailing the CCF and OTF results for Obs-IDs 0160760401, 0160760601, 0160760801 and 0160761301.

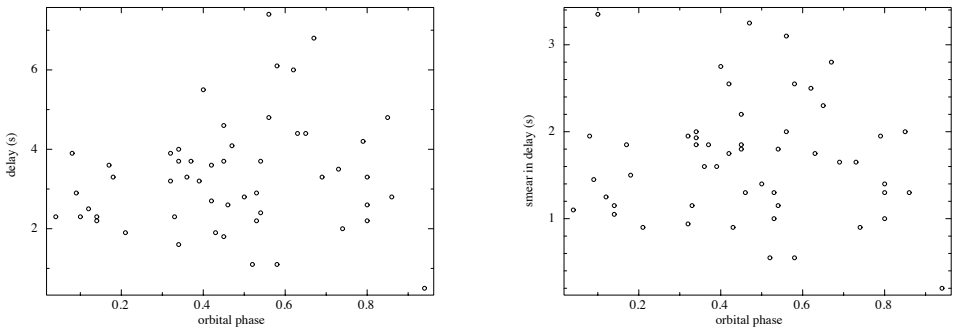

Fig. 4.7 Figure shows the delay and smear parameters as a function of orbital phase. No correlations are observed.

4.3.2 Non-burst simulations

To study the observed non-burst orbital modulations in EXO 0748-676, a series of simulations were carried out using an X-ray binary code [1].

Basic assumptions about the binary system

The program assumes a system containing two stars in circular orbits around their common center of mass. From Kepler's laws,

$$G(m_1 + m_2) = \omega^2 a_s^2 \tag{4.2}$$

$$\omega = \frac{2\pi}{P} \tag{4.3}$$

where, m_1 and m_2 are the masses of the two stars, G is the gravitational constant, ω is the angular velocity of the system, a_s is the binary separation and P is the orbital period. The primary object (star 1) is assumed to be accreting via an accretion disc from the Roche-lobe filling secondary (star 2). The primary star is extremely small in comparison to other system components and emits blackbody radiation which is responsible for irradiating the other parts of the binary. The flux F_1 at a distance d from the primary can be given by

$$F_1 = \frac{L_1}{4\pi d^2} \tag{4.4}$$

[1] Details of the X-ray binary code can be found in: http://www.as.utexas.edu/ elr/Robinson/XRbinary.pdf

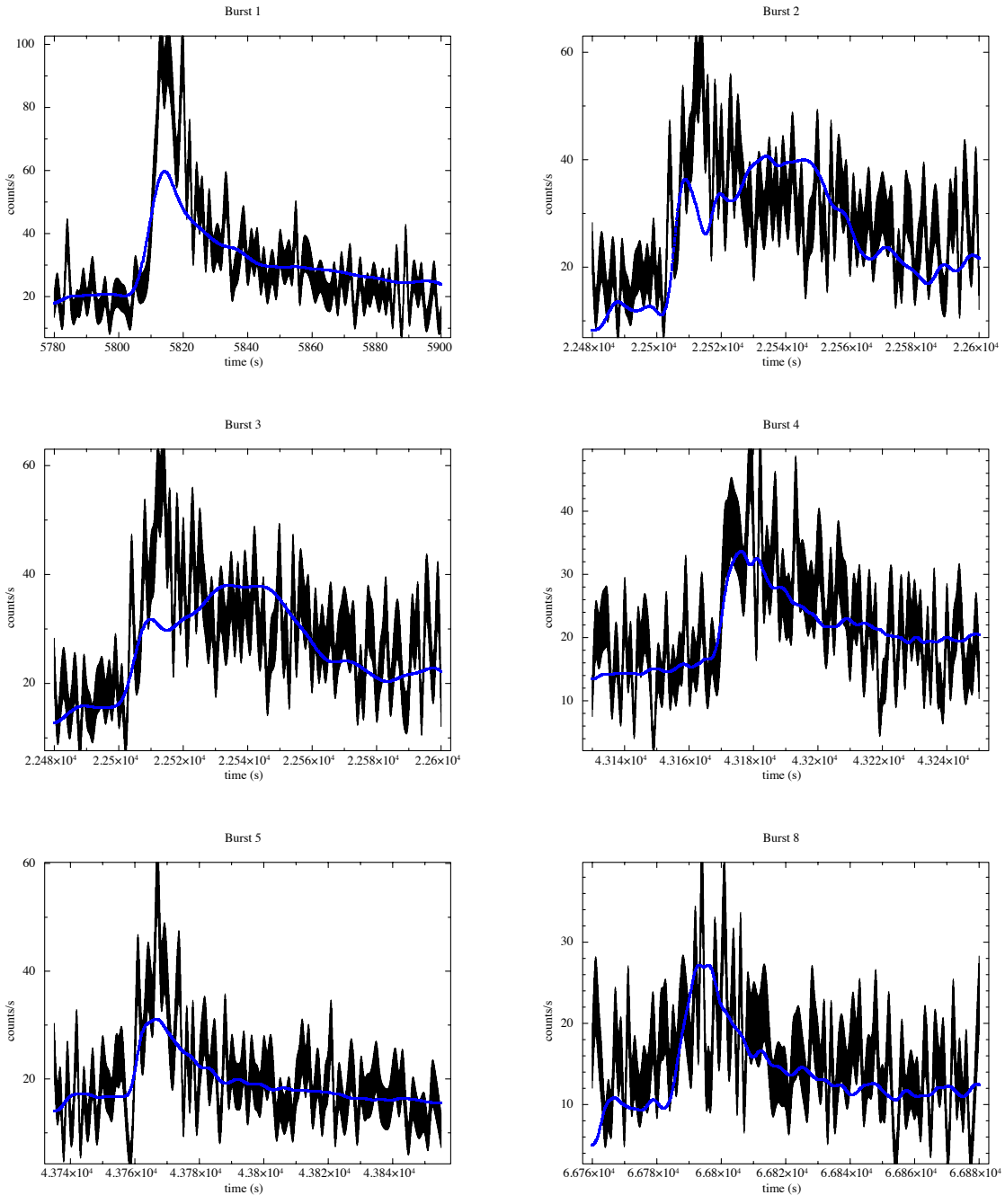

Fig. 4.8 Bursts 1, 2, 3, 4, 5 and 8.

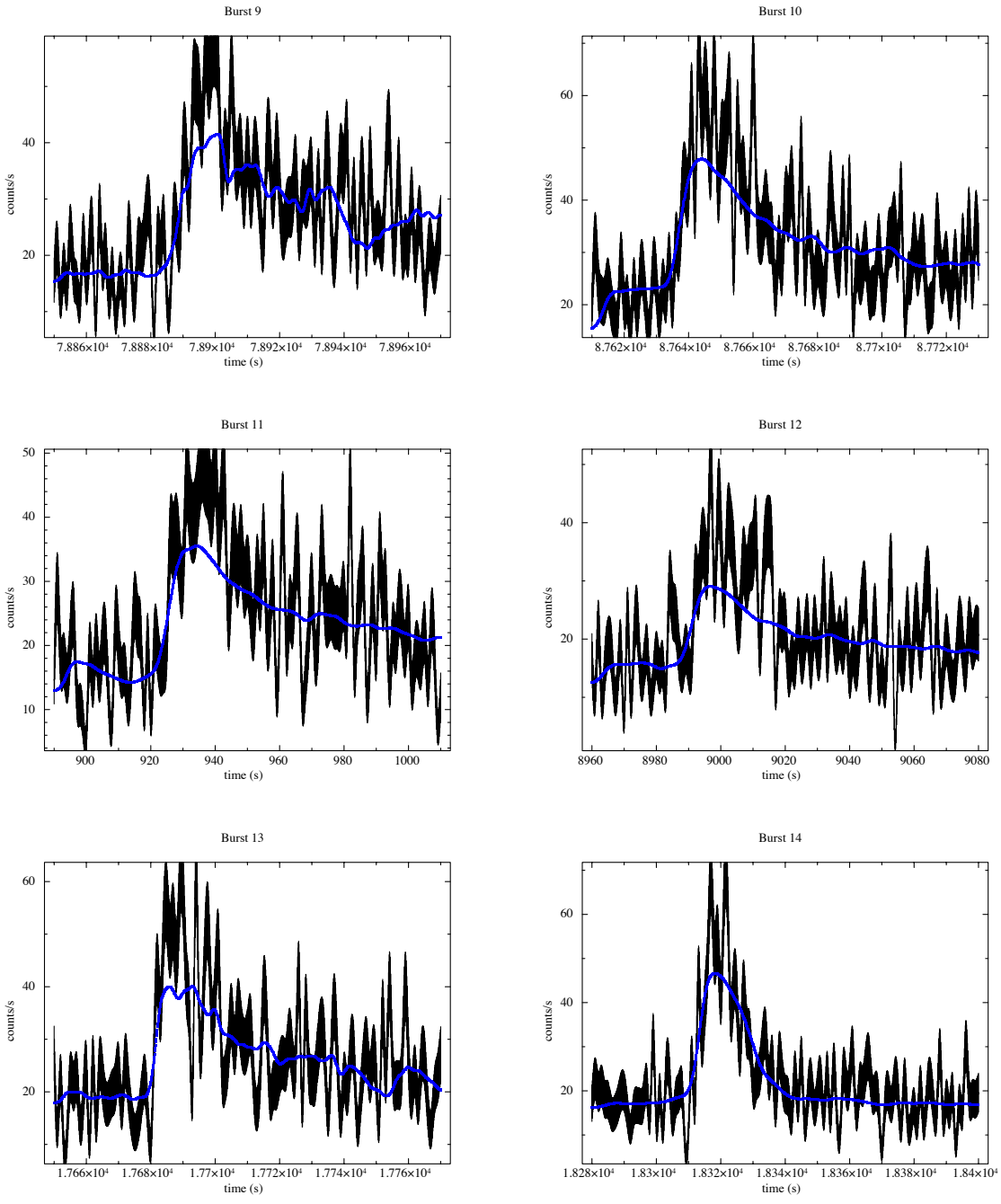

Fig. 4.9 Bursts 9, 10, 11, 12, 13, 14.

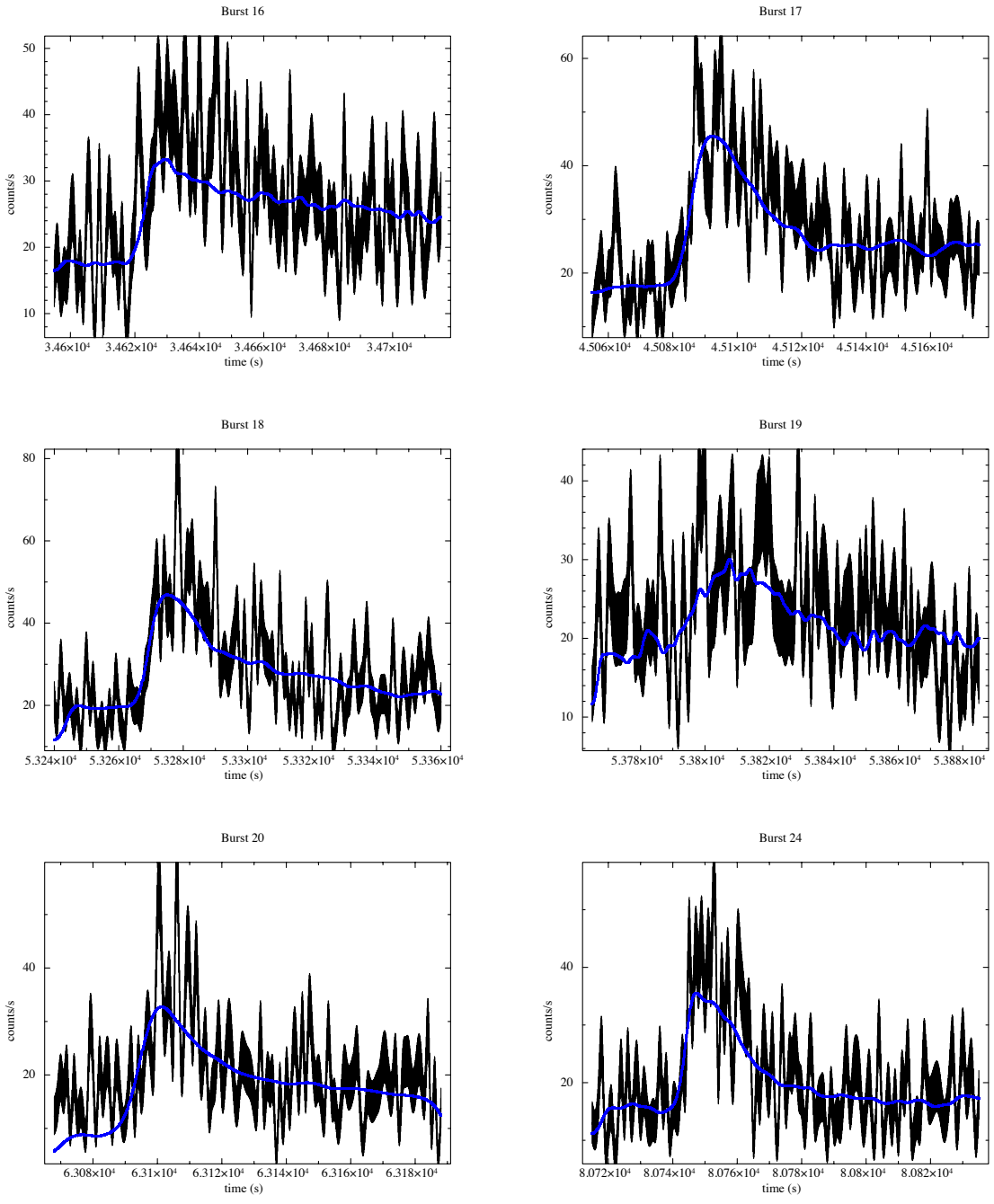

Fig. 4.10 Bursts 16, 17, 18, 19, 20 and 24.

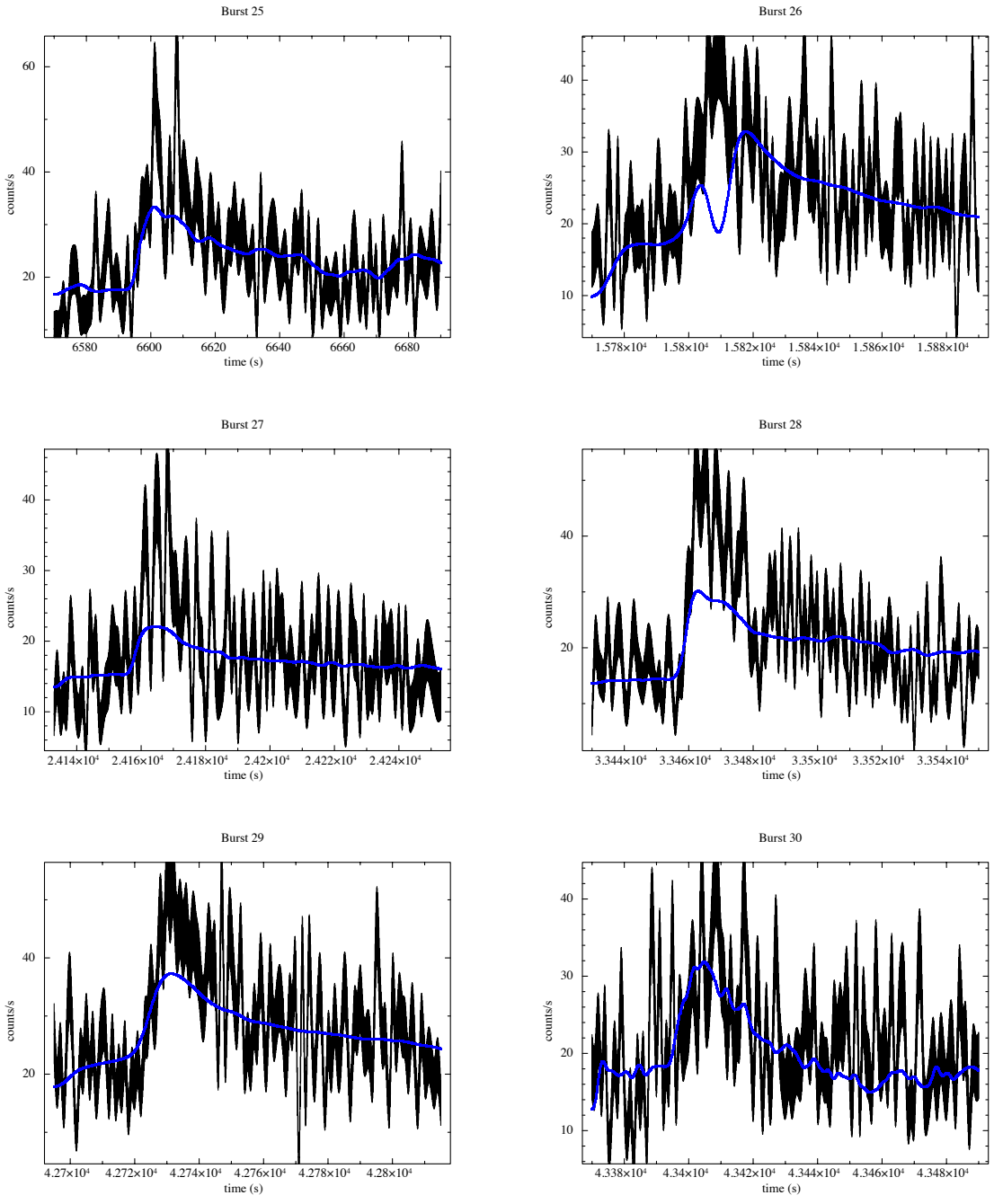

Fig. 4.11 Bursts 25, 26, 27, 28, 29, 30.

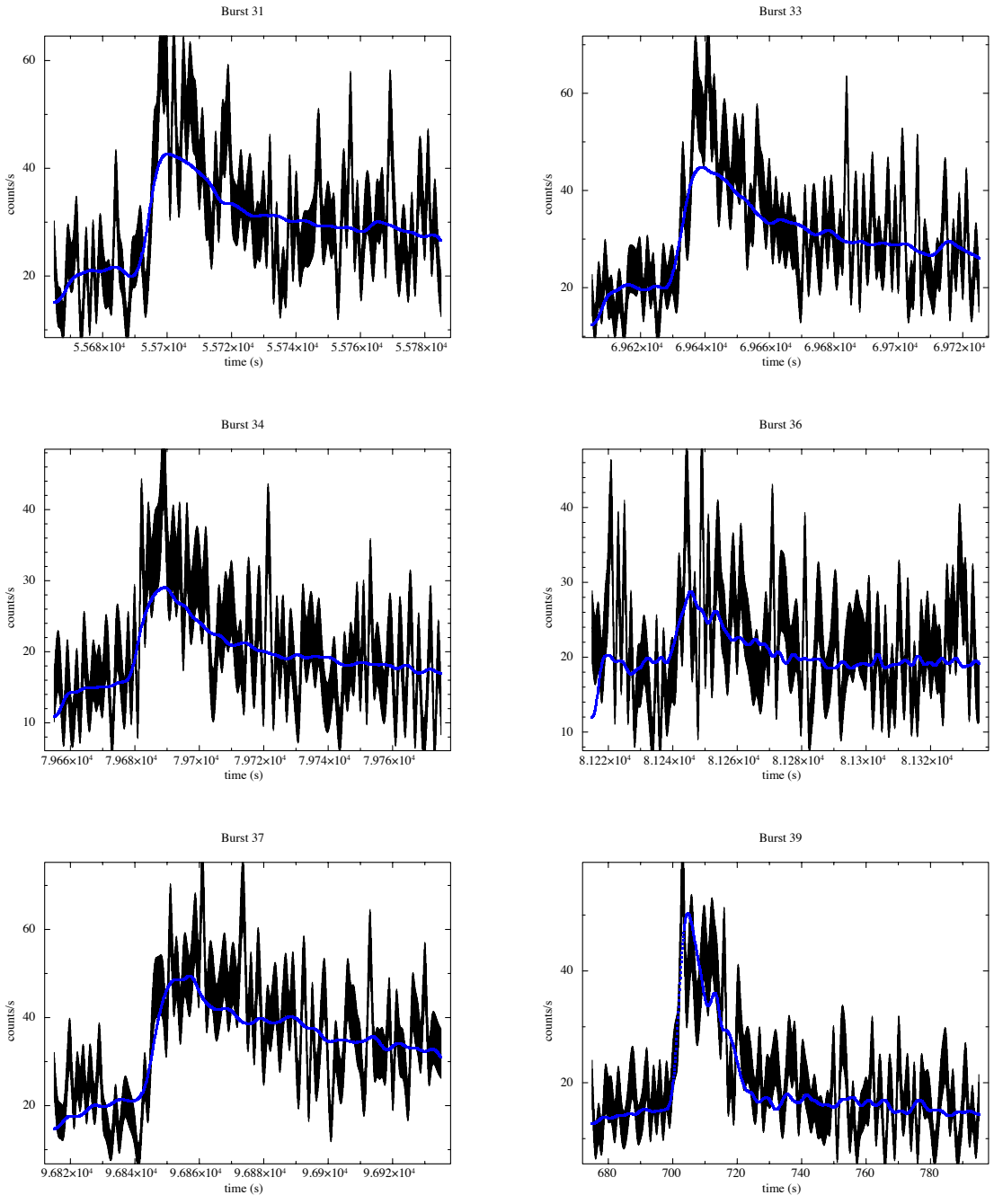

Fig. 4.12 Bursts 31, 33, 34, 36, 37 and 39.

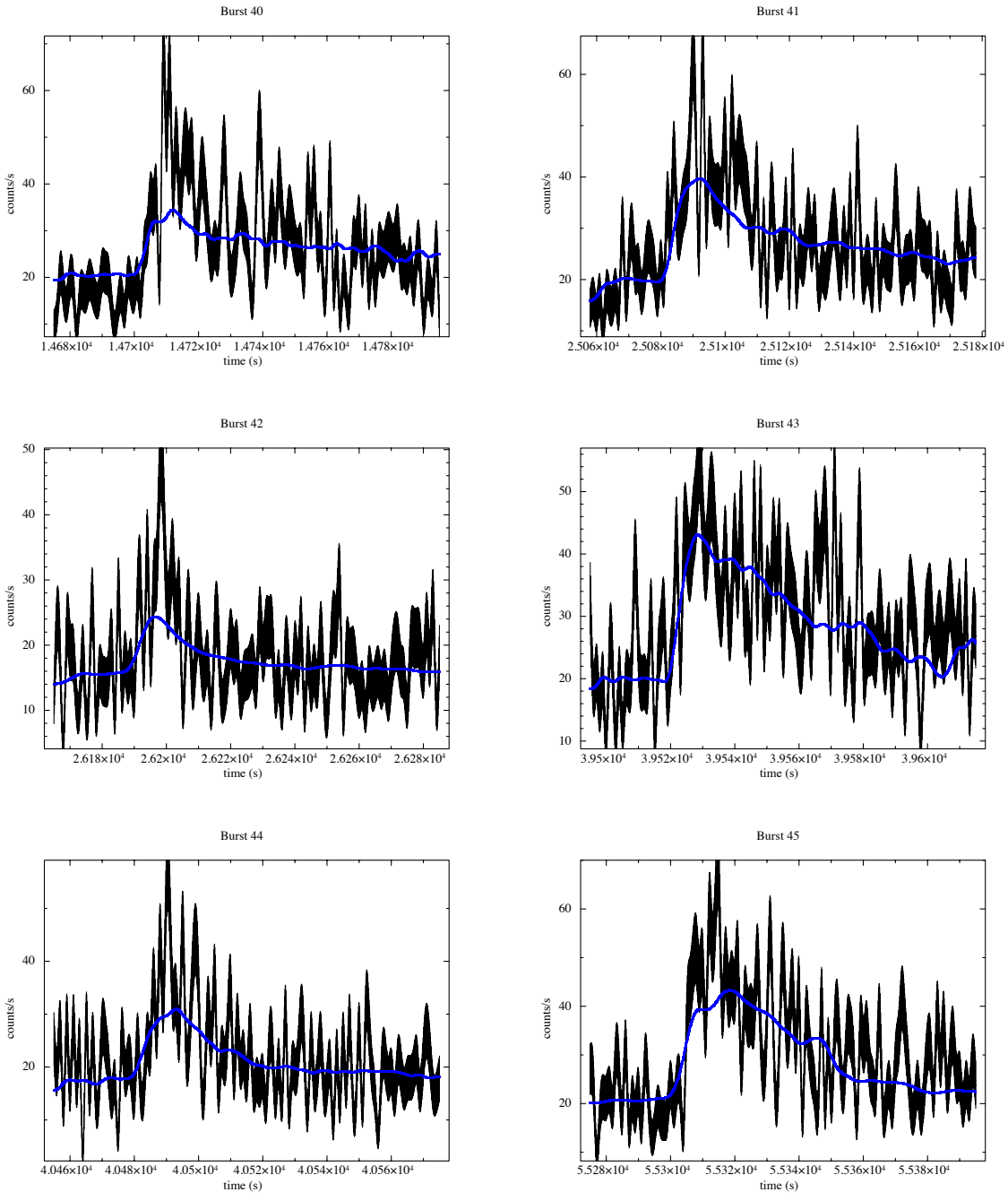

Fig. 4.13 Bursts 40, 41, 42, 43, 44 and 45.

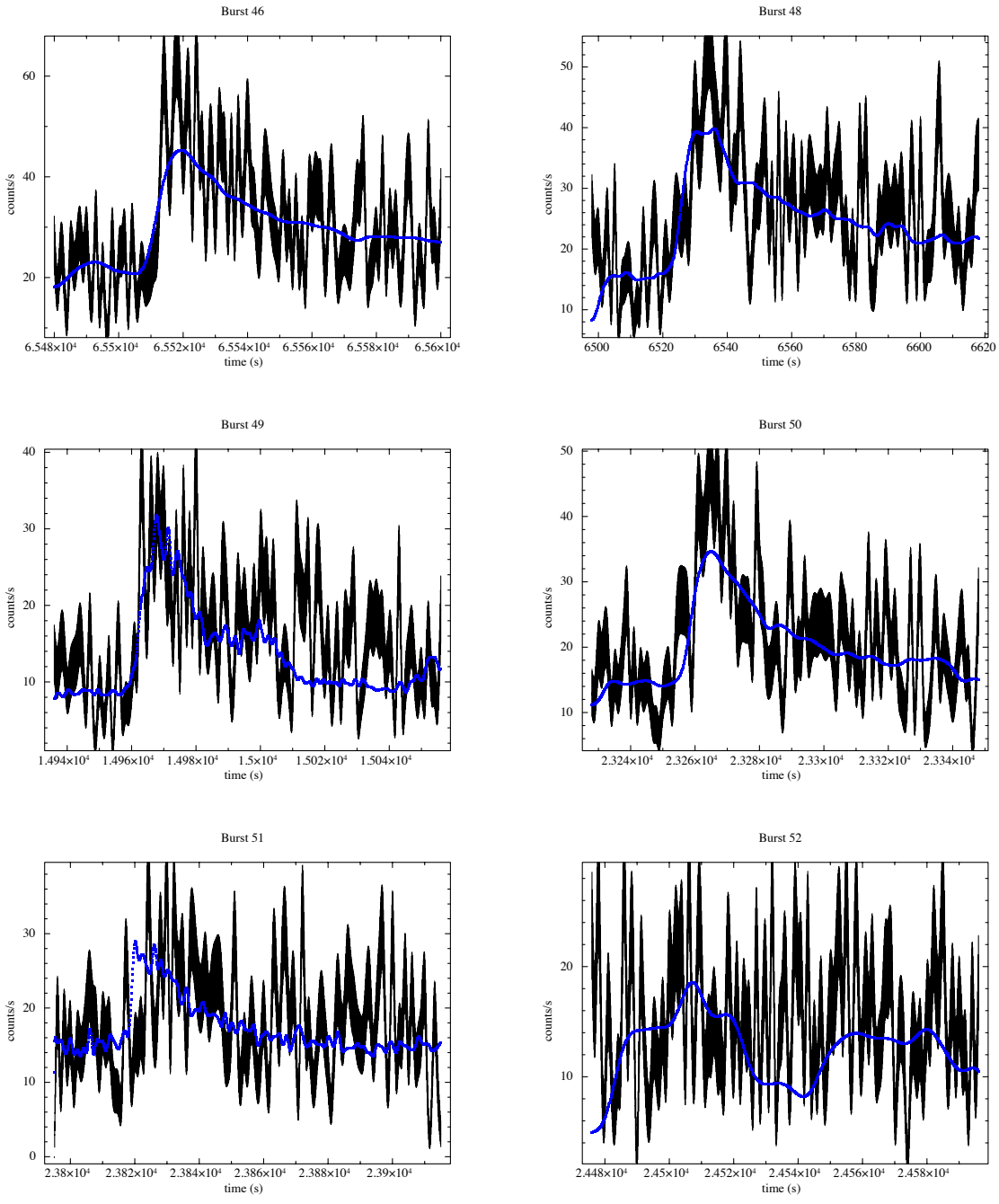

Fig. 4.14 Bursts 46, 48, 49, 50, 51 and 52.

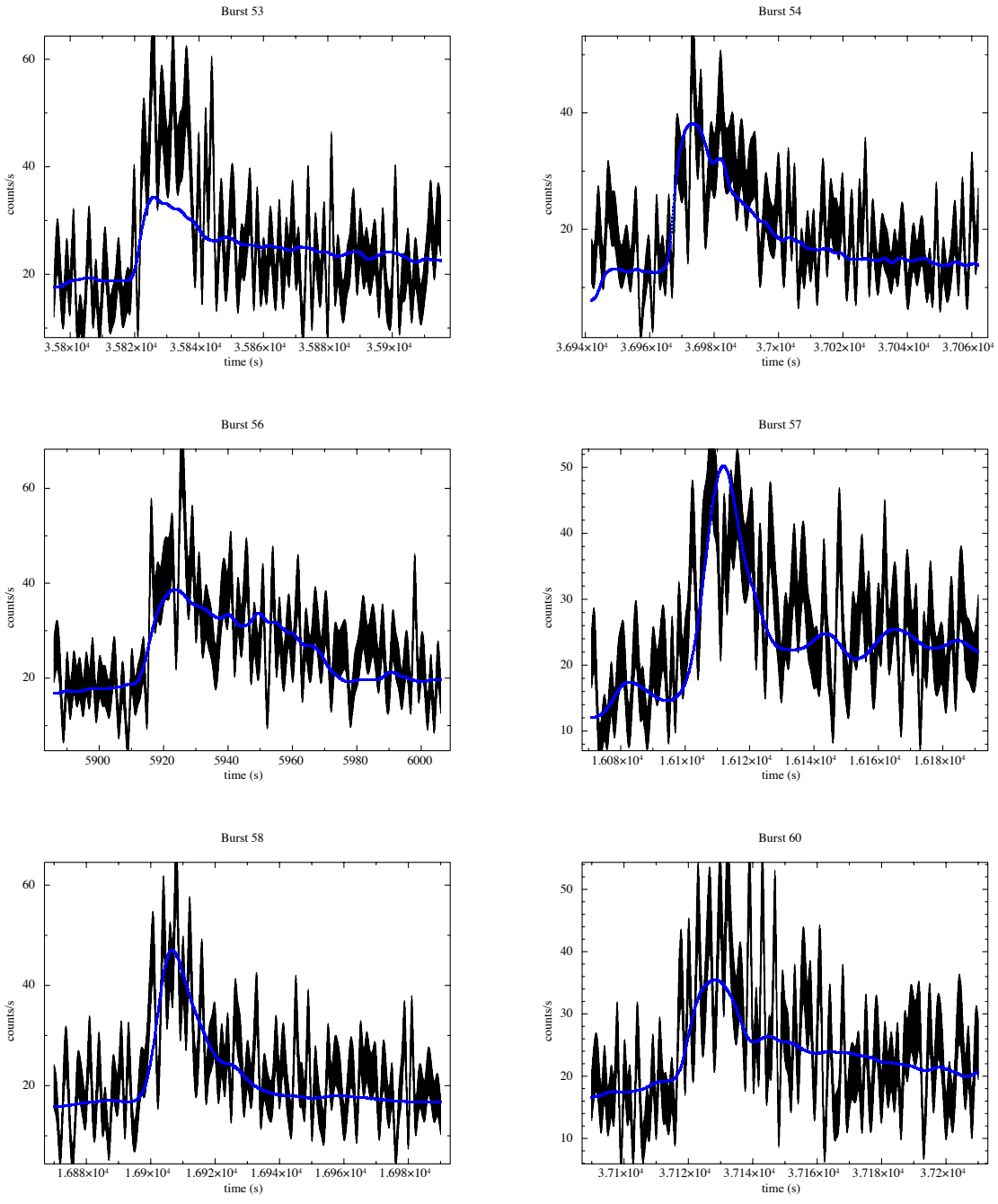

Fig. 4.15 Bursts 53, 54, 56, 57, 58 and 60.

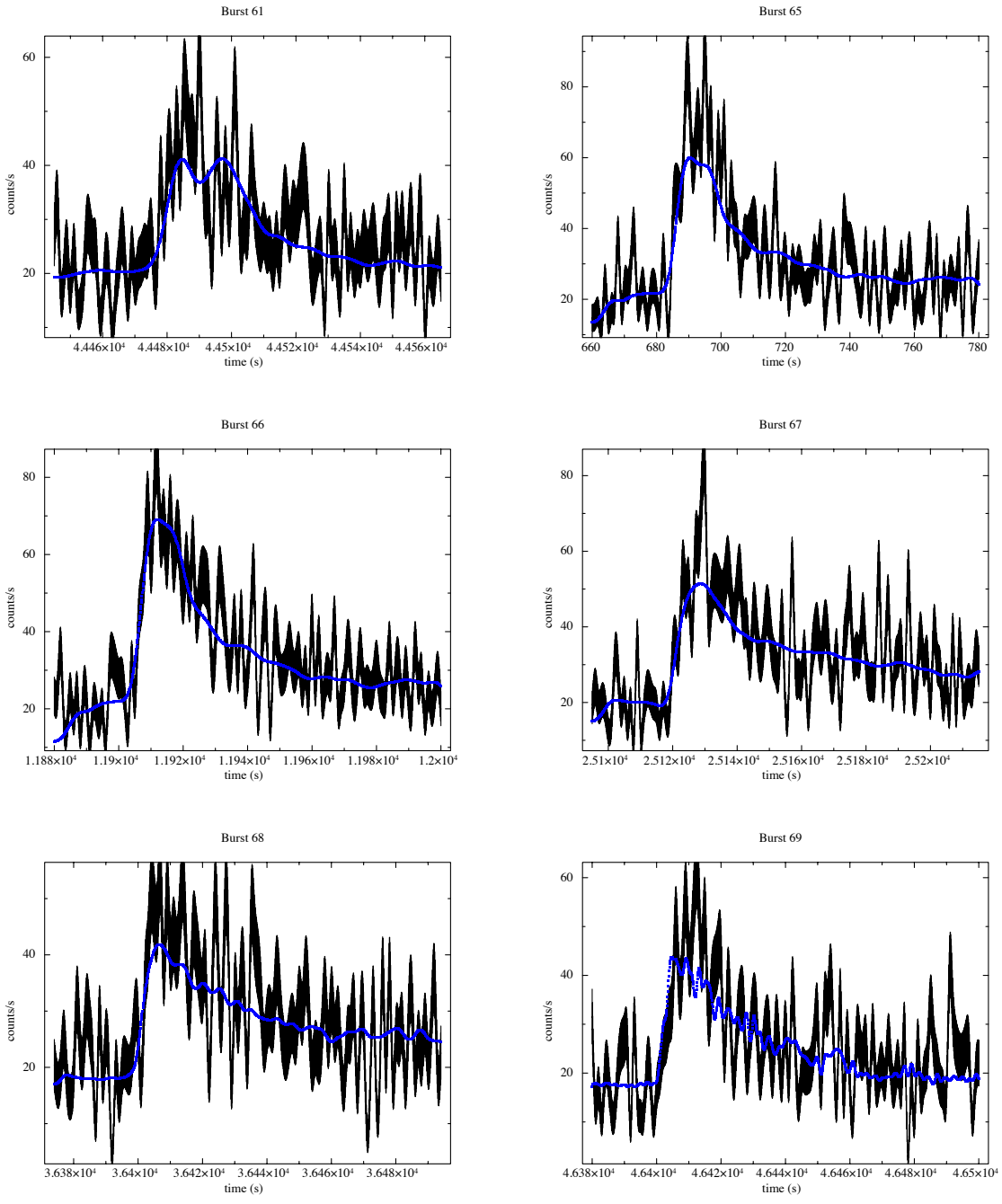

Fig. 4.16 Bursts 61, 65, 66, 67, 68 and 69.

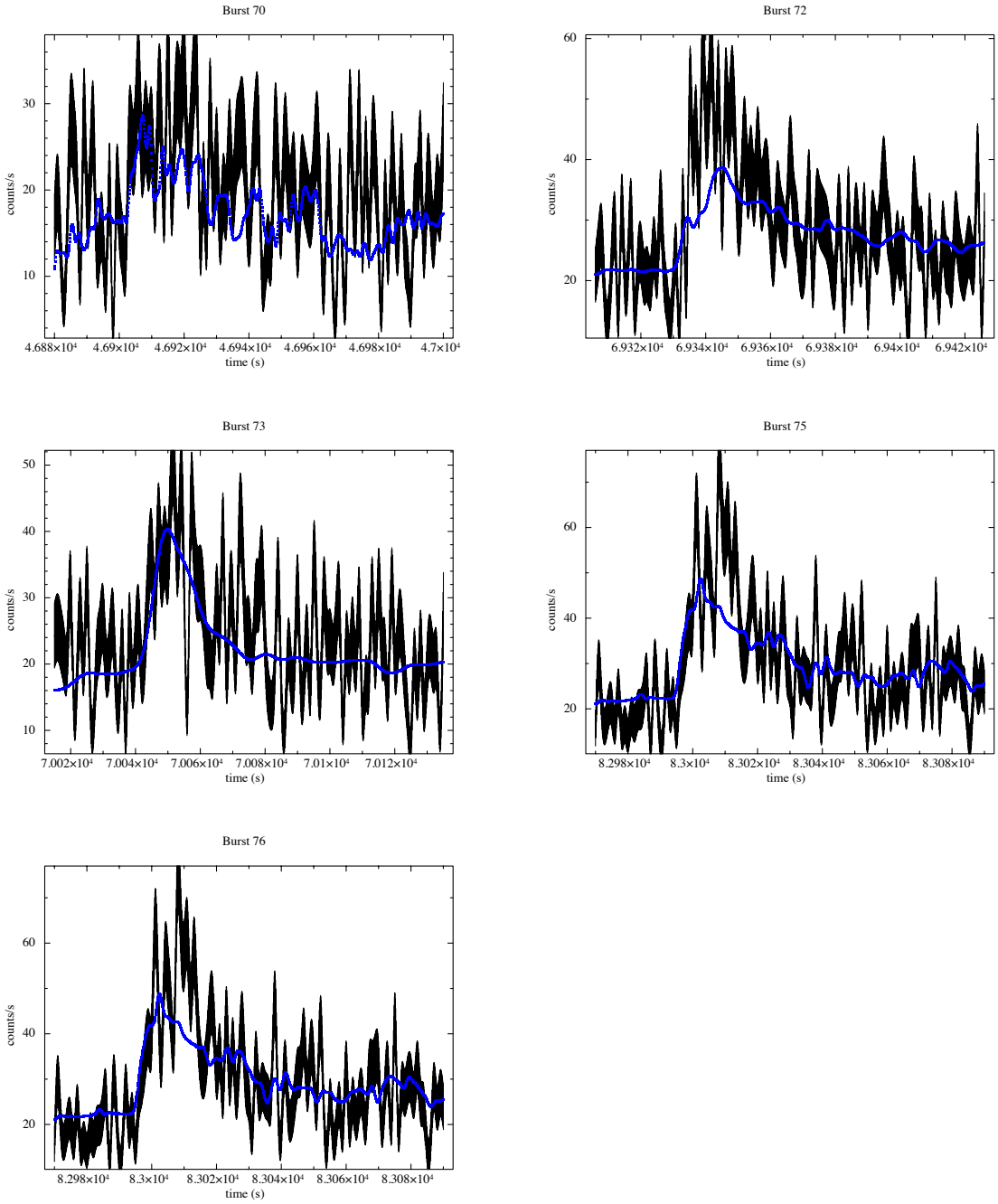

Fig. 4.17 Bursts 70, 72, 73, 75 and 76.

The surface of the secondary star is assumed to coincide with its Roche Lobe and its effective temperature is calculated using its mean effective temperature and mean surface gravity. If irradiation is invoked, the local surface temperatures of the secondary can greatly increase. Local emission is assumed to be dominated by irradiation and the emitting material is not confined to the accretion disc or the stars, it can also involve the accretion disc corona (ADC) or other structures. The geometry of the disc is allowed to be complicated and hence uses ray tracing to compute the light curves. The accretion disc itself is assumed to be in the orbital plane, with other extended components like the disc rim, disc edge and disc torus. The height of the main accretion disc is a power law function of the accretion disc inner and outer radii.

$$H_{main} = H_{edge}\left(\frac{a - a_{min}}{a_{max} - a_{min}}\right)^{\beta_H} \tag{4.5}$$

where H_{edge} is the main disc height at the outer edge.

The accretion disc temperature is allowed to have a power law dependence ($T^4 \propto a^{\beta T}$) on radius or the distribution corresponding to an optically thick viscous disc ($T^4 \propto \frac{K}{a^3}[1 - (\frac{a_{min}}{a})]^2$), where a is some arbitrary radius between a_{min} and a_{max}. Flux from the inner disc is another source of irradiation, particularly in black hole binaries. The preliminary version of the program also allows one to incorporate the irradiation due to X-ray heating from the ADC.

The input binary parameters that are to be specified include the binary inclination (i), orbital period (P) and mass ratio ($q = M_2/M_1$). The disc geometry can be specified with the disc radius (a), height of the disc as a function of a and also the disc-rim height as a function of disc azimuth (ϕ). The code also allows for a torus centered on the compact object, with parameters including the radial distance from the compact object, height and thickness of the torus. The flux parameters include power-law disc temperature as a function of disc radius, outer disc temperature, luminosity of the neutron star, the inner disc temperature and the accretion disc corona (ADC).

The optical flux of the system is calculated by invoking the reprocessing of X-ray to optical from the accretion disc as well the companion star. Between the temperatures of 3500 K and 8000 K, the heated disc is assumed to emit like a blackbody, while the companion emits like a normal stellar atmosphere. Beyond 8000 K, the companion surface is assumed to emit like a black body. The filter sets available for use by the

code are the Johnson UBV, the Cousins RI and the Jonson JHK sets; additionally one can specify a square pass-band.
The observed overall wavelength-dependent flux from the system is:

$$F(\lambda) = \int I(T_{eff}, g, \mu, \lambda).d\vec{A} \tag{4.6}$$

where, I is the local specific intensity, T_{eff} is the local effective temperature, g is the local gravity and λ is the wavelength.
The light curve is measured in a specific wave-band which is described by a response function:

$$R_X(\lambda) = S_X(\lambda) / \int S_X(\lambda) d\lambda \tag{4.7}$$

where S_X is the unnormalized response function. Using the Flux and the response function, a flux density F_X is calculated as follows:

$$F_X = \int R_X(\lambda) F(\lambda) d\lambda \tag{4.8}$$

The flux density F_X is a function of orbital phase and this is what is generated in the form of a light curve. A χ^2 fitting is then carried out to compare the observed and model light curve at the exact the orbital phase. The best fit model is obtained by χ^2 minimization.

Results

One single orbit from Obs-ID 0160760201 has been used to produce the different model light curves. The plots represent the intensities as a function of orbital phase. The y axis intensity values do not represent the actual optical intensities, since the code produces the orbital modulation with a high preset normalization value. The input parameters used for the code are as follows:

- The orbital period P = 0.15916 days
- Mass of neutron star $M_1 = 1.4\ M_\odot$
- Mass ration $q = M_2/M_1 = 0.35$
- Inclination (i) varied from 75 - 83°
- Luminosity of star 1, $L_1 = 2.52 \times 10^{36}$ ergs/s
- Temperature of star 1, $T_1 = 1.2 \times 10^7$ K

- Temperature of star 2, T_2 = 3800 K
- Albedo of star 2 = 0.5
- Eccentricity of the accretion disc = 0.1
- Binary separation a = 1.0×10^{11} cm
- Inner accretion disc radius a_{min} = 0.00001a (10 km)
- Outer accretion disc radius a_{max} = 0.26a (2.6×10^5 km)
- Accretion disc: temperature distribution is that of a steady state, optically thick, viscous disc with total disc luminosity = 1.3×10^{36} erg/s
- Square band pass: 1500 - 5000 Angstrom

The effect of these input parameters on the output model light curves have been tested for 4 simple scenarios described below:

- **Two stars and no accretion disc:** At phase 0.0 the companion completely blocks the primary X-ray photons, cutting off the optical emission completely. At phase 0.5 the primary star blocks the secondary, causing a partial secondary eclipse, resulting in a partial cut off of the optical emission. This is because the primary is smaller in extent than the secondary. No further modulations are observed (Figure 4.18).
- **Two stars with a medium luminous disc:** Accretion disc contributed more to the optical emission. Enhances the optical flux around 0.5 much. Accretion disc visible throughout the orbit, except during the eclipse at phase 0.0 (Figure 4.19).
- **Two stars with an irradiated accretion disc:** Irradiation heats up the accretion disc, resulting in different parts of the disc emitting differently. Profile gets modulated considerably. Enhanced optical emission around phase 0.5 (Figure 4.20).
- **Two stars with an irradiated disc and two disc rims:** Modulated profile corresponding to the location and angular extent of the disc rims (Figure 4.21).

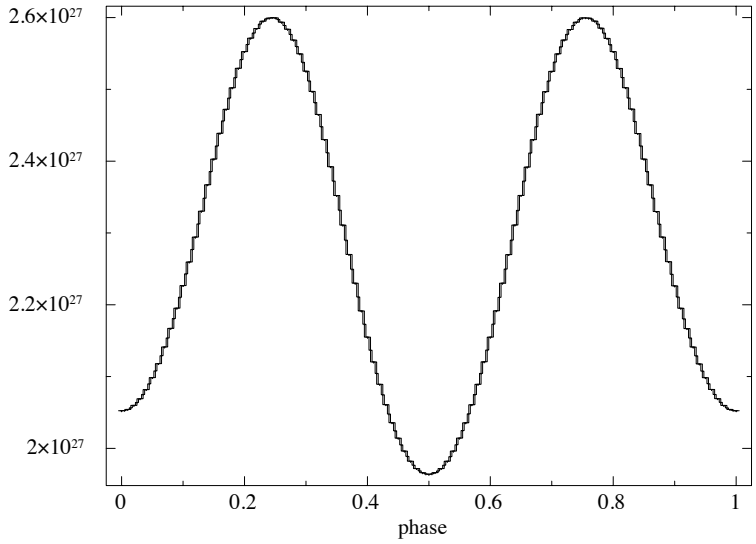

Fig. 4.18 Count rate as a function of orbital phase for two stars and no accretion disc.

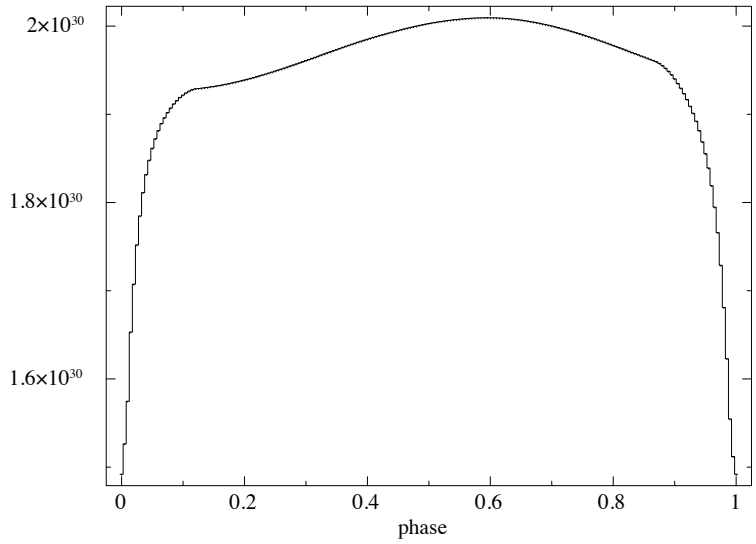

Fig. 4.19 Count rate as a function of orbital phase for two stars and with an accretion disc.

We also carried out the simulation on orbit 2 of Obs-ID 0160760201. The fit required an irradiated accretion disc along with two disc rim components at phases 0.2 and 0.6. Figure 4.22 shows the optical orbital cycle data (black) and the simulated profile (green)

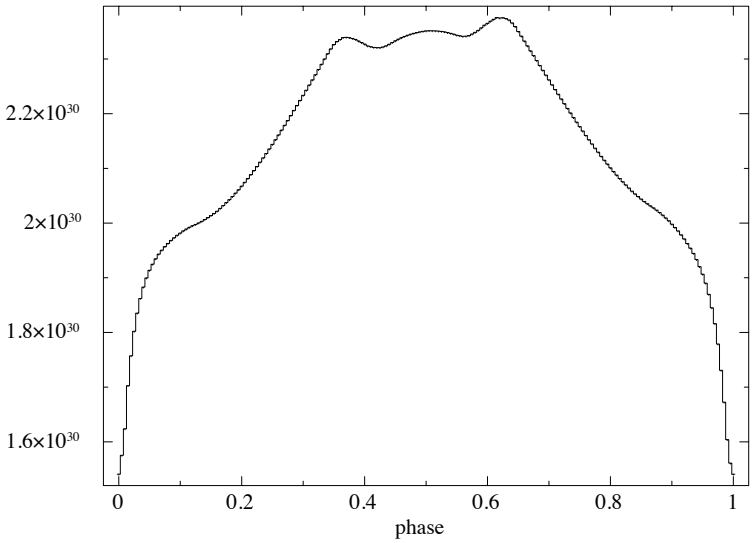

Fig. 4.20 Count rate as a function of orbital phase for two stars with an irradiated accretion disc.

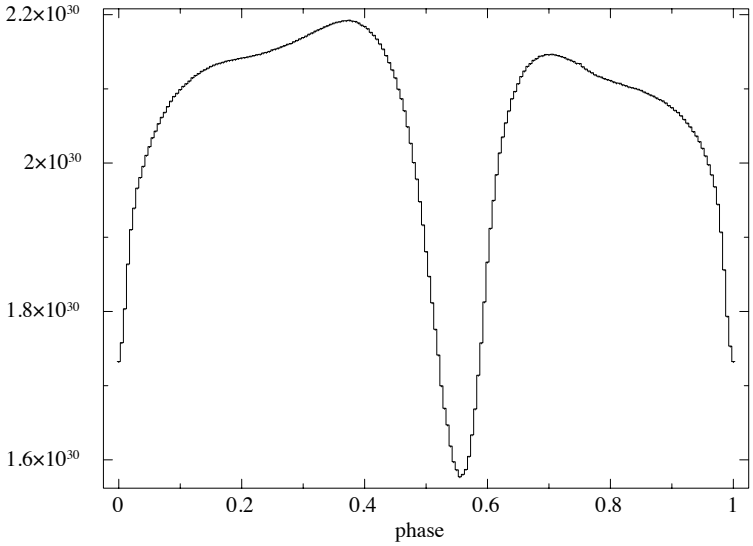

Fig. 4.21 Count rate as a function of orbital phase for two stars with an accretion disc and disc rims.

overlaid. The count rate intensity is shown as a function of orbital phase. Detailed modelling of all the 36 orbital cycles from all the XMM-Newton observations is being

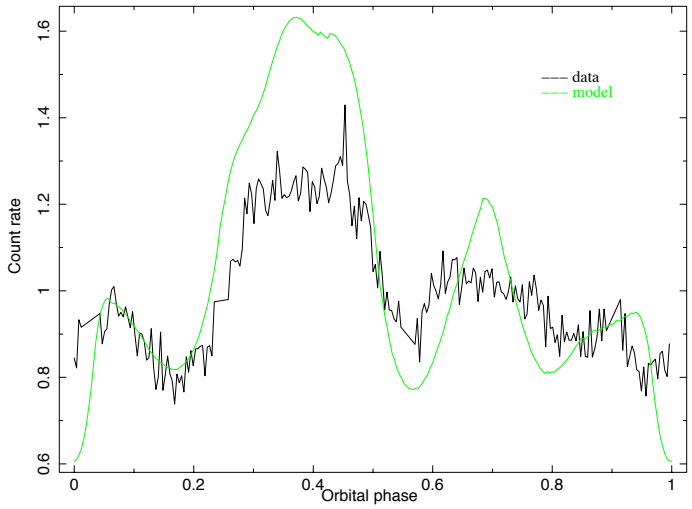

Fig. 4.22 Simulations of orbit 2 from Obs-ID 0160760201 using the X-ray binary code. Count rate as a function of orbital phase is shown for this orbital cycle.

currently examined by optimising the system parameters over a range of inclinations, temperatures and accretion disc parameters.

4.4 Discussion

Detailed studies with simultaneous X-ray and optical light curves of EXO 0748-676 have been conducted using the EPIC-PN detector and the OM on-board XMM-Newton from a set of observations carried out during the hard spectral state of the source. A total of 36 simultaneous and complete, X-ray and optical orbital cycles were examined. The X-ray and optical dips are observed to occur at many different orbital phases with varying depths and widths throughout all the 7 observations. The soft X-ray and the optical emission vary enormously at sub-orbital timescale and also between successive binary orbital cycles. The non-burst, non-eclipsing X-ray (soft and hard) and optical emission exhibit a weak correlation at timescales of a few 1000 s. EXO 0748-676 has been extensively studied in both X-rays and optical in the past and the nature of its X-ray and optical co-variability has been known to change over the years. Results obtained from the work on non-burst orbital modulations provide further indications to the evolving nature of the accretion disc in this source. The burst simulations results suggest that the best fit OTF delays correspond to $\sim$ 3-8 s, which is consistent with the light travel times of this LMXB system and the preliminary simulations of the non-burst optical orbital modulations suggest the requirement of outer disc rims at different or-

bital phases in order to account for the dipping phenomenon observed in the light curves.

4.4.1 Variability In X-rays (Soft and Hard)

During the observations reported in this study, the average unabsorbed X-ray flux of EXO 0748-676 was 2.25×10^{-10} erg cm^{-2}s^{-1} (Boirin et al., 2007), which is nearly 1% L_{Edd}. This persistent flux, representative of the mass accretion rate of the neutron star, has been one of the lowest values ever measured for this system before it went into quiescence in 2008 (Hynes and Jones, 2009). The system was in an X-ray 'faint-hard' state throughout all the 7 observations reported here. The soft X-ray light curves, excluding the thermonuclear bursts and residual eclipse emission, exhibit a large rms in their variability. The hard X-ray emission, being more or less steady, indicates an unvarying accretion rate and persistent hard X-ray emission from the neutron star.

The soft X-ray light curves, in addition to the eclipses and the bursts, exhibited intense dipping over a range of orbital phases. The dipping behavior, in its depth, continuity, orbital phase range, etc. changed considerably from one orbital cycle to the next. The absorbing efficiency of the dips is more pronounced at lower energies. This has been observed in other sources like 4U 1254-690, 4U 1323-62 (Díaz Trigo et al., 2009; Boirin et al., 2005; White and Swank, 1982b). The duration of the X-ray dips provides an estimate of the azimuthal angular extent of the absorbing material. As can be seen in Figures 4.2, 4.3 and 4.4, the duration of the dips exhibits a large variation: multiple very narrow dips (as short as 1% of the orbital period) to one or two wide dips (as long as ∼40% of the orbital period). The soft X-ray dips therefore indicate simultaneous presence of multiple vertical structures with narrow (a few degree) to broad (∼150 degree) azimuthal extent.

EXO 0748-676 has shown a bimodal behavior of transitioning between the hard and soft spectral states in X-rays, while accreting at low-to-moderate rates (0.01 - 0.5 L_{edd}). Figure 4.23 shows the RXTE/ASM light curve indicating the epochs of two XMM-Newton observations, one during a bright soft spectral state in 2005 and another during a faint 2003 (this work) hard spectral state. Excluding the thermonuclear bursts, the 2003 observation light curve shows an average count rate of 25, while the soft state 2005 observation has a count rate that is about an order of magnitude higher. Ponti et al. (2014) showed that the dipping phenomenon in the soft (0.5-5 keV) band appears less intense in soft spectral state compared to the hard spectral state. The dips in the

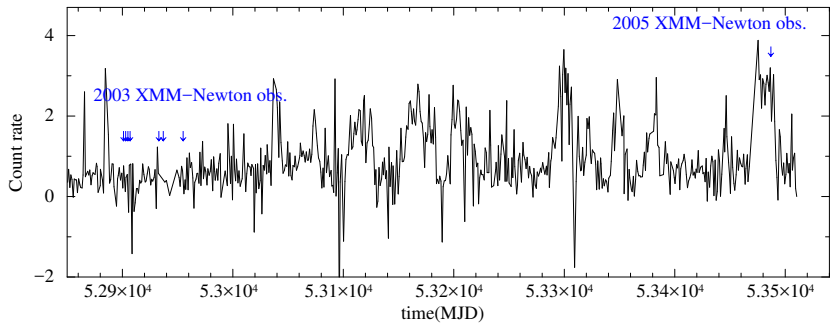

Fig. 4.23 The *RXTE*-ASM light curve of EXO 0748-676 showing the high-intensity 2005 soft state and low-intensity 2003 (this current dataset) hard state, marked with arrows. These very different X-ray states also show up in the spectral properties of the source.

soft state are shallow, extending to almost 75% of the average count rate. The hard state dips on the other extend much deeper, going down to ∼33% of the average count rate (see Figure 4.24).

Interestingly, light curves from an XMM-Newton observation in 2003, studied earlier by Díaz Trigo et al. (2006) and Boirin et al. (2007), which have also been analyzed in the current work, show that the dips have widely different characteristics, including some appearing after the eclipse (Obs-IDs 0160760601 and 0160760801, Figures 4.2, 4.3 and 4.4), even while the source remained in the same hard spectral state.

The soft X-ray photons, get absorbed by disc structures at different azimuthal angles, due to which they display orbital phase-dependent dipping behavior. The structures in the accretion disc that cause the dips can have various origins like irradiation induced vertical structure or warps, stream-impact bulge, ionized absorbers etc., which are described in detail below.

i) Irradiation induced vertical structures:
Irradiation effects are often invoked in a number of disc accreting LMXB systems (de Jong et al., 1996) like 4U 1822-371 (Mason and Cordova, 1982) and 4U 1916-05 (Callanan et al., 1995; Homer et al., 2001). These effects could lead to large scale height and non-axisymmetric vertical structures, the result of which, could be the observed soft X-ray modulations at different orbital phases (Hakala et al., 2005). **Irradiation induced structures act as reprocessing sites for the generation of lower energy photon like UV/optical.** Radiation-driven accretion disc warps can

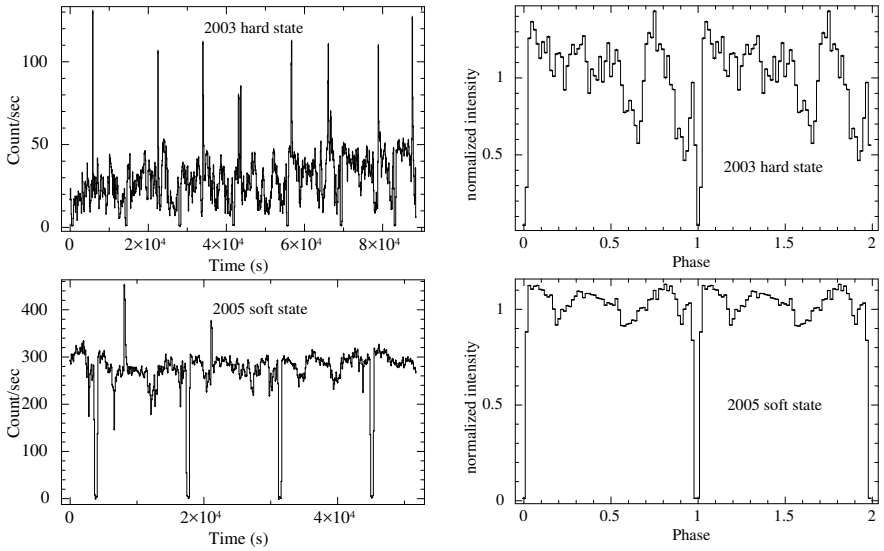

Fig. 4.24 XMM-Newton light curves (2.5-10.0 keV) with a binning of 100 s and normalized average orbital profiles for the 2003 Obs-ID 0160760101 (top- left and right) and the 2005 Obs-ID 0212480501 (bottom- left and right) are shown. The 2005 soft state folded profile shows less intense X-ray dips as compared to the more intense dips when the source was in a hard state in 2003.

lead to instabilities that would produce many of the observed modulations for LMXBs (Pringle, 1996). Warped and precessing accretion discs lead to X-ray heating of outer disc portions in an azimuthally asymmetric way (Clarkson et al., 2003). For disc accreting LMXBs, hosting a primary neutron star, warping effects get prominent after $\sim 3{\times}10^8$ cm . Warping thus affects the outer regions of accretion discs (Pringle, 1996). Although Ogilvie and Dubus (2001) showed that warping may not be prevalent in all LMXBs, there is strong observational evidence for the presence of some form of disc structures above the disc plane in EXO 0748-676. Long term light curve studies of EXO 0748-676 were performed by Kotze et al. (2009) using RXTE ASM, in which a period search using the Lomb Scargle method was adopted. They reported a super-orbital period corresponding to 180.8±0.3 d during the "active" state and conclude that this super-orbital periodicity could be a consequence of coupled precessional and warping effects. The current dataset, having been obtained from a nearly 60 day long observing campaign was not sufficient to look for super-orbital period signatures. Furthermore, Homan et al. (2015) show that origin of the 1 mHz low frequency QPO in EXO 0748-676 could be geometrical in nature, possibly a misaligned, precessing inner accretion flow.

ii) Stream-impact bulge at the outer accretion disc :
Changing aspects of the X-ray heated regions of the disc like the stream-impact plasma

bulge at the outer disc and/or the ionized plasma above the disc may also contribute to the soft X-ray variability at different orbital phases (White and Mason, 1985). They could be responsible for blocking the direct view of the X-ray emitting region near the inner accretion disc, which could cause X-ray dips at different orbital phases. The accretion stream and disc impact model has been invoked to explain the pre-eclipse dips, the anomalous dips as well as the dip marching effect in Her X-1 (Igna and Leahy, 2012).

iii) Ionized absorber :
In a study involving a number of disc accreting LMXB dippers, Ponti et al. (2014) showed that the presence of a large ionized absorbing component, reduces the opacity, which causes less intense X-ray dips in the soft state compared to the hard state (Figure 4.24). To explain the nature of the ionized absorber responsible for the dips, two strikingly contrasting models are often invoked in literature. The first set of models, commonly referred to as complex continuum models (Church et al., 1998; Church and Balucinska-Church, 1995) assumes the X-ray emission originates from a point-like blackbody together with an extended corona, where the dipping spectra are modelled by partial or progressive covering of the extended corona. The second approach, by Díaz Trigo et al. (2006), considers simple ionized absorbers, and self-consistently demonstrates that changes in the properties of an ionized absorber provide an alternative and satisfactory explanation for the overall spectral changes during dips for EXO 0748-676 using the current XMM-Newton dataset Obs ID 0160761301, without having to invoke partial or progressive covering models.

A detailed spectral study of the Obs-ID 0160761301, considering all the X-ray dips, by (Díaz Trigo et al., 2006) revealed that the changes in the spectral continuum from persistent to dipping intervals, reflected in a significant increase in the absorption column density of the ionized absorber by a factor of 5 and a decrease in the ionization parameter $\log(\xi)$ by $\sim$0.2. Their study indicated that, in EXO 0748-676, which shows sharp and deep dips, the absorber is significantly less ionized and relatively cool ($\log(\xi)<2.5$) unlike other LMXB dipping sources with more ionized absorbers.

4.4.2 Lack of Correlated variability between X-rays and optical

Global optical/NIR and X-ray correlation studies conducted in many low magnetic field (B $\leq 10^{11}$ G) neutron star LMXBs by Russell et al. (2006) showed that the optical

emission can be accounted for by thermal emission due to reprocessing except in cases where the source spectral state is hard and the source luminosity is significantly high ($>10^{37}$ ergs/s). In such scenarios, synchrotron emission from jets contributes heavily to the NIR and optical emission. However, since X-ray reprocessing dominates the optical emission for lower luminosities, which is the current case, changes in the X-ray spectral state are expected to reflect in the optical emission for this binary.

Simultaneous X-ray and optical observations of thermonuclear X-ray bursts in LMXBs are extremely useful in understanding the X-ray reprocessing phenomena and also to investigate the relative importance of two main processes of optical emission: i) X-ray heating and ii) viscous dissipation. Reprocessing of X-ray bursts into optical emission has been observed in many LMXB sources (see Section 1.2.4). It is an expected consequence of interception of a fraction of the primary burst X-ray photons by the disc and/or companion surface. Dubus et al. (1999) showed that a point source is incapable of irradiating a planar (non-warped) stationary disc. This is because, self-screening would prevent the outer parts from getting heated. This renders the non-irradiated disc model inadequate to explain the optical emission from a large fraction of persistent LMXBs. Emission of reprocessed optical photons would require structures, that are usually induced by irradiation or X-ray heating. These structures then act as reprocessing sites. A concave disc (which is also a consequence of irradiation), extending to larger scale heights as one moves outwards (de Jong et al., 1996), ensures that the outer disc intercepts some part of the X-rays. In the case of EXO 0748-676, the observed time delays between the X-ray and optical bursts are consistent with the binary separation (Hynes et al., 2006; Paul et al., 2012). Smearing in the delay times, also indicates a finite extent of this reprocessing region which is most likely located at the outer accretion disc. Reprocessing of the thermonuclear X-ray bursts therefore indicate that, since a significant part of the burst X-ray emission does get reprocessed at the outer accretion disc, same may hold true for the non-burst emission.

Considering a conversion factor for the non-burst reprocessing phenomenon, similar to the burst reprocessing, roughly 24% of the total optical emission can be assumed to be due to the reprocessing of X-rays. However, this is only a lower limit, and a much larger fraction of the optical emission is expected to be due to X-ray reprocessing. The X-ray emission from disc-accreting LMXBs is anisotropic and is enhanced in the direction perpendicular to the disc plane (Fujimoto, 1988; He and Keek, 2016). Also,

the disc persistent X-ray emission tends to have a higher degree of anisotropy compared to the burst emission. Thus, for high inclination LMXB systems like EXO 0748-676, the observable X-ray to optical conversion ratio of the non-burst emission would be higher compared to the burst emission. The residual optical emission during the X-ray eclipses is partly from the companion star and partly from the un-eclipsed disc. Considering an average source magnitude of ∼17 (obtained from the OM observations), the optical flux is $\sim 7.0\times10^{-13}$ erg cm^{-2}s^{-1} in the V-band compared to the bolometric X-ray flux of 2.25×10^{-10} erg cm^{-2}s^{-1}. This gives a relative X-ray to optical flux ratio of ∼320 and a reprocessing efficiency from X-ray flux to optical flux of ∼0.075%. Assuming the companion in EXO 0748-676 is a typical M2V type star, with radius of 0.44 $R_\odot$, and a surface temperature of 6000 K (due to irradiation heating, Hynes and Jones 2009), one obtains an optical luminosity of 8.1×10^{32} ergs/s, which corresponds to a an optical flux of 2.68×10^{-13} erg cm^{-2}s^{-1} from the companion, assuming a source distance of 5 kpc.

In EXO 0748-676, the optical eclipses are not total, and are also broader compared to the X-ray eclipses. This indicates that a fraction of the optical photons are emitted from a region, that is centered around the X-ray source, but larger, perhaps with a size comparable to the size of the companion star. A non-zero optical intensity during the eclipse indicates a considerable emission from a broader region, perhaps the outer disc with a small contribution from the companion. Although the broad optical eclipses do coincide with the X-ray eclipses, the optical dips (narrow and broad) are not particularly coincident with the soft X-ray dips. The CCFs display variable positive soft X-ray to optical as well as hard X-ray to optical delays at timescales of a few 1000 s for almost all the orbital cycles. The cross-correlation coefficients are minimal in all the 7 observations. Also, the CCFs are variable from orbit-to-orbit in delays and strength. The lack of correlation at reprocessing timescales is expected and is consistent with the correlation analysis results. However, the observed weak correlation, evident from the repeating patterns of the CCF, that exists at sub-orbital timescales of a few 1000s of seconds, is probably associated to the orbital period. This timescale is different than the dynamic or viscous timescales in the binary and can possibly arise due to variable outer accretion disc structures, discussed in section 4.1.

Since the OM data from the XMM-Newton observation in 2005 (Obs-ID 0212480501) was of a poor statistical quality, it was not possible to carry out a comparative study of the X-ray optical co-variability during the hard spectral state (2003) with the soft spectral state (2005).

4.4.3 Large optical variability

The input for the reprocessing phenomena, the X-rays from the compact star, is likely to be stable since the mass accretion rate and luminosity of the source is fairly constant during the entire duration of all the 7 XMM-Newton observations (Boirin et al., 2007). The optical emission from a stable accretion disc with fairly constant mass accretion rate must exhibit a smooth orbital modulation and is unexpected to show modulations as observed in Figure 4.3. The soft X-ray variability is due to absorption by structures in the accretion disc. However, optical emission from the outer disc will have variability that is different from the X-rays. Vertical accretion disc structures like the ones addressed in section 3.1.4.2 are capable of producing orbital optical intensity variation both due to changing visibility of the structures themselves or the visibility of their X-ray reprocessing faces.

4.4.4 Mean optical intensity and optical states

The optical counterpart of EXO 0748-676, UY Vol, is known to exhibit high and low intensity states similar to those defined for the X-ray (Motch et al., 1989b). The high state corresponds to a high mean optical intensity which also exhibits a broad minima at the phases 0.6-1.2. The low state, on the other hand exhibits a lower mean optical intensity with the broad optical dip disappearing and the sinusoidal shape flattening out (Thomas et al., 1993). In the current dataset, the optical light curves of Obs-IDs 0160760101, 0160760201, 0160760301 and 0160760401 show a broad minima, with some orbital cycles exhibiting peaks; whereas, the orbital profiles observed in Obs-IDs 0160760601, 0160760801 and 0160761301 is different: flattened sinusoids without any peaks. Within the current set of 7 observations, all having similar orbital averaged optical intensity, the shape of the optical modulation varied between what was earlier known to be associated with the optical bright and low intensity states. This could indicate that the optical orbital intensity profiles are not intrinsically related to the mean optical intensity.

4.5 Summary and Conclusions

As a part of exploring the accretion disc dynamics in the high inclination eclipsing LMXB EXO 0748-676, we have carried out detailed X-ray and simultaneous optical analysis using XMM-Newton observations. From simultaneous X-ray and optical observations of EXO 0748-676 in the hard spectral state, it can be seen that there

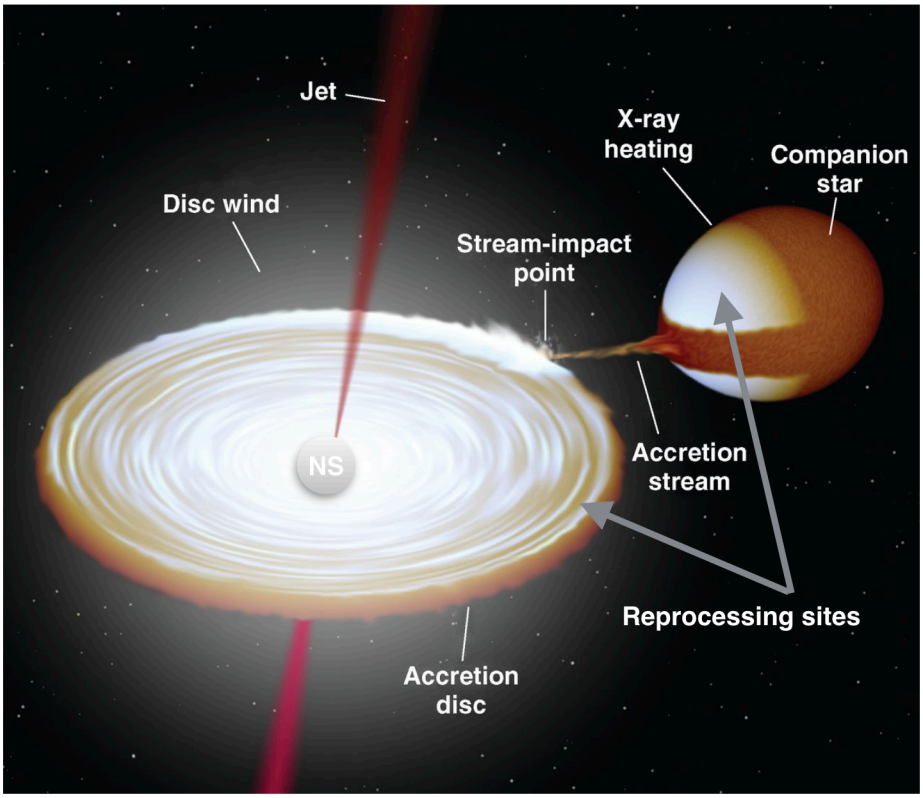

Fig. 4.25 A cartoon illustrating the expected geometry of the X-ray binary with the different components. The reprocessing sites for the LMXB EXO 0748-676, namely, the accretion disc and the inner face of the companion star are indicated. Credit: Robert Hynes, Binary simulations.

exists a weak correlation at a few 1000 s timescales. There exist vertical structures in the outer accretion disc that evolve at binary orbital timescales of a few hours. Large optical variability between successive orbits could be the result of reprocessing occurring at these evolving disc structures. These structures, which act as reprocessing sites, could be the result of irradiation effects and/or warping (as illustrated in Figure 4.25). Modelling these effects would require more sophisticated understanding of an irradiated accretion disc and warps, both of which are still at a very nascent stage. More simultaneous X-ray and optical data would improve statistics and help analyse these scenarios better. We also have studied the X-ray and optical burst profiles and have quantified the mean delays and smearing factors observed for each of the 63 thermonuclear bursts. The delays obtained are consistent with the light travel times within the binary system. Preliminary simulations of the expected reprocessed optical burst as well as non-burst optical light curve profiles have been carried out.

Chapter 5

Spectral and Timing studies of the LMXB dipper XTE J1710-281

This chapter is adapted from the earlier submitted version of the paper 'Spectral and timing studies of the high inclination dipper XTE J1710-281' by Raman et al. (2017) to MNRAS; the updated version, 'Observation of variable pre-eclipse dips and disk winds in the eclipsing LMXB XTE J1710-281' has now been accepted for publication in MNRAS.

5.1 Introduction

Accreting Low Mass X-ray Binary (LMXB) systems contain a compact object in a binary configuration with a mass-donating low-mass companion star (Lewin and Clark, 1980). A small subset of the total LMXB population that have high inclinations (i$\sim$70-90°) are the dipping and eclipsing sources (Díaz Trigo et al., 2006). Out of the thirteen LMXB dipping sources (dippers from now) that host a neutron star, six systems show complete eclipses (D'Aì et al., 2014). These systems present a variety of spectro-temporal signatures that allow efficient means of probing the accretion disc, its atmosphere and possible structures on it.

Absorbers responsible for producing the intensity dips are understood to be vertical structures present on the outer accretion disc, with asymmetric azimuthal distribution (White and Swank, 1982b; Boirin et al., 2007). Spectroscopic studies in a set of six dippers (EXO 0748-676, 4U 1254-690, 4U 1624-490, MXB 1659-298, 4U 1746-371 and 4U 1915-05) revealed that the spectral continuum during dips could be well described by simple ionized absorber models (Díaz Trigo et al., 2006).

High inclination systems have also been found to exhibit X-ray disc winds that are an important aspect in understanding the process of accretion/ejection, particularly in LMXBs (Miller et al., 2011, 2015; Ponti et al., 2014). Disc-wind outflow signatures have been detected in the form of high ionization Fe absorption lines with large outflow velocities, in the soft spectral state (Neilsen and Lee, 2009; Ponti et al., 2012). The fact that these absorption lines are seen only in high inclination sources indicate that these absorbers have an equatorial distribution. In both black hole as well as neutron star binaries, equatorial disc-wind outflow signatures have been detected only in their soft spectral state (Miller et al., 2011; Neilsen and Lee, 2009; Ponti et al., 2012, 2014). Díaz Trigo et al. (2006) detected highly ionized Fe absorption lines (Fe XXV and Fe XXVI) in six high inclination dippers. Our current study focuses on one such high inclination LMXB, XTE J1710-281, with an aim to bring out important timing and spectral features in the source.

XTE J1710-281 is a transient eclipsing LMXB that was discovered in 1998 serendipitously, with *RXTE* (Markwardt et al., 1998). It is a highly inclined binary system viewed edge on with an inclination angle i $\sim$75°-80° (Younes et al., 2009). It shows X-ray eclipses every 3.28 hours with an average eclipse duration of $\sim$420 s (Jain and Paul, 2011). This LMXB also exhibits X-ray intensity dips. The discovery of Type 1 thermonuclear bursts indicated that the compact object is a neutron star and the distance to the source was constrained using the Type-1 bursts to be between 15-20 kpc (Markwardt et al., 2001). The spectrum measured with RXTE PCA was consistent with a thermal bremsstrahlung (kT = 14$\pm$3 keV) or a power law (photon index 1.8$\pm$0.1), with an absorption column density $N_H < 2\times10^{22}$ cm^{-2} (Markwardt et al., 1998). Younes et al. (2009) reported spectral changes during dipping intervals using *XMM-Newton* observations in 2004 and compared the partial neutral absorber and ionized absorber models. Absorption lines due to ionized species like Fe XXV and Fe XXVI observed in other dippers (for example EXO 0748-676: Ponti et al. 2014, 4U 1323-62 and 4U 1624-490: Boirin et al. 2007) were not detected in their 2004 *XMM-Newton* observation.

XTE J1710-281 resembles a well studied eclipsing source, EXO 0748-676 in many ways. Both are high inclination LMXBs that show frequent thermonuclear X-ray bursts and intensity dips in their light curves. EXO 0748-676 has an orbital period of 3.82 hr and displays pre-eclipse dips that vary significantly within short timescales (Parmar et al., 1986; Raman and Paul, 2017). Jain and Paul (2011) carried out extensive eclipse timing studies for XTE J1710-281 and reported two orbital period glitches which are

similar to the period glitches observed in EXO 0748-676 (Wolff et al., 2009).

In this work we have analyzed archival data from *Chandra* and *Suzaku* for XTE J1710-281 to bring out the accretion disc dynamics in the context of the dip evolution and continuum spectral changes from persistent to dipping intervals. We then compare it with the eclipsing LMXBs, EXO 0748-676 and AX J1745.6-2901.

5.2 Observations and data reduction

We have analyzed archival X-ray observations of XTE J1710-281 from *Chandra* and *Suzaku* observatories, a summary of which, is presented in Table 5.1.

5.2.1 *Chandra*

XTE J1710-281 was observed with the Chandra X-ray Observatory (CXO, Weisskopf et al. 2002) on the 23rd of July and on the 7th of August, 2011. The archival data for each Obs-ID (12468 and 12469) had an exposure of ∼75 ks with the ACIS-S detector using the High Energy Transmission Grating Spectrometer (HETGS; Canizares et al. 2000). The data was processed using the `CIAO` software version 4.7. A level 2 dataset was produced using the *chandra_repro* script. The ACIS light curve and spectra were extracted within a source region of 4 arc seconds. The pile-up for *Chandra* observations were computed using the web PIMMS version 4.8 [1]. The ACIS-camera suffered from heavy photon pile-up (∼ 65%) for the zeroth order and so the zeroth order data are not used for further analysis for these two Obs-IDs. The HETG first order grating spectra, arf and rmf were produced during the level 2 processing using the *chandra_repro* script. The *combine_grating_spectra* tool was used to produce a co-added grating spectrum for the plus and minus first order spectra of the HETG and METG arms. The corresponding arf and rmf files were averaged. The spectra were rebinned to obtain a minimum of 50 counts per bin.

5.2.2 *Suzaku*

The X-ray Imaging Spectrometer (XIS) aboard *Suzaku* covers the energy range of 0.2-12 keV (Koyama et al., 2007). The three operational XIS detectors: XIS0, XIS1 and XIS2 have been used for this current analysis. The *Suzaku* Obs-ID 404068010 had a useful exposure of ∼75 kilo-seconds. The XIS detectors were operated in the standard data

[1] http://cxc.harvard.edu/toolkit/pimms.jsp

Observatory	Obs-ID	Instrument	Date of Observation (MJD)	Exposure (ks)	No. of type-1 X-ray bursts
Chandra	12468	HETG	23-07-2011 (55765)	75.1	7
Chandra	12469	HETG	07-08-2011 (55780)	75.1	5
Suzaku	404068010	XIS	23-03-2010 (55278)	76.1	6

Table 5.1 Table detailing the different observations used in the current analysis.

mode with normal window operation that provided a timing resolution of 8 s. The unfiltered event files were reprocessed with the CALDB version 20160607 and HEAsoft version 6.16. The XIS event files were checked for pile-up using the ftool 'pileest' and were found to be free from photon pile-up (less than 0.01%). The reprocessed event files were used to extract light curves and spectra from a circular region of 240 arc seconds around the source centroid. A circular region of the same size far away from the source centroid was selected for the background. Corresponding response file was generated by using the FTOOLS task *xisresp* using the CALDB mentioned above. In the case of *Suzaku* spectra, the spectra from the front illuminated CCDs (XISs 0 and 3), and the back illuminated CCD (XIS-1) were fit simultaneously in the energy range of 0.6-9 keV keeping the instrument normalizations free. Due to artificial structures in the XIS spectra around the Si and Au edge, the energy range of 1.7-2.3 keV was neglected. The XIS spectra were rebinned to contain 100 counts per bin.

5.3 Timing analysis

5.3.1 Light curve and average orbital profile

Since the ACIS zeroth order light curve was heavily piled up, we extracted HETG first order plus and minus arms light curves. Background subtracted and energy dependent (described in detail in section 3.3) first order light curves between 0.5 to 10 keV for *Chandra* Obs-IDs 12468 and 12469 were extracted with a bin size of 1.74 s and are plotted with a 200 s binning (Figure 5.1 top and middle panels). The light curves display more than 6 orbital cycles with sharp X-ray eclipses. X-ray intensity dips are seen to occur at orbital phases prior to the eclipse. The depth and width of the dips are seen to vary from one orbital cycle to the next, as described in detail in the next subsection. The first order light curves from both the *Chandra* observations also exhibit 7 and 5 type-1 bursts, respectively, as mentioned in Table 5.1.

We also extracted light curve for the *Suzaku* observation in the 0.5-10 keV energy band with a time bin size of 8 s and plotted it with a bin size of 100 seconds (Figure 5.1 bottom panel). The light curve contains large data gaps, with incomplete sampling of persistent, dipping and eclipsing intervals. The light curve shows a total of six thermonuclear X-ray bursts during this observation.

In order to compare the average orbital profile, specially the dip features between the different observations, we folded the light curves with the orbital period of 11812.66 s (Jain and Paul, 2011), at a reference epoch of MJD 55278.29, 55762.79 and 55766.895 for the *Suzaku* observation and *Chandra* Obs-IDs 12468 and 12469, respectively. In order to exclude the thermonuclear bursts, time filters were applied to the light curves. On an average, these time windows were $\sim$ 100 s in duration. The average orbital profile is shown in Figure 5.2 with dips covering the phase range 0.6-0.9. The *Chandra* Obs IDs 12468, 12469 and *Suzaku* light curves show slightly different folded orbital profile features. The duty cycle of a dip is defined as the duration of the dip as a fraction of the total orbital period. The pre-eclipse dips for the *Chandra* Obs-ID 12468 and *Suzaku* have duty cycle of nearly 40%, while for the *Chandra* Obs-ID 12469 it is nearly 30%. Along with the pre-eclipse dips, the *Suzaku* profile shows a bump at around phase 0.3, while the *Chandra* Obs-IDs 12468 and 12469 profiles show a less intense secondary dip at phase $\sim$0.4 (duty cycle 10%).

5.3.2 Orbit to orbit evolution of dips

While investigating the dipping profiles in the *Chandra* observations (Figure 5.3), we see orbit to orbit evolution of dips for the first time in this source. The evolution of the depth and width in each subsequent orbit is clearly visible for both the observations. The pre-eclipse dip is observed to be with and without sub-structures in different orbital cycles. An earlier study of the dips made by Younes et al. (2009) in 2004 using *XMM-Newton* also reported presence of narrow absorption dips in one single orbital cycle alone. For both the observations, the duty cycle of the dips range from about 10% to nearly 50%, possibly indicating variable absorber azimuthal distribution above the disc plane. The depth of the dips vary between 20%-90%, signifying variable absorber column density along our line-of-sight between successive orbital cycles. Unlike the light curves from the *Chandra* observations, the *Suzaku* light curve has data gaps. We cannot therefore investigate the dips in the light curve in successive orbits.

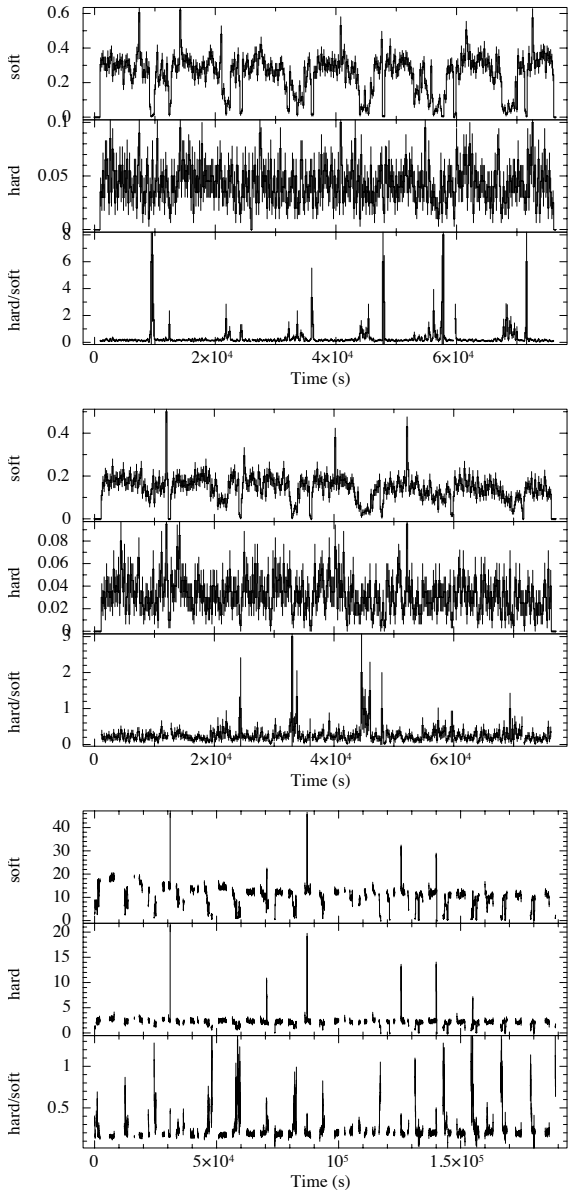

Fig. 5.1 Light curves from the first order HETG *Chandra* Obs-ID 12468 (top), 12469 (middle) with a bin size of 200 s and *Suzaku* (bottom) with a bin size of 100 s are shown. The light curves, extracted in two energy bands, soft (0.5-5 keV) and hard (5-10 keV) are shown along with the hardness ratio in the bottom panel for all the three Obs-IDs. An increase in the hardness ratio is observed during dipping. Type-1 thermonuclear X-ray bursts are also observed in all the light curves.

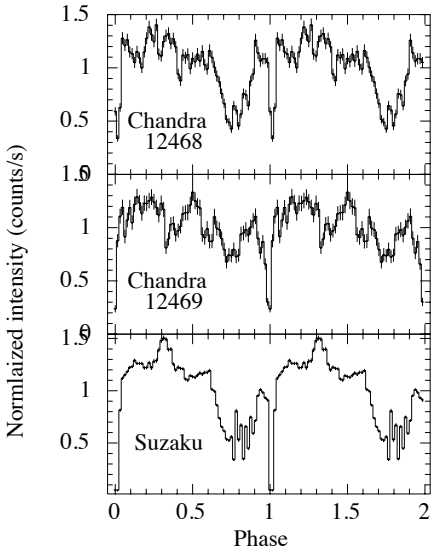

Fig. 5.2 The average orbital profile of the two Chandra observations 12468 (top) and 12469 (middle) folded at 11812.66 s. The bottom panel shows the average *Suzaku* folded pulse profile. All three observations display a clear dip at the orbital phase just before the eclipse.

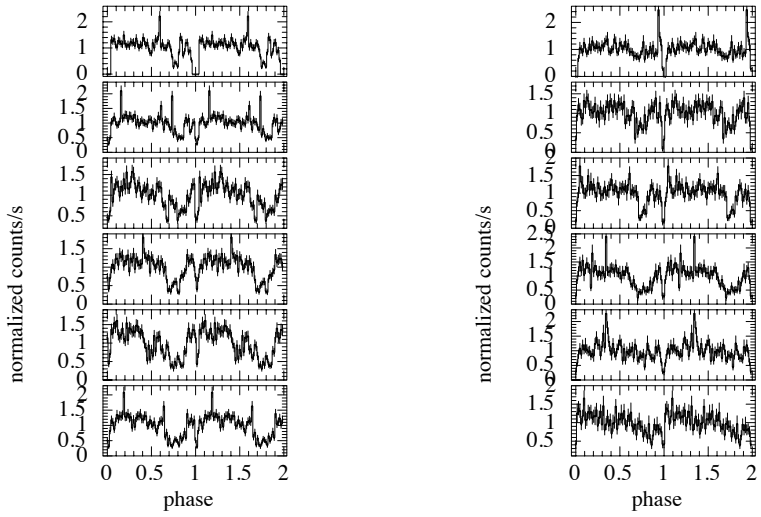

Fig. 5.3 The orbit-to-orbit intensity modulations are shown for the *Chandra* Obs IDs 12468 (left) and 12469 (right) first order light curve. A clear evolution of the dip parameters (depth, width and shape) as a function of time, is observed.

5.3.3 Energy dependence of dips

To investigate the energy dependence of the dips, we extracted background subtracted light curves in two energy bands: 0.5-5 keV and 5-10 keV for all the observations. Figure 5.1 shows the energy dependent intensity variations in the light curves for the three observations. The soft X-ray light curve shows more prominent dips as compared to the hard-X-ray band. As a result, the hardness ratio increases during the X-ray dips, with the deeper troughs showing an increased hardness ratio compared to the shallower one. Although the *Suzaku* observation has periodic large data gaps, a periodic increase in the hardness ratio with interval same as the orbital period indicate it to be due to the dips in the same orbital phase range as the *Chandra* light curves. The increase in hardness ratio during dipping intervals has been observed before by Younes et al. (2009) using *XMM-Newton* observations for this source, and for other dipping sources like 4U 1254-690, 4U 1323-62, 4U 2127+11 etc. (Ioannou et al., 2002; Boirin et al., 2007; Díaz Trigo et al., 2009).

5.4 Spectral Analysis

5.4.1 Time-averaged spectroscopy

We performed spectroscopy of XTE 1710-281 averaged over the entire stretch of the observations for the *Chandra* and *Suzaku* data. Spectral fitting was performed using *XSPEC* (Arnaud, 1996) version 12.8.1. The photo-electric cross-sections of Wilms et al. (2000) have been used to model the line-of-sight absorption by neutral gas with solar abundances (the '*TBabs*' *XSPEC* model). The cross section for X-ray absorption by the ISM is computed as the sum of the cross sections for X-ray absorption due to the gas-phase ISM, the grain-phase ISM, and the molecules in the ISM. At first the spectra were fitted with a powerlaw with a single absorption component accounting for the foreground absorption which includes the line of sight interstellar absorption as well as absorption local to the source. The fits however proved to be unsatisfactory with large systematic residuals left after the fitting, and high values of χ^2 (Reduced χ^2 of 0.66 for 334 d.o.f for Obs-ID 12468 and 1.22 for 563 d.o.f for Obs-ID 12469). Addition of another absorption component in the form of a partial covering absorber representing the local structures in the accretion disc (causing the pre-eclipse dips) provided a better fit (Reduced χ^2 of 0.63 for 331 d.o.f for Obs-ID 12468 and 1.11 for 560 d.o.f for Obs-ID 12469). We tried to fit both a partial covering neutral absorber (*XSPEC* model '*pcfabs*') and partial covering ionized absorber (*XSPEC* model '*zxipcf*',

Reeves et al. 2008) to the spectrum to account for this effect. The partial covering neutral and ionized absorber models yielded similar reduced χ^2 (reduced χ^2 of 0.69, 0.66 for the two models respectively for Obs-ID 12468 with 332 d.o.f. and reduced χ^2 of 1.22, 1.11 respectively for Obs-ID 12469 with 560 d.o.f.) However, the partially ionized partial absorber model proved to be a better fit as compared to the partial covering neutral absorber, in terms of the absence of systematic structures and edges in the residuals and was hence used as the best-fit model for all our fits. No further change in the continuum components were made and the same model 'zxipcf' was used for all the three observations. Table 5.2 shows the best fit parameters along with the fluxes measured. Figure 5.4 shows the best-fit average HETG first order spectra for Chandra Obs IDs 12468 and 12469, and simultaneous XIS0, XIS1 and XIS3 *Suzaku* spectra. The derived absorbed fluxes (0.5-8 keV) for the *Chandra* (Obs ID 12468, 12469) and the *Suzaku* observation in order are $4.25\pm0.2\times10^{-11}$, $7.94\pm0.1\times10^{-11}$ and $4.50\pm0.07\times10^{-11}$ ergs s^{-1} cm^2. The *Chandra* Obs-ID 12469 shows a steeper power law index and larger flux compared to the other two observations.

In addition to the modeling of the continuum, we detected several spectral lines in the *Suzaku* spectrum. The first is a broad emission feature at $\sim$0.72 keV of equivalent width 82.2$\pm$7.0 eV. This is probably a complex due to unresolved Fe L shell lines. An additional weak absorption line is detected, with a significance of 3.4σ at 6.6$\pm$0.03 keV, which is at the same energy as the atomic transitions corresponding to one of the He-like Fe XXV triplet absorption line. The line width was fixed to a value of 0.01 keV. The optical depth (line-depth/$\sqrt{2\pi}$ line-width) at the Gaussian absorption line center is calculated to be $\sim$0.8. Introducing these lines moderately improved the reduced χ^2 to 1.03 with 2230 d.o.f, from an initial reduced χ^2 value of 1.1 for 2236 d.o.f without the gaussian emission line at 0.72 keV (F statistic value = 25.2589 and probability 3.75155e-29) and an initial reduced χ^2 value of 1.04 for 2235 d.o.f without the gaussian absorption line at 6.6 keV (F statistic value = 4.3301 and probability 0.000634495). Although we do not detect similar features in the *Chandra* HETG spectrum, we cannot rule out its presence in the corresponding spectra. This is because, for the count rate of XTE J1710-281, these lines would be below the detection threshold of HETG considering its lower effective area w.r.t the XIS. However, in order to derive upper limits on the presence of the 6.6 keV line in the time-averaged *Chandra* spectra, a gaussian absorption feature (the 'gabs' model in XSPEC) was introduced at 6.6 keV. We fixed the line energy and width to the values obtained in the Suzaku spectra and

Model Parameter	Model	*Chandra* Obs-ID 12468	*Chandra* Obs-ID 12469	*Suzaku*
nH^{fore} ($10^{22}cm^{-2}$)	**TBabs**	0.55 ± 0.1	0.72 ± 0.1	0.48 ± 0.02
nH ($10^{22}cm^{-2}$)	**zxipcf**	$37.3^{-12.54}_{+11.78}$	$45.3^{-10.4}_{+9.2}$	$42.47^{-6.2}_{+6.9}$
log(ξ)	**zxipcf**	$2.25\ ^{-0.16}_{+0.26}$	3.03 ± 0.1	2.01 ± 0.01
Cov. f	**zxipcf**	0.64 ± 0.1	0.56 ± 0.1	0.4 ± 0.04
Power law index	**po**	2.1 ± 0.1	2.45 ± 0.1	1.95 ± 0.04
E_{gabs} (keV)	**gabs**			$6.60\ ^{-0.04}_{+0.02}$
σ (eV)	**gabs**			0.01 (fixed)
depth	**gabs**			$0.04\ ^{-0.02}_{+0.04}$
E_{gaus} (keV)	**gaus**			0.72 ± 0.01
EW (eV)	**gaus**			82.2 ± 7.0
red. χ^2		0.66 for 332 d.o.f	1.11 for 560 d.o.f.	1.03 for 2231 d.o.f
Flux ($ergs/cm^2/s$)[a]		$4.25\pm0.2 \times10^{-11}$	$7.94\pm0.1 \times10^{-11}$	$4.10\pm0.07 \times10^{-11}$

Table 5.2 Best fit spectral parameters for time-averaged *Chandra* (Obs-ID 12468 and 12469) HETG spectra and XIS0, XIS1 and XIS3 *Suzaku* spectra fitted simultaneously. The errors are quoted at 90% confidence interval.

[a] Flux is measured from 0.5-8 keV

obtain upper-limits to the line depth as 2.4×10^{-5} and 1.00×10^{-4} for Obs ID 12468 and 12469, respectively, as compared to the line depth of 0.02 ± 0.01 detected with *Suzaku* .

5.4.2 Intensity resolved spectroscopy

In order to probe the changes in the spectrum from the persistent and dipping intervals, we carried out an intensity resolved spectral analysis of the *Chandra* and *Suzaku* observations. In order to perform this exercise, we first excluded the intervals corresponding to thermonuclear bursts and eclipses. We then defined persistent and dipping intervals based on the count rate from the light curves of the corresponding observations. For the *Chandra* observations the persistent emission is seen to have an average count rate of 0.25 counts/s (Figure 5.1). Time intervals that had intensities below 75% of the average persistent count rate were considered as dipping intervals. We then extracted spectra corresponding to those intervals. The *Chandra* intensity resolved spectra were grouped to contain 50 counts per energy bin.

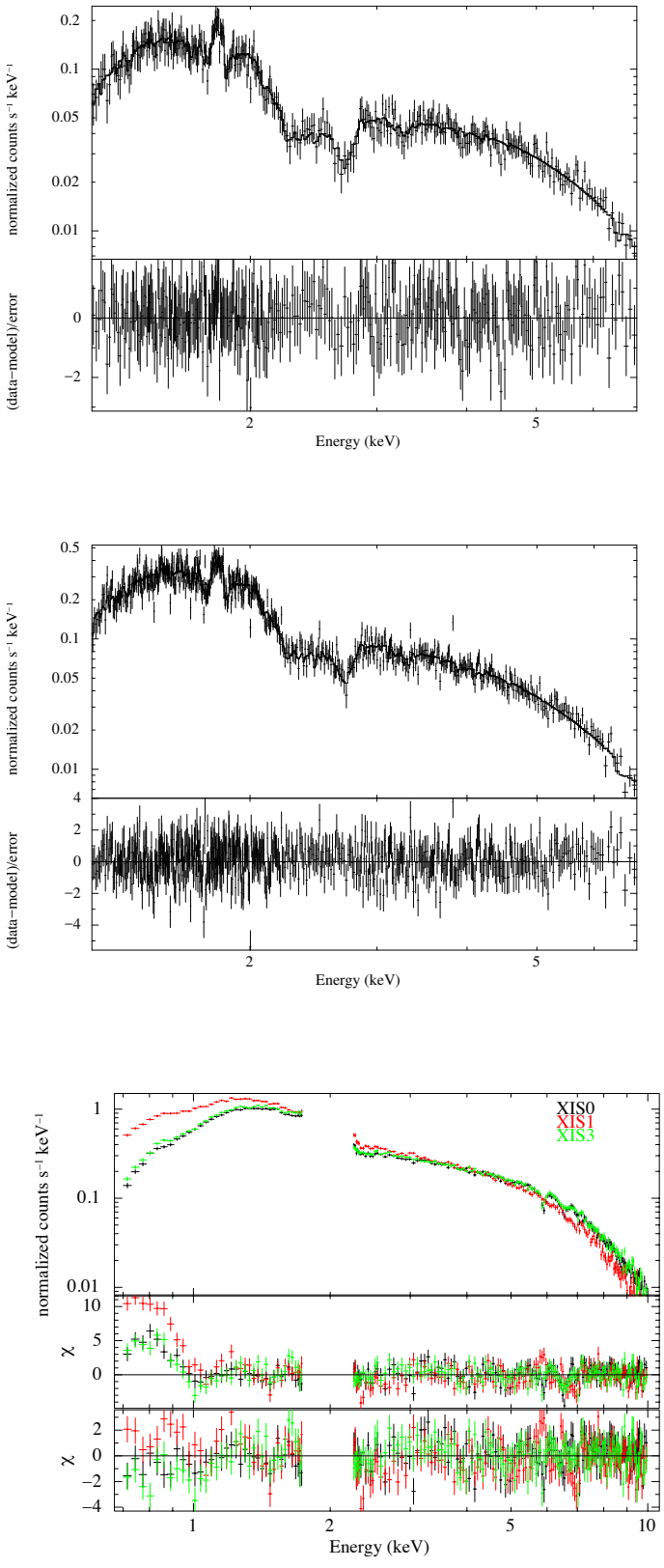

Fig. 5.4 The time-averaged best fit spectra for *Chandra* Obs-ID 12468 (top), 12469 (middle) and *Suzaku* (bottom) are shown. The *Suzaku* spectrum shows residuals at 0.72 keV and 6.6 keV which are indicated.

Since the *Suzaku* light curve contained incompletely sampled dips, it was not possible to identify dipping time intervals from the light curve. Therefore a count rate cut of 75% of the average persistent count rate (about 2 counts/s), similar to what was used for the *Chandra* analysis, was adopted to identify the dipping intervals. The corresponding spectra for the persistent and dipping intervals were extracted. A different grouping scheme was adopted for the persistent (minimum of 120 counts per bin) and dipping (minimum of 100 counts per bin) intervals, as compared to the time-averaged *Suzaku* spectrum. The same background and response files that were used to fit the persistent spectra were taken for the fits.

We consider the cause of the dipping activity to be absorption due to the passage of the vertical structures obscuring our view to the source (White and Swank, 1982b; Díaz Trigo et al., 2006). In this case we may assume that the underlying continuum spectrum does not change during the duration of the observation, and the spectral changes during the dipping intervals are solely due to the passage of this absorbing material along our line of sight. In order to demonstrate this we fit the persistent and the dipping spectra simultaneously linking the parameters of the continuum emission, *i.e.* the powerlaw component. The absorption components are left free. We fix the energy and width of the emission lines in the case of *Suzaku* spectrum to the corresponding values obtained in the average spectra, due to statistical limitations.

In the case of the *Chandra* Obs-ID 12468 and 12469, the line-of-sight neutral hydrogen column density was fixed to the time-average values. This was because the errors obtained on this parameter, if left free for each component, was very large, and the value was consistent with that obtained from the average spectrum. While fitting the intensity resolved spectra, the power law index was tied between the persistent and dipping intervals and the ionized absorber zxipcf model parameters have been left free to vary. There appears to be a significant increase in the ionized absorber column density and a decrease in the ionization state from the persistent to dipping spectra for both *Chandra* Obs-IDs. Significant residuals were still present, that prompted us to include an edge model into the fit. An edge is detected at 2.75±0.05 keV (F statistic value = 14.3733 and probability 9.01986e-11), possibly indicating the presence of S XVI.

In the intensity resolved *Suzaku* spectra the neutral hydrogen column density is seen to marginally decrease from 0.22×10^{22} cm^{-2} to 0.17×10^{22} cm^{-2} from the persistent to dip spectra. However, the absorption column density of the partially ionized absorber

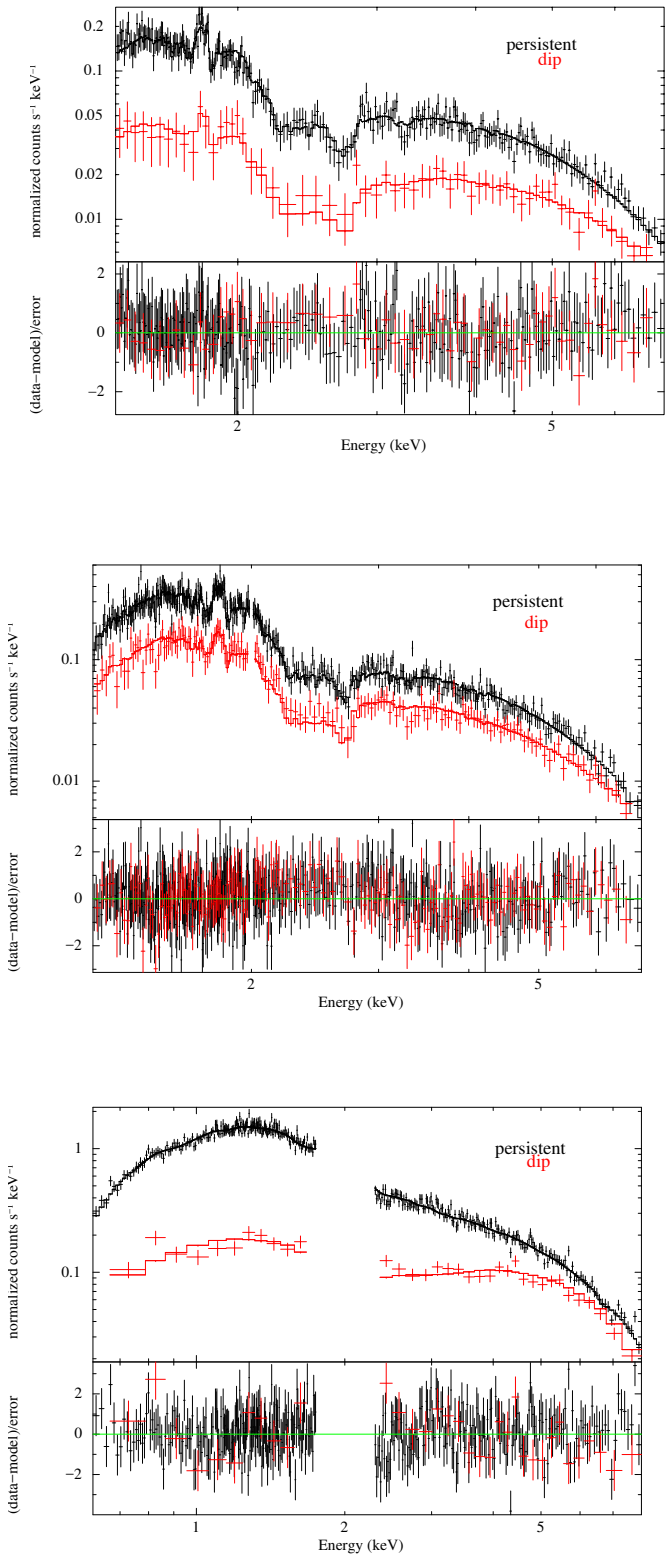

Fig. 5.5 Intensity resolved spectra for the persistent and dip epochs are fit simultaneously for *Chandra* Obs-ID 12468 (top left), *Chandra* Obs-ID 12469 (top right) and *Suzaku* (bottom) observations. The best fit spectrum for only the XIS0 is shown for the *Suzaku* observation.

Parameter	Model	*Chandra* Obs-ID 12468		*Chandra* Obs-ID 12469		*Suzaku*	
		Persistent	Dip	Persistent	Dip	Persistent	Dip
nH^{fore} ($10^{22}cm^{-2}$)	**TBabs**	0.54[a] (fixed)		0.72[a] (fixed)		0.22±0.01	0.17±0.07
nH ($10^{22}cm^{-2}$)	**zxipcf**	0.14 (fixed)	$68.3^{+49.6}_{-98.6}$	$11.6^{+18}_{-7.8}$	$65.2^{+34.2}_{-24.9}$	$2.86^{+2.3}_{-1.8}$	$14.9^{+1.8}_{-1.6}$
log(ξ)	**zxipcf**	$2.74^{+2.7}_{-1.4}$	$1.73^{+2.26}_{-1.72}$	$3.4^{+0.52}_{-0.14}$	$1.95^{+0.18}_{-0.71}$	3.38±0.1	1.43±0.2
Cov. f	**zxipcf**	1.0	0.60±0.04	0.64±0.3	0.52±0.03	1.00	0.89±0.01
Power law index	**po**	1.86±0.04		2.58±0.05		1.77±0.02	
E (keV)	**gabs**					6.6[a]	
sigma (eV)	**gabs**					0.01[a]	
depth	**gabs**					0.01[a]	
E (keV)	**gaus**					0.72[a]	
EW (eV)	**gaus**					133.3	148.4
E(keV)	**edge**	2.75±0.05		$2.77^{+0.05}_{-0.01}$			
Max Tau	**edge**	0.33±0.1	0.72±0.3	0.39±0.1	0.56±0.1		
red. χ^2		0.61 for 311 d.o.f		0.83 for 582 d.o.f.		1.12 for 374 d.o.f	

Table 5.3 Best fit spectral parameters for intensity resolved *Chandra* (Obs-ID 12468 and 12469) HETG spectra and simultaneous XIS0, XIS1 and XIS3 *Suzaku* spectra. The errors are quoted at 90% confidence interval.

[a]Frozen to the time-averaged spectral parameter value.

shows an increase by a factor of ∼7 from the persistent to the dip spectrum. The ionization parameter shows a decrease from 3.38±0.1 to 1.43±0.2 from the persistent to the dipping spectra. We fixed the 6.6 keV absorption line parameters, and the 0.72 keV broad emission line parameters to the time-averaged spectral parameter values. The best fit spectra for the intensity resolved *Chandra* and *Suzaku* observations are shown in Figure 5.5, and Table 5.3 shows the best fit spectral parameters.

5.5 Discussion

We have carried out spectro-temporal analysis of the dipping LMXB XTE J1710-281 using archival *Chandra* and *Suzaku* observations. We have observed evolution in the dip strength, duration and shape between successive orbital cycles, indicating evolution of the accretion disc structures in the timescale of hours. We have also detected highly ionized Fe species in the *Suzaku* spectra, which indicate signature of disc winds as observed in other dippers. The dip spectrum in *Chandra* and *Suzaku* observations is found to be best described by a power law component with a spectral index of $\Gamma \sim 2$ with partial covering by a partially ionized absorber.

5.5.1 Evolution of the dips

High inclination LMXB sources exhibit intensity dips, which are usually characterized by increased spectral hardness (Díaz Trigo et al., 2009). These dips have been observed in some total eclipsing sources like EXO 0748-676, XTE J1710-281 and also in some partial eclipsing sources like 4U 2129+12 (Chou, 2014). Recently Galloway et al. (2016) discovered, in the LMXB source Aql X-1, intermittent episodes of dipping, similar to those observed in high inclination binaries. Detailed characterization of dip parameters like the dip orbital phase, width and strength have been performed for many dippers, to extract information of orbital period and also dynamics of the accretion disc structures (Chou, 2014; Chou and Grindlay, 2001; Hu et al., 2008). Since dips are caused by absorption in the accretion disc structure, they are not exactly phase-locked, but they show phase jitters (eg. ±0.05 cycle for 4U 1915-05, Chou and Grindlay 2001). In the case of XTE J1710-281 (Younes et al. 2009 and the current work), on average, the dips are observed pre-dominantly at pre-eclipse orbital phases between the orbital phase range of 0.6-0.9. In the system EXO 0748-676, dips have also been seen at other orbital phases, even just after the eclipse (Raman and Paul, 2017). A very interesting outcome of this current study of dips using Chandra observations is the evolving morphology

from one orbital cycle to the next. The dip depth, width as well as shape (in terms of the number of narrow features present) are observed to vary. Irradiation-induced vertical structures (de Jong et al., 1996; Pringle, 1996), present usually at the outer accretion disc are azimuthally distributed in an asymmetric manner (Hakala et al., 2005). They are responsible for preferentially absorbing the primary X-ray photons at certain orbital epochs as was also observed in EXO 0748-676 (Parmar et al., 1986). The orbit-to-orbit dip profiles as seen in the *Chandra* light curves have different features, some are broad, some deep and some even have narrow features, similar to what was observed by Younes et al. (2009) in the *XMM-Newton* light curve. Nevertheless, the presence of varying dip intensities in successive orbital cycles in *Chandra* indicates not just any structure, but an *evolving* one. Warped discs also present a very physically compelling solution to explain different X-ray modulations in LMXBs (Ogilvie and Dubus, 2001). These warps can develop at various disc-radii and can modulate the X-ray emission at certain orbital epochs. Another possible explanation for varying dip morphology at timescales of hours, could be the variable mass accretion splashes at the stream-impact point on the outer accretion disc (White and Swank, 1982b). At these locations, the disc-extent increases vertically leading to temporary structures that block the primary X-ray photons from reaching the observer.

5.5.2 Detection of ionized species of Fe

The broad 0.72 keV emission line detected in the *Suzaku* spectrum, can be identified with an Fe L blend. It has an equivalent width of 82.2±7.0 eV. Owing to the fact that XTE J1710-281 is a relatively faint source, the *Chandra* spectrum does not have enough photons below 1 keV and was therefore not able to detect a line of similar strength. Line emission in the spectral energy range 0.7-2.0 keV (Buote et al., 1999), associated with the Fe L-shell ions, is understood to be a dominant spectral component arising in coronal plasmas (Liedahl et al., 1995). Only ionized Fe ions (Fe XII and beyond) produce Fe L transitions that fall in the energy range 0.7-2 keV. The dominant ion of the Fe L blend in the 0.72 -0.74 keV range is that of Fe XVII (Buote et al., 1999). In addition, a weaker 6.6 keV absorption feature is also detected in the *Suzaku* spectrum. This line can be possibly associated with one of the He-like Fe XXV triplet line. However, it is only marginally detected with a detection significance corresponding to 3.4 σ. Younes et al. (2009) did not detect, in their 2004 *XMM-Newton* observation, absorption lines due to ionized species like Fe XXV and Fe XXVI, that are commonly observed in other dippers (for example EXO 0748-676: Ponti et al. 2014, 4U 1323-62 and 4U 1624-490: Boirin et al. 2007). However, they have derived upper limits on the

equivalent width of the 6.65 keV absorption line corresponding to the Fe XXV 1s-2p transition, as 114, 50, and 73 eV in the persistent, shallow-dipping, and deep-dipping spectra, respectively.

Such high ionization Fe lines are tracers for equatorial disc winds (Ponti et al., 2014). The lines are suspected to be produced by absorption due to photo-ionized gas (Ponti et al., 2015). The Fe XXV Kα (E = 6.697 keV) and Fe XXVI Kα (E = 6.966 keV), as well as Fe XXV Kβ (E = 7.880 keV) absorption lines have been observed in three other eclipsing sources AX J1745.6-2901 (Hyodo et al., 2009), EXO 0748-676 (Ponti et al., 2014) and IGR J17451-3022 (Bozzo et al., 2016). Hyodo et al. (2009) suggested a disc-corona origin for these lines in the source AX J1745.6-2901, since they were observed at all orbital phases. Other non-eclipsing, high inclination dippers like 4U 1254-690, 4U 1624-490 and MXB 1659-298 also show these features, suggesting an equatorial origin for these photo-ionized absorbing gas (Ponti et al., 2014). In black hole binaries, these absorption features were found to have high outflow velocities and therefore were assumed to be equatorial winds (see Ponti et al. 2012, 2014).

Signatures of S XV and S XVI in the form of an *emission* line have been observed in a few other AGN, SNR systems (For eg. Kaastra et al. 2014; Nobukawa et al. 2008) and also in Cyg X-1 (Feng et al. 2003) and has been an indicator of hot plasmas and wind outflows. We suggest that the S XVI absorption edge at 2.75 keV detected in the intensity resolved *Chandra* spectra could have been produced as a result of a similar scenario. However, statistics on the *Chandra* data are insufficient to constrain the line parameters and investigate its changes from persistent to dipping spectra.

In a recent review, Díaz Trigo and Boirin (2016) show that, from a total of 18 LMXBs exhibiting presence of photo-ionized plasma in the form of absorption lines of Fe XXV and Fe XXVI, 16 systems have highly ionized plasma ($\log(\xi) > 3$). However, there are 4 systems that exhibit *both* high ($\log(\xi) > 3$) and low ($\log(\xi) < 3$) photo-ionization and two systems (MAXI J1305-704 and GX 339-4) that show only low photo-ionization. Results obtained from the *Suzaku* observation in this work, indicate that XTE J1710-281 could be one such system whose photo-ionized plasma has both low and high ionization. Such photo-ionized plasma can be irradiation-induced, or even be the result of thermal or magnetic instabilities, etc.

5.5.3 Nature of the absorber

Various models have been proposed to explain the continuum emission in dippers. In order to particularly describe the comptonized component, a number of single and multi-component continuum power-law models have been previously explored. One set of models (Boirin et al. 2007; Díaz Trigo et al. 2006) incorporate a neutral or ionized absorber partially or completely covering the power law as well as the black-body emission during dips. These models explain the dip spectra in sources like 4U 1323-62, EXO 0748-676 and 4U 1254-690. Another set of models (Parmar et al. 1985a; Bonnet-Bidaud et al. 2001; Oosterbroek et al. 2001; Younes et al. 2009) incorporate two-components. In these models, one fraction of the power law component is partially covered by an ionized or a neutral absorber and the remaining fraction is left uncovered. These models have been invoked to describe the dipping spectra in EXO 0748-676. Finally, the third set of models are the complex-continuum models (Church et al. 1998; Bałucińska-Church et al. 1999). These models require two independent absorbing components, one for the extended comptonized power-law emission and another, for the point-like blackbody emission. Again, these complex models allow for neutral as well as ionized absorbers for the comptonized continuum component. Dippers like 4U 1323-62 were modelled in this manner (Boirin et al., 2007).

In the case of XTE J1710-281, the spectral properties of the dips are well described by an ionized absorber that partially obscures the non-thermal emission and does not require us to invoke other complicated models.

Considering that the ionized absorber is located at the outer accretion disc, we can compute the ratio of thickness d, of a slab of the absorber, with respect to the distance r, between the ionizing source and the absorber. For this, we consider the circularization radius to be the minimum possible value for the accretion disc radius, r, and compute it using equation (4.21) (Frank et al., 1992) for a system with mass ratio, q$\sim$0.3. We obtain $R_{circ} \sim 0.32 R_{\odot}$. Since $\xi = L/n_e r^2$, and $n_e \sim {n_H}^{zxipcf}/d$, we compute the ratio,

$$d/r = \frac{r \times \xi \times {n_H}^{zxipcf}}{L}$$

where, ξ is the ionization parameter, L is the source luminosity, n_e is the electron number density and ${n_H}^{zxipcf}$ is the ionized absorber column density. Assuming a

distance of 15 kpc to the source (Markwardt et al., 2001) and a considering a flux of 7.9×10^{-11} ergs/s/cm^{-2} (Table 5.2), we obtain a source luminosity of 2×10^{36} ergs/s. This gives us a d/r ratio of 0.03 and 0.007 for the persistent and dipping intervals, respectively.

Also, there is strong reason to believe that the absorber responsible for the X-ray intensity dips, also causes the Fe line absorptions as well, mainly because these lines are observed only in high inclination dipping sources. The relative line strengths in these different intensity epochs (persistent and dipping), can allow us to probe the absorber characteristics. For example, lines detected during the dips, correspond to electronic transitions from less ionized species than during the persistent (Younes et al., 2009). However we were unable to compare the line parameters in detail because of the weak line depths and statistical limitations of the dataset.

5.6 Summary and Conclusions

We have studied the eclipsing NS X-ray binary XTE J1710-281 using archival *Chandra* and *Suzaku* observations. Using *Chandra* folded orbital profiles, we detected an evolution of the dip morphology from orbit-to-orbit, indicating accretion disc structures, which seem to evolve in timescales as short as a few hours. The intensity resolved *Chandra* and *Suzaku* continuum spectra are best described using a power-law that is partially absorbed by ionized material. We also detect signatures of accretion disc winds in the *Suzaku* spectra, in the form of He-like Fe XXV triplet absorption line and a 0.72 keV Fe-L blend emission line (as illustrated for clarity in Figure 5.6). There is no clear correlation between the flux, shape of the continuum and presence/absence of lines in these observations. The shape of the continuum is consistent between the different observations: the case of the *XMM-Newton* observation (Younes et al., 2009), and also for the case of *Chandra* and *Suzaku* observations (present work). Lines are detected only in *Suzaku* spectrum, but we cannot rule out their presence in the *Chandra* observation (as we mention) and in the *XMM-Newton* (as Younes et al. 2009 mention). Future observations of this object will help understand the distribution of ionized matter on the accretion disc and disc structure evolution scenarios better.

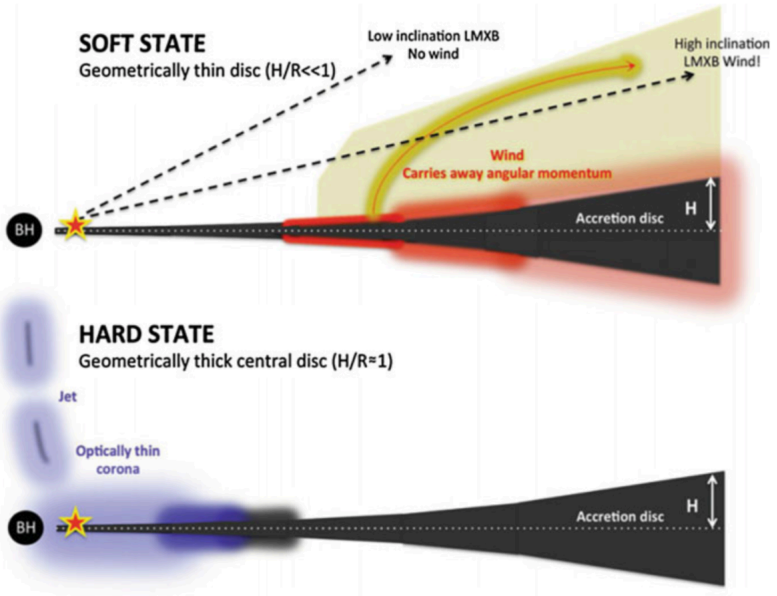

Fig. 5.6 A cartoon illustrating the expected geometry of the disc and outflows in high inclination LMXBs, like XTE J1710-281, in the soft and hard states. Credit: Ponti et al. (2012).

Chapter 6

Summary and future prospects

"There is nothing more deceptive than an obvious fact" - Arthur Conan Doyle

6.1 Summary and context of this thesis work

As part of this thesis work X-ray reprocessing studies have been carried out on three specific LMXB targets. Several interesting aspects of X-ray and optical emission from the different binary components like the accretion disc and the companion star have been observed.

The ultra-compact X-ray pulsar 4U 1626-67, known for its unique torque reversal history, was observed in the optical using the SALT observatory on two occasions. During both the observations, which were carried out during this pulsar's current spin up phase (2014 and 2016), 4U 1626-67 displayed signatures of accretion disc warps at different accretion disc radii in the form of optical side-bands, milli-hertz QPOs and drifting optical pulses. Dynamic power spectra were constructed to evaluate the varying amplitudes of the 7.67 s pulse peak, its harmonics and side-bands. The orbital period for this low inclination object, previously measured using the optical sideband, was confirmed with our observations to be 42 minutes. A unique side-band at 7.65 s was also observed and is possibly another manifestation of orbital modulation of the pulse period at a specific accretion disc radius that could arise due to disc warping.

Multi-wavelength studies of X-ray binaries have proven to be invaluable in extracting crucial information about emission processes. In particular, since regions close to the compact object emit X-rays that go on to heat up nearby regions, producing lower-

wavelength optical/UV photons, X-ray optical co-variability studies come as useful diagnostic handles. Such correlation studies have been carried out on the eclipsing binary EXO 0748-676. In particular, this object presents a favorable inclination that allows the observer to view the accretion disc, structures and periodic eclipses and intensity dips. The results of this work brings out the fact that there possibly exist vertical structures in the outer accretion disc that evolve within timescales of as short as a few hours. Large optical variability between successive orbits could be the result of reprocessing occurring at these evolving disc structures. These structures could be the result of irradiation effects and/or warping.

The high inclination LMXB XTE J1710-281 is a poorly studied object that exhibits orbital period glitches, thermonuclear bursts, dips and eclipses and is very similar to EXO 0748-676. This prompted the study of its spectral and timing characteristics using archival Chandra and Suzaku data. An evolution of dip morphology from orbit-to-orbit in the folded Chandra profile, was observed, indicating accretion disc structures, which seem to evolve in timescales as short as a few hours. The origin of the absorbers responsible for the evolving dips could be disc warps, outer accretion disc stream-impact splashes or irradiation-induced vertical structures. The intensity resolved Chandra and Suzaku continuum spectra could be best described using a power-law that is partially absorbed by ionized material. Results of the Suzaku spectral analysis also revealed the presence of highly ionized Fe species in the form of a broad 0.72 keV Fe L-alpha emission line and also an Helium-like triplet Fe XXV absorption line at 6.6 keV, which are understood to be signatures of accretion disc wind, adding XTE J1710-281 to the sample of disc wind emitting NS systems.

Accreting LMXBs, particularly like those studied in this thesis, that present variability due to accretion disc warping, hold tremendous scope for future studies. In order to map and characterize accretion disc-magnetoshperic interactions, disc structures and instability conditions that would trigger warping and other very less-understood effects, it is crucial to construct a sufficiently exhaustive observational database of sources, and examine them in detail. This thesis work is a small effort towards achieving this goal.

6.2 On-going and Future work

6.2.1 Inadequacies of the reprocessing model

Correlated optical/X-ray studies have been carried out in the past to understand a range of emission mechanisms originating all the way from near the compact object through the inner accretion disc and extending well into the outer accretion disc (van Paradijs and McClintock, 1994). The disc spectrum is a multi-color composite of X-rays and UV/optical and IR. Since emission in each of these wave-bands exhibit various timescales of variabilities, it has become imperative to examine such processes simultaneously in all these wavebands and bring out correlations, if any.

Since in disc accreting systems, optical photons are primarily assumed to be originating due to the reprocessing of X-ray photons, positive lags (of the order of a few seconds to a few 10s of seconds, depending on the location of the reprocessing region) are expected in the X-ray/optical cross-correlation studies. Such has been the case for most objects, until recently, where a number of black hole binaries (like GS 1354-64, etc.) and even a couple of NS binaries (like Sco X-1 and Cyg X-2, Durant et al. 2011) have shown anti-correlation between the X-ray and optical. These correlations/anti-correlations seem to be dependent on the spectral state of the sources. Some sources are also observed to exhibit what is known as a "pre-cognition dip" or an anti-correlation dip prior to the delayed positive correlation peak in the CCF. These observations demand for a far more comprehensive model other than reprocessing. The regimes within which the reprocessing model can be invoked need to be be further explored. Especially, in specific cases where reprocessing is valid, like type-1 thermonuclear bursts, flares, etc., further work can be carried out in terms of phase-resolved echo-tomography or through kinematically resolved emission line echo-mapping. For other cases where the reprocessing model is inadequate, new models such as the magnetic reservoir model (Malzac et al., 2004), the 'thermal Comptonization of synchrotron radiation in the ADC' model (Merloni et al., 2000), the 'electron-cyclotron emission' model (Fabian et al., 1982), etc. provide alternative perspectives to the various observed correlations and anti-correlations. Detections of QPOs, simultaneously in X-rays and optical assist in validating some of these models. The currently operating multi-wavelength observatory, Astrosat, can act as an excellent probe in this domain.

6.2.2 Optical light curve modelling in X-ray binaries

A number of tools currently exist that allows the user to simulate the reprocessed signal in an X-ray binary system. One such program, known as the X-ray binary code[1], is currently being explored in order to characterize the observed non-burst orbital modulations in EXO 0748-676. The program models an X-ray binary system using ray-tracing algorithm for a specified set of binary parameters and generates a model optical light curve (Bayless et al., 2010). Synthesizing model light curves are useful for studying the disc structures like coronae, rims, etc. They are also useful for constraining certain binary parameters (for example, see Bayless et al. 2010).

6.2.3 Accreting neutron stars as sources of GW waves

Pulsars, non-pulsating neutron stars in supernovae remnants and even binary neutron stars are promising sources of continuous gravitational waves from ground-based GW detectors (Aasi et al., 2014). Among these objects, accretion powered NS X-ray binaries are being continuously monitored by existing GW detectors like Virgo and LIGO. Particularly, systems with precisely measured orbital and spin parameters, along with high mass accretion rates and rapid spin rates are ideal candidates for potential GW detection. This list consists of accreting millisecond pulsars, burst oscillation sources and kilo-hertz QPO sources, all of which provide some means of measuring the NS spin frequency. However, uncertainties in the measurements are still large since it requires assuming a wide range of spin and orbital parameters. Precisely constraining these parameters requires rigorous X-ray archival data searches as well as new X-ray satellite (like for eg. Astrosat) observations.

NS frequencies have been observed to be much less than the break-up limit of 1 kHz (Lattimer and Prakash, 2007). Current surveys are still unable to identify rapid rotators, making it appear that there could be some breaking mechanism that prevents accreting neutron stars from reaching the limit. One model suggests that the accretion torques get balanced by magnetopshere-disc interactions, while another model predicts loss of angular momentum via emission of gravitational radiation. Increasing the sample of rapid rotators using Astrosat will help constrain these models better and will help GW detectors to pick and pursue the right candidates for observations.

[1] Details of the X-ray binary code can be found in: http://www.as.utexas.edu/ elr/Robinson/XRbinary.pdf

References

J. Aasi, B. P. Abbott, R. Abbott, T. Abbott, M. R. Abernathy, T. Accadia, F. Acernese, K. Ackley, C. Adams, T. Adams, and et al. First all-sky search for continuous gravitational waves from unknown sources in binary systems. Phys. Rev. D, 90(6): 062010, September 2014. doi: 10.1103/PhysRevD.90.062010.

M. A. Alpar and J. Shaham. Is GX5 - 1 a millisecond pulsar? Nature, 316:239–241, July 1985. doi: 10.1038/316239a0.

M. A. Alpar, A. F. Cheng, M. A. Ruderman, and J. Shaham. A new class of radio pulsars. Nature, 300:728–730, December 1982. doi: 10.1038/300728a0.

K. A. Arnaud. XSPEC: The First Ten Years. In G. H. Jacoby and J. Barnes, editors, *Astronomical Data Analysis Software and Systems V*, volume 101 of *Astronomical Society of the Pacific Conference Series*, page 17, 1996.

M. Bałucińska-Church, M. J. Church, T. Oosterbroek, A. Segreto, R. Morley, and A. N. Parmar. An X-ray study of the dipping low mass X-ray binary XV 1323-619. A&A, 349:495–504, September 1999.

A. J. Bayless, E. L. Robinson, R. I. Hynes, T. A. Ashcraft, and M. E. Cornell. The Structure of the Accretion Disk in the Accretion Disk Corona X-ray Binary 4U 1822-371 at Optical and Ultraviolet Wavelengths. ApJ, 709:251–262, January 2010. doi: 10.1088/0004-637X/709/1/251.

P. A. Becker and M. T. Wolff. Thermal and Bulk Comptonization in Accretion-powered X-Ray Pulsars. ApJ, 654:435–457, January 2007. doi: 10.1086/509108.

A. Beri, C. Jain, B. Paul, and H. Raichur. Torque reversals and pulse profile of the pulsar 4U 1626-67. MNRAS, 439:1940–1947, April 2014. doi: 10.1093/mnras/stu087.

D. Bhattacharya and G. Srinivasan. The magnetic fields of neutron stars and their evolution. *X-ray Binaries*, pages 495–522, 1995.

D. Bhattacharya and E. P. J. van den Heuvel. Formation and evolution of binary and millisecond radio pulsars. Phys. Rep., 203:1–124, 1991. doi: 10.1016/0370-1573(91)90064-S.

S. Bhattacharyya. Measurement of neutron star parameters: A review of methods for low-mass X-ray binaries. *Advances in Space Research*, 45:949–978, April 2010. doi: 10.1016/j.asr.2010.01.010.

L. Bildsten. Theory and observations of Type I X-Ray bursts from neutron stars. In S. S. Holt and W. W. Zhang, editors, *American Institute of Physics Conference Series*, volume 522 of *American Institute of Physics Conference Series*, pages 359–369, June 2000. doi: 10.1063/1.1291736.

L. Bildsten, D. Chakrabarty, J. Chiu, M. H. Finger, D. T. Koh, R. W. Nelson, T. A. Prince, B. C. Rubin, D. M. Scott, M. Stollberg, B. A. Vaughan, C. A. Wilson, and R. B. Wilson. Observations of Accreting Pulsars. ApJS, 113:367–408, December 1997. doi: 10.1086/313060.

L. Boirin, M. Méndez, M. Díaz Trigo, A. N. Parmar, and J. S. Kaastra. A highly-ionized absorber in the X-ray binary 4U 1323-62: A new explanation for the dipping phenomenon. A&A, 436:195–208, June 2005. doi: 10.1051/0004-6361:20041940.

L. Boirin, L. Keek, M. Méndez, A. Cumming, J. J. M. in't Zand, J. Cottam, F. Paerels, and W. H. G. Lewin. Discovery of X-ray burst triplets in EXO 0748-676. A&A, 465: 559–573, April 2007. doi: 10.1051/0004-6361:20066204.

J. M. Bonnet-Bidaud, F. Haberl, P. Ferrando, P. J. Bennie, and E. Kendziorra. The eclipsing bursting X-ray binary EXO 0748-676 revisited by XMM-Newton. A&A, 365:L282–L287, January 2001. doi: 10.1051/0004-6361:20000222.

B. Boroson, K. O'Brien, K. Horne, T. Kallman, M. Still, P. T. Boyd, H. Quaintrell, and S. D. Vrtilek. Discovery of Millihertz ULTRAVIOLET Quasi-periodic Oscillations in Hercules X-1. ApJ, 545:399–406, December 2000. doi: 10.1086/317786.

E. Bozzo, L. Stella, M. Vietri, and P. Ghosh. Can disk-magnetosphere interaction models and beat frequency models for quasi-periodic oscillation in accreting X-ray pulsars be reconciled? A&A, 493:809–818, January 2009. doi: 10.1051/0004-6361:200810658.

E. Bozzo, P. Pjanka, P. Romano, A. Papitto, C. Ferrigno, S. Motta, A. A. Zdziarski, F. Pintore, T. Di Salvo, L. Burderi, D. Lazzati, G. Ponti, and L. Pavan. IGR J17451-3022: A dipping and eclipsing low mass X-ray binary. A&A, 589:A42, May 2016. doi: 10.1051/0004-6361/201527501.

D. A. H. Buckley. First-Light Instrumentation for the SALT. In R. Clowes, A. Adamson, and G. Bromage, editors, *The New Era of Wide Field Astronomy*, volume 232 of *Astronomical Society of the Pacific Conference Series*, page 386, 2001.

D. A. H. Buckley, E. B. Burgh, P. L. Cottrell, K. H. Nordsieck, D. O'Donoghue, and T. B. Williams. Status of the Southern African Large Telescope (SALT) first-generation instruments. In *Society of Photo-Optical Instrumentation Engineers (SPIE) Conference Series*, volume 6269 of Proc. SPIE, page 62690A, June 2006. doi: 10.1117/12.673838.

D. A. Buote, C. R. Canizares, and A. C. Fabian. X-ray emission lines and multiphase gas in elliptical galaxies and galaxy clusters. MNRAS, 310:483–510, December 1999. doi: 10.1046/j.1365-8711.1999.02969.x.

D. N. Burrows, J. E. Hill, J. A. Nousek, J. A. Kennea, A. Wells, J. P. Osborne, A. F. Abbey, A. Beardmore, K. Mukerjee, A. D. T. Short, G. Chincarini, S. Campana, O. Citterio, A. Moretti, C. Pagani, G. Tagliaferri, P. Giommi, M. Capalbi, F. Tamburelli, L. Angelini, G. Cusumano, H. W. Bräuninger, W. Burkert, and G. D. Hartner. The Swift X-Ray Telescope. Space Sci. Rev., 120:165–195, October 2005. doi: 10.1007/s11214-005-5097-2.

E. M. Cackett, E. F. Brown, N. Degenaar, J. M. Miller, M. Reynolds, and R. Wijnands. An X-ray-UV correlation in Cen X-4 during quiescence. MNRAS, 433:1362–1368, August 2013. doi: 10.1093/mnras/stt804.

P. J. Callanan, J. E. Grindlay, and A. M. Cool. Optical Observations of 4U 1915-05, and the Stability of the Long Term Ephemeris. PASJ, 47:153–162, April 1995.

A. Camero-Arranz, M. H. Finger, N. R. Ikhsanov, C. A. Wilson-Hodge, and E. Beklen. New Torque Reversal and Spin-up of 4U 1626-67 Observed by Fermi/Gamma-ray Burst Monitor and Swift/Burst Alert Telescope. ApJ, 708:1500–1506, January 2010. doi: 10.1088/0004-637X/708/2/1500.

C. R. Canizares, D. P. Huenemoerder, D. S. Davis, D. Dewey, K. A. Flanagan, J. Houck, T. H. Markert, H. L. Marshall, M. L. Schattenburg, N. S. Schulz, M. Wise, J. J. Drake, and N. S. Brickhouse. High-Resolution X-Ray Spectra of Capella: Initial Results from the Chandra High-Energy Transmission Grating Spectrometer. ApJ, 539:L41–L44, August 2000. doi: 10.1086/312823.

D. Chakrabarty. High-Speed Optical Photometry of the Ultracompact X-Ray Binary 4U 1626-67. ApJ, 492:342–351, January 1998. doi: 10.1086/305035.

D. Chakrabarty, L. Bildsten, J. M. Grunsfeld, D. T. Koh, T. A. Prince, B. A. Vaughan, M. H. Finger, D. M. Scott, and R. B. Wilson. Torque Reversal and Spin-down of the Accretion-powered Pulsar 4U 1626-67. ApJ, 474:414–425, January 1997. doi: 10.1086/303445.

D. Chakrabarty, L. Homer, P. A. Charles, and D. O'Donoghue. Millihertz Optical/Ultraviolet Oscillations in 4U 1626-67: Evidence for a Warped Accretion Disk. ApJ, 562:985–991, December 2001. doi: 10.1086/323877.

S. Chaty. Nature, Formation, and Evolution of High Mass X-Ray Binaries. In L. Schmidtobreick, M. R. Schreiber, and C. Tappert, editors, *Evolution of Compact Binaries*, volume 447 of *Astronomical Society of the Pacific Conference Series*, page 29, September 2011.

T. J. Chester. Continuum optical pulsation from the companions of binary X-ray pulsars. ApJ, 227:569–578, January 1979. doi: 10.1086/156767.

Y. Chou. Measuring the orbital periods of low mass X-ray binaries in the X-ray band. *Research in Astronomy and Astrophysics*, 14:1367-1382, November 2014. doi: 10.1088/1674-4527/14/11/001.

Y. Chou and J. E. Grindlay. Binary and Long-Term (Triple?) Modulations of 4U 1820-30 in NGC 6624. ApJ, 563:934–940, December 2001. doi: 10.1086/324038.

M. J. Church and M. Balucinska-Church. A complex continuum model for the low-mass X-ray binary dipping sources: application to X 1624-49. A&A, 300:441, August 1995.

M. J. Church, M. Bałucińska-Church, T. Dotani, and K. Asai. Progressive Covering of the Accretion Disk Corona during Dipping in the Low-Mass X-Ray Binary XBT 0748-676. ApJ, 504:516–521, September 1998. doi: 10.1086/306049.

M. J. Church, A. Gibiec, and M. Bałucińska-Church. The nature of the island and banana states in atoll sources and a unified model for low-mass X-ray binaries. MNRAS, 438:2784–2797, March 2014. doi: 10.1093/mnras/stt2364.

W. I. Clarkson, P. A. Charles, M. J. Coe, and S. Laycock. Long-term properties of accretion discs in X-ray binaries - II. Stability of radiation-driven warping. MNRAS, 343:1213–1223, August 2003. doi: 10.1046/j.1365-8711.2003.06761.x.

R. H. D. Corbet, A. P. Smale, P. A. Charles, W. H. G. Lewin, J. W. Menzies, T. Naylor, W. Penninx, M. Sztajno, J. R. Thorstensen, J. Trumper, and J. van Paradijs. Connections between X-ray and optical variability in the low mass X-ray binary 1735-444. MNRAS, 239:533–547, August 1989. doi: 10.1093/mnras/239.2.533.

D. Crampton and R. D. McClure. Photometry of the optical counterpart of the X-ray source 4U1626-67. PASP, 91:117–119, February 1979. doi: 10.1086/130454.

D. Crampton, J. Stauffer, J. B. Hutchings, A. P. Cowley, and P. Ianna. Optical observations of the X-ray nova EXO 0748-676 near maximum light. ApJ, 306: 599–604, July 1986. doi: 10.1086/164369.

A. D'Aì, T. di Salvo, D. Ballantyne, R. Iaria, N. R. Robba, A. Papitto, A. Riggio, L. Burderi, S. Piraino, A. Santangelo, G. Matt, M. Dovčiak, and V. Karas. A self-consistent approach to the hard and soft states of 4U 1705-44. A&A, 516:A36, June 2010. doi: 10.1051/0004-6361/200913758.

A. D'Aì, R. Iaria, T. Di Salvo, A. Riggio, L. Burderi, and N. R. Robba. Chandra X-ray spectroscopy of a clear dip in GX 13+1. A&A, 564:A62, April 2014. doi: 10.1051/0004-6361/201322044.

J. A. de Jong, J. van Paradijs, and T. Augusteijn. Reprocessing of X rays in low-mass X-ray binaries. A&A, 314:484–490, October 1996.

N. Degenaar, M. T. Wolff, P. S. Ray, K. S. Wood, J. Homan, W. H. G. Lewin, P. G. Jonker, E. M. Cackett, J. M. Miller, E. F. Brown, and R. Wijnands. Further X-ray observations of EXO 0748-676 in quiescence: evidence for a cooling neutron star crust. MNRAS, 412:1409–1418, April 2011. doi: 10.1111/j.1365-2966.2010.17562.x.

T. Di Salvo, L. Stella, N. R. Robba, M. van der Klis, L. Burderi, G. L. Israel, J. Homan, S. Campana, F. Frontera, and A. N. Parmar. The Discovery of a State-Dependent Hard Tail in the X-Ray Spectrum of the Luminous Z Source GX 17+2. ApJ, 544: L119–L122, December 2000. doi: 10.1086/317309.

M. Díaz Trigo and L. Boirin. Accretion disc atmospheres and winds in low-mass X-ray binaries. *Astronomische Nachrichten*, 337:368, May 2016. doi: 10.1002/asna.201612315.

M. Díaz Trigo, A. N. Parmar, L. Boirin, M. Méndez, and J. S. Kaastra. Spectral changes during dipping in low-mass X-ray binaries due to highly-ionized absorbers. A&A, 445:179–195, January 2006. doi: 10.1051/0004-6361:20053586.

M. Díaz Trigo, A. N. Parmar, L. Boirin, C. Motch, A. Talavera, and S. Balman. Variations in the dip properties of the low-mass X-ray binary XB 1254-690 observed with XMM-Newton and INTEGRAL. A&A, 493:145–157, January 2009. doi: 10.1051/0004-6361:200810154.

J. F. Dolan. A Catalogue of Discrete Celestial X-Ray Sources. AJ, 75:223, April 1970. doi: 10.1086/110966.

G. Dubus, J.-P. Lasota, J.-M. Hameury, and P. Charles. X-ray irradiation in low-mass binary systems. MNRAS, 303:139–147, February 1999. doi: 10.1046/j.1365-8711.1999.02212.x.

M. Durant, T. Shahbaz, P. Gandhi, R. Cornelisse, T. Muñoz-Darias, J. Casares, V. Dhillon, T. Marsh, H. Spruit, K. O'Brien, D. Steeghs, and R. Hynes. High time resolution optical/X-ray cross-correlations for X-ray binaries: anticorrelations and rapid variability. MNRAS, 410:2329–2338, February 2011. doi: 10.1111/j.1365-2966.2010.17604.x.

P. P. Eggleton. Approximations to the radii of Roche lobes. ApJ, 268:368, May 1983. doi: 10.1086/160960.

P. P. Eggleton and F. Verbunt. Triple star evolution and the formation of short-period, low mass X-ray binaries. MNRAS, 220:13P–18P, May 1986. doi: 10.1093/mnras/220.1.13P.

G. Fabbiano. Populations of X-Ray Sources in Galaxies. ARA&A, 44:323–366, September 2006. doi: 10.1146/annurev.astro.44.051905.092519.

A. C. Fabian, P. W. Guilbert, C. Motch, M. Ricketts, S. A. Ilovaisky, and C. Chevalier. GX 339-4 - Cyclotron radiation from an accretion flow. A&A, 111:L9, July 1982.

R. P. Fender and E. Kuulkers. On the peak radio and X-ray emission from neutron star and black hole candidate X-ray transients. MNRAS, 324:923–930, July 2001. doi: 10.1046/j.1365-8711.2001.04345.x.

J. Frank, A. King, and D. Raine. *Accretion power in astrophysics.* 1992.

B. Friedman and V. R. Pandharipande. Hot and cold, nuclear and neutron matter. *Nuclear Physics A*, 361:502–520, May 1981. doi: 10.1016/0375-9474(81)90649-7.

M. Y. Fujimoto. Angular distribution of radiation from low-mass X-ray binaries. ApJ, 324:995–1000, January 1988. doi: 10.1086/165955.

D. K. Galloway, M. P. Muno, J. M. Hartman, D. Psaltis, and D. Chakrabarty. Thermonuclear (Type I) X-Ray Bursts Observed by the Rossi X-Ray Timing Explorer. ApJS, 179:360-422, December 2008. doi: 10.1086/592044.

D. K. Galloway, J. Lin, D. Chakrabarty, and J. M. Hartman. Discovery of a 552 Hz Burst Oscillation in the Low-Mass X-Ray Binary EXO 0748-676. ApJ, 711: L148–L151, March 2010. doi: 10.1088/2041-8205/711/2/L148.

D. K. Galloway, A. N. Ajamyan, J. Upjohn, and M. Stuart. Intermittent dipping in a low-mass X-ray binary. MNRAS, 461:3847–3853, October 2016. doi: 10.1093/mnras/stw1576.

J. Gaskin, C. Wilson-Hodge, B. Ramsey, R. Elsner, A. F. Tennant, K. Kilaru, D. A. Swartz, S. Christe, A. Y. Shih, F. K. Baganoff, P. Seller, M. Wilson, and D. Stuchlik. SuperHERO: The Next Generation Hard X-Ray Focusing Telescope. In *American Astronomical Society Meeting Abstracts*, volume 225 of *American Astronomical Society Meeting Abstracts*, page 413.05, January 2015.

P. Ghosh and F. K. Lamb. Accretion by rotating magnetic neutron stars. III - Accretion torques and period changes in pulsating X-ray sources. ApJ, 234:296–316, November 1979. doi: 10.1086/157498.

R. Giacconi, E. Kellogg, P. Gorenstein, H. Gursky, and H. Tananbaum. An X-Ray Scan of the Galactic Plane from UHURU. ApJ, 165:L27, April 1971. doi: 10.1086/180711.

M. Gilfanov, R. Sunyeav, and E. Churazov, editors. *Lighthouses of the Universe: The Most Luminous Celestial Objects and Their Use for Cosmology*, 2002. doi: 10.1007/b88624.

M. Gottwald, F. Haberl, A. N. Parmar, and N. E. White. The bursting behavior of the transient X-ray burst source EXO 0748-676 - A dependence between the X-ray burst properties and the strength of the persistent emission. ApJ, 308:213–224, September 1986. doi: 10.1086/164491.

J. E. Grindlay. The discovery of bursting X-ray sources. *Comments on Astrophysics*, 6:165–175, 1976.

J. E. Grindlay, J. E. McClintock, C. R. Canizares, L. Cominsky, F. K. Li, W. H. G. Lewin, and J. van Paradijs. Discovery of optical bursts from an X-ray burst source, MXB1735-44. Nature, 274:567, August 1978. doi: 10.1038/274567a0.

N. V. Gusinskaia, A. T. Deller, J. W. T. Hessels, N. Degenaar, J. C. A. Miller-Jones, R. Wijnands, A. S. Parikh, T. D. Russell, and D. Altamirano. Jet quenching in the neutron star low-mass X-ray binary 1RXS J180408.9-342058. MNRAS, 470: 1871–1880, September 2017. doi: 10.1093/mnras/stx1235.

G. M. H. J. Habets. *Advanced evolution of helium stars and massive close binaries*. PhD thesis, , Univ. Amsterdam, (1985). Advisor: E.P.J. van den Heuvel, 1985.

J. A. Hackwell, G. L. Grasdalen, R. D. Gehrz, L. Cominsky, W. H. G. Lewin, and J. van Paradijs. The detection of an optical burst coincident with an X-ray burst from MXB 1837 + 05 /Ser X-1/. ApJ, 233:L115–L119, November 1979. doi: 10.1086/183088.

P. Hakala, G. Ramsay, P. Muhli, P. Charles, D. Hannikainen, K. Mukai, and O. Vilhu. XMM-Newton observations of UW CrB: detection of X-ray bursts and evidence for accretion disc evolution. MNRAS, 356:1133–1138, January 2005. doi: 10.1111/j.1365-2966.2004.08543.x.

G. Hasinger and M. van der Klis. Two patterns of correlated X-ray timing and spectral behaviour in low-mass X-ray binaries. A&A, 225:79–96, November 1989.

C.-C. He and L. Keek. Anisotropy of X-Ray Bursts from Neutron Stars with Concave Accretion Disks. ApJ, 819:47, March 2016. doi: 10.3847/0004-637X/819/1/47.

R. C. Hickox and S. D. Vrtilek. Pulse-Phase Spectroscopy of SMC X-1 with Chandra and XMM-Newton: Reprocessing by a Precessing Disk? ApJ, 633:1064–1075, November 2005. doi: 10.1086/491596.

J. Homan and M. van der Klis. A 695 HZ Quasi-periodic Oscillation in the Low-Mass X-Ray Binary EXO 0748-676. ApJ, 539:847–850, August 2000. doi: 10.1086/309280.

J. Homan, J. K. Fridriksson, and R. A. Remillard. On the Geometric Nature of Low-frequency Quasi-periodic Oscillations in Neutron-star Low-mass X-Ray Binaries. ApJ, 812:80, October 2015. doi: 10.1088/0004-637X/812/1/80.

L. Homer, P. A. Charles, P. Hakala, P. Muhli, I.-C. Shih, A. P. Smale, and G. Ramsay. On the multi-periodicities in the X-ray dipper XB1916-053. MNRAS, 322:827–842, April 2001. doi: 10.1046/j.1365-8711.2001.04170.x.

C.-P. Hu, Y. Chou, and Y.-Y. Chung. A Parameterization Study of the Properties of the X-Ray Dips in the Low-Mass X-Ray Binary X1916-053. ApJ, 680:1405-1411, June 2008. doi: 10.1086/527549.

D. G. Hummer. The ionization structure of planetary nebulae, II. Collisional cooling of pure hydrogen nebulae. MNRAS, 125:461, 1963. doi: 10.1093/mnras/125.5.461.

R. I. Hynes. Correlated X-ray and Optical Variability in X-ray Binaries. In J.-M. Hameury and J.-P. Lasota, editors, *The Astrophysics of Cataclysmic Variables and Related Objects*, volume 330 of *Astronomical Society of the Pacific Conference Series*, page 237, August 2005.

R. I. Hynes. Multiwavelength Observations of Accretion in Low-Mass X-ray Binary Systems. *ArXiv e-prints*, October 2010.

R. I. Hynes and E. D. Jones. The Quiescent Optical and Infrared Counterpart to EXO 0748-676 = UY Vol. ApJ, 697:L14–L17, May 2009. doi: 10.1088/0004-637X/697/1/L14.

R. I. Hynes, C. A. Haswell, W. Cui, C. R. Shrader, K. O'Brien, S. Chaty, D. R. Skillman, J. Patterson, and K. Horne. The remarkable rapid X-ray, ultraviolet, optical and infrared variability in the black hole XTE J1118+480. MNRAS, 345:292–310, October 2003. doi: 10.1046/j.1365-8711.2003.06938.x.

R. I. Hynes, P. A. Charles, M. R. Garcia, E. L. Robinson, J. Casares, C. A. Haswell, A. K. H. Kong, M. Rupen, R. P. Fender, R. M. Wagner, E. Gallo, B. A. C. Eves, T. Shahbaz, and C. Zurita. Correlated X-Ray and Optical Variability in V404 Cygni in Quiescence. ApJ, 611:L125–L128, August 2004. doi: 10.1086/424005.

R. I. Hynes, K. Horne, K. O'Brien, C. A. Haswell, E. L. Robinson, A. R. King, P. A. Charles, and K. J. Pearson. Multiwavelength Observations of EXO 0748-676. I. Reprocessing of X-Ray Bursts. ApJ, 648:1156–1168, September 2006. doi: 10.1086/505592.

Y. Hyodo, Y. Ueda, T. Yuasa, Y. Maeda, K. Makishima, and K. Koyama. Timing and Spectral Study of AXJ1745.6-2901 with Suzaku. PASJ, 61:S99–S106, January 2009. doi: 10.1093/pasj/61.sp1.S99.

C. D. Igna and D. A. Leahy. Light-curve dip production through accretion stream-accretion disc impact in the HZ Her/Her X-1 binary star system. MNRAS, 425:8–20, September 2012. doi: 10.1111/j.1365-2966.2012.21303.x.

A. F. Illarionov and R. A. Sunyaev. Why the Number of Galactic X-ray Stars Is so Small? A&A, 39:185, February 1975.

S. A. Ilovaisky, C. Motch, and C. Chevalier. Discovery of optical pulsations from 4U 1626-67. A&A, 70:L19–L22, December 1978.

S. A. Ilovaisky, C. Chevalier, N. E. White, K. O. Mason, P. W. Sanford, J. P. Delvaille, and H. W. Schnopper. Simultaneous X-ray and optical observations of rapid variability in Scorpius X-1. MNRAS, 191:81–93, April 1980. doi: 10.1093/mnras/191.1.81.

Z. Ioannou, T. Naylor, A. P. Smale, P. A. Charles, and K. Mukai. Understanding the LMXB X2127+119 in M 15. I. X-ray eclipses and dips. A&A, 382:130–140, January 2002. doi: 10.1051/0004-6361:20011581.

F. J. Jablonski, M. G. Pereira, J. Braga, and C. D. Gneiding. Discovery of Optical Pulsations in V2116 Ophiuchi equivalent to GX 1+4. ApJ, 482:L171–L174, June 1997a. doi: 10.1086/310699.

F. J. Jablonski, M. G. Pereira, J. Braga, and C. D. Gneiding. Discovery of Optical Pulsations in V2116 Ophiuchi equivalent to GX 1+4. ApJ, 482:L171–L174, June 1997b. doi: 10.1086/310699.

C. Jain and B. Paul. Eclipse timings of the LMXB XTE J1710-281: orbital period glitches. MNRAS, 413:2–6, May 2011. doi: 10.1111/j.1365-2966.2010.18110.x.

C. Jain, B. Paul, K. Joshi, A. Dutta, and H. Raichur. Search for orbital motion of the pulsar 4U 1626-67: Candidate for a neutron star with a supernova fall-back accretion disk. *Journal of Astrophysics and Astronomy*, 28:175–184, April 2008. doi: 10.1007/s12036-007-0015-5.

C. Jain, B. Paul, and A. Dutta. Spectral and temporal changes associated with flux enhancement in 4U 1626-67. MNRAS, 403:920–925, April 2010. doi: 10.1111/j.1365-2966.2009.16170.x.

P. C. Joss. X-ray bursts and neutron-star thermonuclear flashes. Nature, 270:310–314, November 1977. doi: 10.1038/270310a0.

P. C. Joss, Y. Avni, and S. Rappaport. Accreting neutron stars in highly compact binary systems and the nature of 3U 1626-67. ApJ, 221:645–651, April 1978a. doi: 10.1086/156068.

P. C. Joss, Y. Avni, and S. Rappaport. Accreting neutron stars in highly compact binary systems and the nature of 3U 1626-67. ApJ, 221:645–651, April 1978b. doi: 10.1086/156068.

J. S. Kaastra, J. Ebrero, N. Arav, E. Behar, S. Bianchi, G. Branduardi-Raymont, M. Cappi, E. Costantini, G. A. Kriss, B. De Marco, M. Mehdipour, S. Paltani, P.-O. Petrucci, C. Pinto, G. Ponti, K. C. Steenbrugge, and C. P. de Vries. Multiwavelength campaign on Mrk 509. XIV. Chandra HETGS spectra. A&A, 570:A73, October 2014. doi: 10.1051/0004-6361/201424662.

R. Kaur, B. Paul, B. Kumar, and R. Sagar. A Study of the Long-Term Evolution of Quasi-Periodic Oscillations in the Accretion-Powered X-Ray Pulsar 4U 1626-67. ApJ, 676:1184-1188, April 2008. doi: 10.1086/529130.

D. Klochkov, R. Staubert, K. Postnov, N. Shakura, and A. Santangelo. Continuous monitoring of pulse period variations in Hercules X-1 using Swift/BAT. A&A, 506: 1261–1267, November 2009. doi: 10.1051/0004-6361/200912791.

J. M. Kommers, D. Chakrabarty, and W. H. G. Lewin. Sidebands due to Quasi-Periodic Oscillations in 4U 1626-67. ApJ, 497:L33–L37, April 1998. doi: 10.1086/311272.

M. M. Kotze, P. A. Charles, and L. A. Crause. Discovery of long-term superorbital periodicities in the pseudo-transient LMXBs: IGRJ17098-3628 and EXO0748-676. MNRAS, 395:1579–1584, May 2009. doi: 10.1111/j.1365-2966.2009.14640.x.

K. Koyama, Y. Hyodo, T. Inui, H. Nakajima, H. Matsumoto, T. G. Tsuru, T. Takahashi, Y. Maeda, N. Y. Yamazaki, H. Murakami, S. Yamauchi, Y. Tsuboi, A. Senda, J. Kataoka, H. Takahashi, S. S. Holt, and G. V. Brown. Iron and Nickel Line Diagnostics for the Galactic Center Diffuse Emission. PASJ, 59:245–255, January 2007. doi: 10.1093/pasj/59.sp1.S245.

U. Kraus, S. Blum, J. Schulte, H. Ruder, and P. Meszaros. Analyzing X-Ray Pulsar Profiles: Geometry and Beam Pattern of Centaurus X-3. ApJ, 467:794, August 1996. doi: 10.1086/177653.

F. K. Lamb, C. J. Pethick, and D. Pines. A Model for Compact X-Ray Sources: Accretion by Rotating Magnetic Stars. ApJ, 184:271–290, August 1973. doi: 10.1086/152325.

J. M. Lattimer and M. Prakash. Neutron Star Structure and the Equation of State. ApJ, 550:426–442, March 2001. doi: 10.1086/319702.

J. M. Lattimer and M. Prakash. Neutron star observations: Prognosis for equation of state constraints. Phys. Rep., 442:109–165, April 2007. doi: 10.1016/j.physrep.2007.02.003.

A. Lawrence, L. Cominsky, C. Engelke, G. Jernigan, W. H. G. Lewin, M. Matsuoka, K. Mitsuda, M. Oda, T. Ohashi, H. Pedersen, and J. van Paradijs. Simultaneous U, B, V, and X-ray measurements of a burst from 4U/MXB 1636-53. ApJ, 271:793–803, August 1983. doi: 10.1086/161245.

D. A. Leahy, R. F. Elsner, and M. C. Weisskopf. On searches for periodic pulsed emission - The Rayleigh test compared to epoch folding. ApJ, 272:256–258, September 1983. doi: 10.1086/161288.

A. Levine, C. P. Ma, J. McClintock, S. Rappaport, M. van der Klis, and F. Verbunt. 4U 1626-67 - The binary with the smallest known mass function. ApJ, 327:732–741, April 1988. doi: 10.1086/166230.

W. H. G. Lewin and G. W. Clark. Galactic bulge sources - What are they /X-ray sources in globular clusters and burst sources/. In J. Ehlers, J. J. Perry, and M. Walker, editors, *Ninth Texas Symposium on Relativistic Astrophysics*, volume 336 of *Annals of the New York Academy of Sciences*, pages 451–478, February 1980. doi: 10.1111/j.1749-6632.1980.tb15953.x.

W. H. G. Lewin and P. C. Joss. X-Ray Bursters and the X-Ray Sources of the Galactic Bulge. In W. H. G. Lewin and E. P. J. van den Heuvel, editors, *Accretion-Driven Stellar X-ray Sources*, page 41, 1983.

D. A. Liedahl, A. L. Osterheld, and W. H. Goldstein. New calculations of Fe L-shell X-ray spectra in high-temperature plasmas. ApJ, 438:L115–L118, January 1995. doi: 10.1086/187729.

A. P. Lightman and D. M. Eardley. Black Holes in Binary Systems: Instability of Disk Accretion. ApJ, 187:L1, January 1974. doi: 10.1086/181377.

Q. Z. Liu, J. van Paradijs, and E. P. J. van den Heuvel. A catalogue of low-mass X-ray binaries in the Galaxy, LMC, and SMC (Fourth edition). A&A, 469:807–810, July 2007. doi: 10.1051/0004-6361:20077303.

N. R. Lomb. Least-squares frequency analysis of unequally spaced data. Ap&SS, 39: 447–462, February 1976. doi: 10.1007/BF00648343.

G. Machin, P. J. Callanan, P. A. Charles, J. Thorstensen, K. Brownsberger, R. H. D. Corbet, R. Hamwey, E. T. Harlaftis, K. O. Mason, and K. Mukai. Optical and X-Ray Observations of 4U:0614+09. MNRAS, 247:205, November 1990.

C. Maitra and B. Paul. Pulse-phase-dependent Variations of the Cyclotron Absorption Features of the Accreting Pulsars A0535+26, XTE J1946+274, and 4U 1907+09 with Suzaku. ApJ, 771:96, July 2013. doi: 10.1088/0004-637X/771/2/96.

P. R. Maloney and M. C. Begelman. The Origin of Warped, Precessing Accretions Disks in X-Ray Binaries. ApJ, 491:L43–L46, December 1997. doi: 10.1086/311058.

J. Malzac, A. Merloni, and A. C. Fabian. Jet-disc coupling through a common energy reservoir in the black hole XTE J1118+480. MNRAS, 351:253–264, June 2004. doi: 10.1111/j.1365-2966.2004.07772.x.

C. B. Markwardt, F. E. Marshall, J. Swank, and T. Takeshima. XTE J1710-281 = 1RXS J171012.3-280754. IAU Circ., 6998, August 1998.

C. B. Markwardt, J. H. Swank, and T. E. Strohmayer. Discovery of the Orbital Period of the Bursting and Dipping Source XTE J1710-281. In *American Astronomical Society Meeting Abstracts*, volume 33 of *Bulletin of the American Astronomical Society*, page 1350, December 2001.

K. O. Mason and F. A. Cordova. Ultraviolet spectrophotometry of 2A 1822-371 - A bulge on the accretion disk. ApJ, 255:603–609, April 1982. doi: 10.1086/159862.

K. O. Mason, A. Breeveld, R. Much, M. Carter, F. A. Cordova, M. S. Cropper, J. Fordham, H. Huckle, C. Ho, H. Kawakami, J. Kennea, T. Kennedy, J. Mittaz, D. Pandel, W. C. Priedhorsky, T. Sasseen, R. Shirey, P. Smith, and J.-M. Vreux. The XMM-Newton optical/UV monitor telescope. A&A, 365:L36–L44, January 2001. doi: 10.1051/0004-6361:20000044.

J. E. McClintock, H. V. Bradt, R. E. Doxsey, J. G. Jernigan, C. R. Canizares, and W. A. Hiltner. Optical candidates for two X-ray bursters and an X-ray pulsar. Nature, 270:320, November 1977. doi: 10.1038/270320a0.

J. E. McClintock, C. R. Canizares, L. Cominsky, F. K. Li, W. H. G. Lewin, J. van Paradijs, and J. E. Grindlay. A 3-s delay in an optical burst from X-ray burst source MXB1735-44. Nature, 279:47–49, May 1979. doi: 10.1038/279047a0.

J. E. McClintock, F. K. Li, C. R. Canizares, and J. E. Grindlay. Simultaneous X-ray and optical observations of the 7.7 second X-ray pulsar 4U 1626-67. ApJ, 235: L81–L85, January 1980. doi: 10.1086/183163.

A. Merloni, T. Di Matteo, and A. C. Fabian. Magnetic flares and the optical variability of the X-ray transient XTE J1118+480. MNRAS, 318:L15–L19, October 2000. doi: 10.1046/j.1365-8711.2000.03943.x.

J. Middleditch and J. Nelson. Studies of optical pulsations from HZ Herculis/Hercules X-1: a determination of the mass of the neutron star. ApJ, 208:567–586, September 1976. doi: 10.1086/154638.

J. Middleditch, K. O. Mason, J. E. Nelson, and N. E. White. 4U 1626-67 - A prograde spinning X-ray pulsar in a 2500 S binary system. ApJ, 244:1001–1021, March 1981. doi: 10.1086/158772.

S. Migliari and R. P. Fender. Jets in neutron star X-ray binaries: a comparison with black holes. MNRAS, 366:79–91, February 2006. doi: 10.1111/j.1365-2966.2005.09777.x.

J. M. Miller, D. Maitra, E. M. Cackett, S. Bhattacharyya, and T. E. Strohmayer. A Fast X-ray Disk Wind in the Transient Pulsar IGR J17480-2446 in Terzan 5. ApJ, 731:L7, April 2011. doi: 10.1088/2041-8205/731/1/L7.

J. M. Miller, A. C. Fabian, J. Kaastra, T. Kallman, A. L. King, D. Proga, J. Raymond, and C. S. Reynolds. Powerful, Rotating Disk Winds from Stellar-mass Black Holes. ApJ, 814:87, December 2015. doi: 10.1088/0004-637X/814/2/87.

K. Mitsuda, H. Inoue, K. Koyama, K. Makishima, M. Matsuoka, Y. Ogawara, K. Suzuki, Y. Tanaka, N. Shibazaki, and T. Hirano. Energy spectra of low-mass binary X-ray sources observed from TENMA. PASJ, 36:741–759, 1984.

K. Mitsuda, H. Inoue, N. Nakamura, and Y. Tanaka. Luminosity-related changes of the energy spectrum of X1608-522. PASJ, 41:97–111, 1989.

D.-S. Moon and S. S. Eikenberry. Large X-Ray Flares from LMC X-4: Discovery of Millihertz Quasi-periodic Oscillations and Quasi-periodic Oscillation-Modulated Pulsations. ApJ, 549:L225–L228, March 2001. doi: 10.1086/319160.

C. Motch, M. W. Pakull, M. Mouchet, and K. Beuermann. An X-ray and optical study of the low-mass X-ray source 4U 1556-605. A&A, 219:158–166, July 1989a.

C. Motch, H. Pedersen, S. A. Ilovaisky, C. Chevalier, and M. Mouchet. Optical emission from the high inclination X ray transient EXO 0748-676. In J. Hunt and B. Battrick, editors, *Two Topics in X-Ray Astronomy, Volume 1: X Ray Binaries. Volume 2: AGN and the X Ray Background*, volume 296 of *ESA Special Publication*, November 1989b.

J. Neilsen and J. C. Lee. Accretion disk winds as the jet suppression mechanism in the microquasar GRS 1915+105. Nature, 458:481–484, March 2009. doi: 10.1038/nature07680.

R. W. Nelson, B. A. Vaughan, L. Bildsten, D. Chakrabarty, D. T. Koh, T. A. Prince, M. H. Finger, R. B. Wilson, and B. C. Rubin. On the Dramatic Spin-Up/Spin-Down Torque Reversals in BATSE Observations of Accretion Powered Pulsars. In D. T. Wickramasinghe, G. V. Bicknell, and L. Ferrario, editors, *IAU Colloq. 163: Accretion Phenomena and Related Outflows*, volume 121 of *Astronomical Society of the Pacific Conference Series*, page 256, 1997.

W. G. Newton. Neutron stars: A taste of pasta? *Nature Physics*, 9:396–397, July 2013. doi: 10.1038/nphys2663.

M. Nobukawa, T. G. Tsuru, Y. Takikawa, Y. Hyodo, T. Inui, H. Nakajima, H. Matsumoto, K. Koyama, H. Murakami, and S. Yamauchi. Suzaku Spectroscopy of an X-Ray Reflection Nebula and a New Supernova Remnant Candidate in the SgrB1 Region. PASJ, 60:S191–S200, January 2008. doi: 10.1093/pasj/60.sp1.S191.

K. O'Brien, K. Horne, R. I. Hynes, W. Chen, C. A. Haswell, and M. D. Still. Echoes in X-ray binaries. MNRAS, 334:426–434, August 2002. doi: 10.1046/j.1365-8711.2002.05530.x.

D. O'Donoghue. Correction of spherical aberration in the Southern African Large Telescope (SALT). In P. Dierickx, editor, *Optical Design, Materials, Fabrication, and Maintenance*, volume 4003 of Proc. SPIE, pages 363–372, July 2000. doi: 10.1117/12.391526.

D. O'Donoghue, D. A. H. Buckley, L. A. Balona, D. Bester, L. Botha, J. Brink, D. B. Carter, P. A. Charles, A. Christians, F. Ebrahim, R. Emmerich, W. Esterhuyse, G. P. Evans, C. Fourie, P. Fourie, H. Gajjar, M. Gordon, C. Gumede, M. de Kock,

A. Koeslag, W. P. Koorts, H. Kriel, F. Marang, J. G. Meiring, J. W. Menzies, P. Menzies, D. Metcalfe, B. Meyer, L. Nel, J. O'Connor, F. Osman, C. Du Plessis, H. Rall, A. Riddick, E. Romero-Colmenero, S. B. Potter, C. Sass, H. Schalekamp, N. Sessions, S. Siyengo, V. Sopela, H. Steyn, J. Stoffels, J. Scholtz, G. Swart, A. Swat, J. Swiegers, T. Tiheli, P. Vaisanen, W. Whittaker, and F. van Wyk. First science with the Southern African Large Telescope: peering at the accreting polar caps of the eclipsing polar SDSS J015543.40+002807.2. MNRAS, 372:151–162, October 2006. doi: 10.1111/j.1365-2966.2006.10834.x.

G. I. Ogilvie and G. Dubus. Precessing warped accretion discs in X-ray binaries. MNRAS, 320:485–503, February 2001. doi: 10.1046/j.1365-8711.2001.04011.x.

T. Oosterbroek, A. N. Parmar, L. Sidoli, J. J. M. in't Zand, and J. Heise. BeppoSAX observation of the eclipsing dipping X-ray binary X 1658-298. A&A, 376:532–542, September 2001. doi: 10.1051/0004-6361:20011006.

M. Orlandini, D. Dal Fiume, F. Frontera, S. Del Sordo, S. Piraino, A. Santangelo, A. Segreto, T. Oosterbroek, and A. N. Parmar. BEPPOSAX Observation of 4U 1626-67: Discovery of an Absorption Cyclotron Resonance Feature. ApJ, 500:L163–L166, June 1998. doi: 10.1086/311404.

B. Paczynski. Common Envelope Binaries. In P. Eggleton, S. Mitton, and J. Whelan, editors, *Structure and Evolution of Close Binary Systems*, volume 73 of *IAU Symposium*, page 75, 1976.

V. R. Pandharipande and R. A. Smith. A model neutron solid with π^0 condensate. *Nuclear Physics A*, 237:507–532, January 1975. doi: 10.1016/0375-9474(75)90415-7.

A. Papitto, C. Ferrigno, E. Bozzo, N. Rea, L. Pavan, L. Burderi, M. Burgay, S. Campana, T. di Salvo, M. Falanga, M. D. Filipović, P. C. C. Freire, J. W. T. Hessels, A. Possenti, S. M. Ransom, A. Riggio, P. Romano, J. M. Sarkissian, I. H. Stairs, L. Stella, D. F. Torres, M. H. Wieringa, and G. F. Wong. Swings between rotation and accretion power in a binary millisecond pulsar. Nature, 501:517–520, September 2013. doi: 10.1038/nature12470.

A. N. Parmar, M. Gottwald, F. Haberl, P. Giommi, and N. E. White. The EXO 0748-676: an exciting new X-ray transient. In W. R. Burke, editor, *Recent Results on Cataclysmic Variables. The Importance of IUE and Exosat Results on Cataclysmic Variables and Low-Mass X-Ray Binaries*, volume 236 of *ESA Special Publication*, June 1985a.

A. N. Parmar, N. E. White, P. Giommi, F. Haberl, H. Pedersen, and M. Mayor. EXO 0748-676. IAU Circ., 4039, February 1985b.

A. N. Parmar, N. E. White, P. Giommi, and M. Gottwald. The discovery of 3.8 hour periodic intensity dips and eclipses from the transient low-mass X-ray binary EXO 0748-676. ApJ, 308:199–212, September 1986. doi: 10.1086/164490.

B. Paul, M. Archana, and L. Saripalli. Simultaneous X-ray and optical observations of thermonuclear bursts in the LMXB EXO 0748-676. *Bulletin of the Astronomical Society of India*, 40:93–104, June 2012.

G. G. Pavlov, D. Sanwal, and M. A. Teter. Central Compact Objects in Supernova Remnants. In F. Camilo and B. M. Gaensler, editors, *Young Neutron Stars and Their Environments*, volume 218 of *IAU Symposium*, page 239, 2004.

H. Pedersen, J. Lub, H. Inoue, K. Koyama, K. Makishima, M. Matsuoka, K. Mitsuda, T. Murakami, M. Oda, Y. Ogawara, T. Ohashi, N. Shibazaki, Y. Tanaka, S. Hayakawa, H. Kunieda, F. Makino, K. Masai, F. Nagase, Y. Tawara, S. Miyamoto, H. Tsunemi, K. Yamashita, I. Kondo, J. G. Jernigan, J. van Paradijs, A. Beardsley, L. Cominsky, J. Doty, and W. H. G. Lewin. Simultaneous optical and X-ray bursts from 4U/MXB 1636-53. ApJ, 263:325–339, December 1982. doi: 10.1086/160507.

H. Pedersen, S. Cristiani, S. D'Odorico, B. Thomsen, and P. Angebault. EXO 0748-676. IAU Circ., 4047, March 1985.

G. Ponti, R. P. Fender, M. C. Begelman, R. J. H. Dunn, J. Neilsen, and M. Coriat. Ubiquitous equatorial accretion disc winds in black hole soft states. MNRAS, 422: 11–15, May 2012. doi: 10.1111/j.1745-3933.2012.01224.x.

G. Ponti, T. Muñoz-Darias, and R. P. Fender. A connection between accretion state and Fe K absorption in an accreting neutron star: black hole-like soft-state winds? MNRAS, 444:1829–1834, October 2014. doi: 10.1093/mnras/stu1742.

G. Ponti, S. Bianchi, T. Muñoz-Darias, B. De Marco, T. Dwelly, R. P. Fender, K. Nandra, N. Rea, K. Mori, D. Haggard, C. O. Heinke, N. Degenaar, T. Aramaki, M. Clavel, A. Goldwurm, C. J. Hailey, G. L. Israel, M. R. Morris, A. Rushton, and R. Terrier. On the Fe K absorption - accretion state connection in the Galactic Centre neutron star X-ray binary AX J1745.6-2901. MNRAS, 446:1536–1550, January 2015. doi: 10.1093/mnras/stu1853.

J. E. Pringle. Self-induced warping of accretion discs. MNRAS, 281:357–361, July 1996. doi: 10.1093/mnras/281.1.357.

J. E. Pringle and M. J. Rees. Accretion Disc Models for Compact X-Ray Sources. A&A, 21:1, October 1972.

H. Raichur and B. Paul. Long-term flux variations in Cen X-3: clues from flux-dependent orbital modulation and pulsed fraction. MNRAS, 387:439–445, June 2008. doi: 10.1111/j.1365-2966.2008.13251.x.

G. Raman and B. Paul. X-ray and optical orbital modulation of EXO 0748-676 : A co-variability study using XMM-Newton. New A, 54:122–139, July 2017. doi: 10.1016/j.newast.2017.02.001.

S. Rappaport, T. Markert, F. K. Li, G. W. Clark, J. G. Jernigan, and J. E. McClintock. Discovery of a 7.68 second X-ray periodicity in 3U 1626-67. ApJ, 217:L29–L33, October 1977. doi: 10.1086/182532.

J. Reeves, C. Done, K. Pounds, Y. Terashima, K. Hayashida, N. Anabuki, M. Uchino, and M. Turner. On why the iron K-shell absorption in AGN is not a signature of the local warm/hot intergalactic medium. MNRAS, 385:L108–L112, March 2008. doi: 10.1111/j.1745-3933.2008.00443.x.

D. M. Russell, R. P. Fender, R. I. Hynes, C. Brocksopp, J. Homan, P. G. Jonker, and M. M. Buxton. Global optical/infrared-X-ray correlations in X-ray binaries: quantifying disc and jet contributions. MNRAS, 371:1334–1350, September 2006. doi: 10.1111/j.1365-2966.2006.10756.x.

E. E. Salpeter. Accretion of Interstellar Matter by Massive Objects. ApJ, 140:796–800, August 1964. doi: 10.1086/147973.

H. Schatz and K. E. Rehm. X-ray binaries. *Nuclear Physics A*, 777:601–622, October 2006. doi: 10.1016/j.nuclphysa.2005.05.200.

E. Schreier, R. Levinson, H. Gursky, E. Kellogg, H. Tananbaum, and R. Giacconi. Evidence for the Binary Nature of Centaurus X-3 from UHURU X-Ray Observations. ApJ, 172:L79, March 1972. doi: 10.1086/180896.

F. D. Seward and P. A. Charles. *Exploring the X-Ray Universe*. November 1995.

N. I. Shakura and R. A. Sunyaev. A theory of the instability of disk accretion on to black holes and the variability of binary X-ray sources, galactic nuclei and quasars. MNRAS, 175:613–632, June 1976. doi: 10.1093/mnras/175.3.613.

K. Shinoda, T. Kii, K. Mitsuda, F. Nagase, Y. Tanaka, K. Makishima, and N. Shibazaki. Discovery of the quasi-periodic oscillations from the X-ray pulsar X1627-673. PASJ, 42:L27–L32, April 1990.

A. Shirakawa and D. Lai. Magnetically Driven Precession of Warped Disks and Millihertz Variabilities in Accreting X-Ray Pulsars. ApJ, 565:1134–1140, February 2002. doi: 10.1086/324548.

Y. Soong and J. H. Swank. Timing analysis of binary X ray pulsars observed by HEAO 1. In J. Hunt and B. Battrick, editors, *Two Topics in X-Ray Astronomy, Volume 1: X Ray Binaries. Volume 2: AGN and the X Ray Background*, volume 296 of *ESA Special Publication*, November 1989.

K. A. Southwell, D. O'Donoghue, and P. A. Charles. The optical light curve of the eclipsing LMXB EXO 0748-676. In H. U. Zimmermann, J. Trümper, and H. Yorke, editors, *Roentgenstrahlung from the Universe*, pages 191–192, February 1996.

A. W. Steiner, J. M. Lattimer, and E. F. Brown. The Neutron Star Mass-Radius Relation and the Equation of State of Dense Matter. ApJ, 765:L5, March 2013. doi: 10.1088/2041-8205/765/1/L5.

T. Strohmayer and L. Bildsten. *New views of thermonuclear bursts*, pages 113–156. April 2006.

L. Strüder, U. Briel, K. Dennerl, R. Hartmann, E. Kendziorra, N. Meidinger, E. Pfeffermann, C. Reppin, B. Aschenbach, W. Bornemann, H. Bräuninger, W. Burkert, M. Elender, M. Freyberg, F. Haberl, G. Hartner, F. Heuschmann, H. Hippmann, E. Kastelic, S. Kemmer, G. Kettenring, W. Kink, N. Krause, S. Müller, A. Oppitz, W. Pietsch, M. Popp, P. Predehl, A. Read, K. H. Stephan, D. Stötter, J. Trümper, P. Holl, J. Kemmer, H. Soltau, R. Stötter, U. Weber, U. Weichert, C. von Zanthier, D. Carathanassis, G. Lutz, R. H. Richter, P. Solc, H. Böttcher, M. Kuster,

R. Staubert, A. Abbey, A. Holland, M. Turner, M. Balasini, G. F. Bignami, N. La Palombara, G. Villa, W. Buttler, F. Gianini, R. Lainé, D. Lumb, and P. Dhez. The European Photon Imaging Camera on XMM-Newton: The pn-CCD camera. A&A, 365:L18–L26, January 2001. doi: 10.1051/0004-6361:20000066.

R. A. Sunyaev and L. G. Titarchuk. Comptonization of X-rays in plasma clouds - Typical radiation spectra. A&A, 86:121–138, June 1980.

T. M. Tauris and E. P. J. van den Heuvel. *Formation and evolution of compact stellar X-ray sources*, pages 623–665. April 2006.

B. Thomas, R. Corbet, T. Augusteijn, P. Callanan, and A. P. Smale. Optical and X-ray observations of the low-mass X-ray binary EXO 0748-676. ApJ, 408:651–655, May 1993. doi: 10.1086/172624.

A. Treves, R. Turolla, S. Zane, and M. Colpi. Isolated Neutron Stars: Accretors and Coolers. PASP, 112:297–314, March 2000. doi: 10.1086/316529.

A. Treves, S. B. Popov, M. Colpi, M. E. Prokhorov, and R. Turolla. The Magnificient Seven: Close-by Cooling Neutron Stars? In R. Giacconi, S. Serio, and L. Stella, editors, *X-ray Astronomy 2000*, volume 234 of *Astronomical Society of the Pacific Conference Series*, page 225, 2001.

M. J. L. Turner, A. Abbey, M. Arnaud, M. Balasini, M. Barbera, E. Belsole, P. J. Bennie, J. P. Bernard, G. F. Bignami, M. Boer, U. Briel, I. Butler, C. Cara, C. Chabaud, R. Cole, A. Collura, M. Conte, A. Cros, M. Denby, P. Dhez, G. Di Coco, J. Dowson, P. Ferrando, S. Ghizzardi, F. Gianotti, C. V. Goodall, L. Gretton, R. G. Griffiths, O. Hainaut, J. F. Hochedez, A. D. Holland, E. Jourdain, E. Kendziorra, A. Lagostina, R. Laine, N. La Palombara, M. Lortholary, D. Lumb, P. Marty, S. Molendi, C. Pigot, E. Poindron, K. A. Pounds, J. N. Reeves, C. Reppin, R. Rothenflug, P. Salvetat, J. L. Sauvageot, D. Schmitt, S. Sembay, A. D. T. Short, J. Spragg, J. Stephen, L. Strüder, A. Tiengo, M. Trifoglio, J. Trümper, S. Vercellone, L. Vigroux, G. Villa, M. J. Ward, S. Whitehead, and E. Zonca. The European Photon Imaging Camera on XMM-Newton: The MOS cameras : The MOS cameras. A&A, 365:L27–L35, January 2001. doi: 10.1051/0004-6361:20000087.

M. van der Klis. Quasi-periodic oscillations in low-mass X-ray binaries. In D. J. Helfand and J.-H. Huang, editors, *The Origin and Evolution of Neutron Stars*, volume 125 of *IAU Symposium*, pages 321–330, 1987.

M. van der Klis, L. Stella, N. White, F. Jansen, and A. N. Parmar. Intensity and source state dependence of the quasi-periodic oscillations in Scorpius X-1. ApJ, 316: 411–426, May 1987. doi: 10.1086/165210.

M. H. van Kerkwijk, D. Chakrabarty, J. E. Pringle, and R. A. M. J. Wijers. Warped Disks as a Possible Origin of Torque Reversals in Accretion-powered Pulsars. ApJ, 499:L27–L30, May 1998. doi: 10.1086/311346.

J. van Paradijs and J. E. McClintock. Absolute visual magnitudes of low-mass X-ray binaries. A&A, 290:133–136, October 1994.

J. van Paradijs and J. E. McClintock. Optical and ultraviolet observations of X-ray binaries. *X-ray Binaries*, pages 58–125, 1995.

J. van Paradijs and N. White. The Galactic Distribution of Low-Mass X-Ray Binaries. ApJ, 447:L33, July 1995. doi: 10.1086/309558.

J. van Paradijs, M. van der Klis, and H. Pedersen. Optical photometry of the X-ray source EXO 0748-676/UY Volantis. A&AS, 76:185–188, December 1988.

J. T. VanderPlas. Understanding the Lomb-Scargle Periodogram. *ArXiv e-prints*, March 2017.

R. A. Wade, H. Quintana, K. Horne, and T. R. Marsh. Optical studies of the X-ray transient EXO 0748-676. PASP, 97:1092–1095, November 1985. doi: 10.1086/131668.

B. Warner. Multiple optical orbital sidebands in intermediate polars. MNRAS, 219: 347–356, March 1986. doi: 10.1093/mnras/219.2.347.

M. C. Weisskopf, H. D. Tananbaum, L. P. Van Speybroeck, and S. L. O'Dell. Chandra X-ray Observatory (CXO): overview. In J. E. Truemper and B. Aschenbach, editors, *X-Ray Optics, Instruments, and Missions III*, volume 4012 of Proc. SPIE, pages 2–16, July 2000. doi: 10.1117/12.391545.

M. C. Weisskopf, B. Brinkman, C. Canizares, G. Garmire, S. Murray, and L. P. Van Speybroeck. An Overview of the Performance and Scientific Results from the Chandra X-Ray Observatory. PASP, 114:1–24, January 2002. doi: 10.1086/338108.

B. F. West, K. D. Wolfram, and P. A. Becker. Dynamical and Radiative Properties of X-Ray Pulsar Accretion Columns: Phase-averaged Spectra. ApJ, 835:130, February 2017. doi: 10.3847/1538-4357/835/2/130.

N. E. White and S. S. Holt. Accretion disk coronae. ApJ, 257:318–337, June 1982. doi: 10.1086/159991.

N. E. White and K. O. Mason. The structure of low-mass X-ray binaries. Space Sci. Rev., 40:167–194, February 1985. doi: 10.1007/BF00212883.

N. E. White and J. H. Swank. The discovery of 50 minute periodic absorption events from 4U 1915-05. ApJ, 253:L61–L66, February 1982a. doi: 10.1086/183737.

N. E. White and J. H. Swank. The discovery of 50 minute periodic absorption events from 4U 1915-05. ApJ, 253:L61–L66, February 1982b. doi: 10.1086/183737.

J. Wilms, A. Allen, and R. McCray. On the Absorption of X-Rays in the Interstellar Medium. ApJ, 542:914–924, October 2000. doi: 10.1086/317016.

M. T. Wolff, P. S. Ray, K. S. Wood, and P. L. Hertz. Eclipse Timings of the Transient Low-Mass X-ray Binary EXO 0748-676. IV. The Rossi X-ray Timing Explorer Eclipses. ApJS, 183:156–170, July 2009. doi: 10.1088/0067-0049/183/1/156.

I. Yi, J. C. Wheeler, and E. T. Vishniac. Torque Reversal in Accretion-powered X-Ray Pulsars: Erratum. ApJ, 491:L93–L93, December 1997. doi: 10.1086/311072.

G. Younes, L. Boirin, and B. Sabra. An XMM-Newton view of the dipping low-mass X-ray binary XTE J1710-281. A&A, 502:905–912, August 2009. doi: 10.1051/0004-6361/200811314.

Y. B. Zel'dovich. The Fate of a Star and the Evolution of Gravitational Energy Upon Accretion. *Soviet Physics Doklady*, 9:195, September 1964.

Z. Zhang and X.-D. Li. A diagnosis of torque reversals in 4U 1626-67. A&A, 518:A19, July 2010. doi: 10.1051/0004-6361/201013991.

Z. Zhang, K. Makishima, S. Sakurai, M. Sasano, and K. Ono. Probing the accretion scheme of the dipping X-ray binary 4U 1915-05 with Suzaku. PASJ, 66:120, December 2014. doi: 10.1093/pasj/psu117.

Z. Zhang, S. Sakurai, K. Makishima, K. Nakazawa, K. Ono, S. Yamada, and H. Xu. Suzaku Observation of the High-inclination Binary EXO 0748-676 in the Hard State. ApJ, 823:131, June 2016. doi: 10.3847/0004-637X/823/2/131.

C. Zurita, J. Casares, and T. Shahbaz. Evidence for Optical Flares in Quiescent Soft X-Ray Transients. ApJ, 582:369–381, January 2003. doi: 10.1086/344534.